ABSTRACT

THEORETICAL AND EXPERIMENTAL STUDIES OF THE FIELD – INDUCED PHENOMENA IN FLOWING SUSPENSIONS

by

Nikolai Markarian

The present work describes results of experimental and theoretical studies of the behavior of dilute suspensions subject to high gradient AC electric fields. When a spatially non-uniform electric field is applied to a suspension, in which the particles and the suspending fluid have different dielectric permittivities and/or conductivities, the particles migrate towards the regions of high or low electric field strengths depending on the sign of their polarization. This phenomenon, referred to as *dielectrophoresis*, has found numerous applications for the control and manipulation of the particle motions.

Presented in Chapter 3 are the results of studying the field –induced motion and segregation of particles in macro-scale. Experiments were conducted in a parallel-plate channel in which an extremely dilute suspension of heavy, positively polarized spheres was exposed to an ac electric field under conditions such that the field lines were arranged along the channel cross section perpendicular to the streamlines of the main flow. Following the application of a high-gradient strong ac field (~ several kV/mm), the particles were found to move towards both the high-voltage and grounded electrodes and aggregate along their edges. The model calculations required no fitting parameters because the particle polarizability was determined independently by measuring the frequency and concentration dependence

of the complex dielectric permittivity of a suspension in a low-strength field (~ V/mm).

Chapter 4 is devoted to the studies of the field-induced particle motions and their segregation in suspensions flowing through microfluidic devices. Experiments were conducted on microfluidics with electrodes of different sizes arranged parallel and perpendicular to the flow. The conditions under which the interparticle electric interactions do not affect the particle trapping in high-field strength regions were identified.

In order to evaluate the effects of gravity on the particle motions and their segregation, the experiments have been conducted in microgravity environment aboard the NASA research aircraft. Appendix A presents the Test Equipment Data Package for the microgravity experiments, the results of which are currently in the process of being evaluated and would require further investigation.

THEORETICAL AND EXPERIMENTAL STUDIES OF THE FIELD – INDUCED PHENOMENA IN FLOWING SUSPENSIONS

by

Nikolai Markarian

A Dissertation
Submitted to the Faculty of the
New Jersey Institute of Technology
in Partial Fulfillment of the Requirements for the Degree of
Doctor of Philosophy in Mechanical Engineering

Department of Mechanical Engineering

May 2003

APROVAL PAGE

THEORETICAL AND EXPERIMENTAL STUDIES OF THE FIELD – INDUCED PHENOMENA IN FLOWING SUSPENSIONS

Nikolai Markarian

Dr. Boris Khusid, Dissertation Advisor — Date
Associate Professor of Mechanical Engineering, NJIT

Dr. Andreas Acrivos, Committee Member — Date
Professor Emeritus of Chemical Engineering, CCNY

Dr. Avraham Harnoy, Committee Member — Date
Professor of Mechanical Engineering, NJIT

Dr. Ernest S. Geskin, Committee Member — Date
Professor of Mechanical Engineering, NJIT

Dr. Rajesh N. Dave, Committee Member — Date
Professor of Mechanical Engineering, NJIT

Dr. Robert Pfeffer, Committee Member — Date
Professor of Chemical Engineering, NJIT

Dr. Kenneth R. Farmer II, Committee Member — Date
Associate Professor of Physics, NJIT

BIOGRAPHICAL SKETCH

Author: Nikolai Markarian

Degree: Doctor of Philosophy

Undergraduate and Graduate Education:

- Doctor of Philosophy in Mechanical Engineering,
  New Jersey Institute of Technology, Newark, NJ, 2003

- BS/MS in Manufacturing Engineering,
  Bauman Moscow State Technical University, Moscow, Russia, 1998

Major: Mechanical Engineering

Presentations and Publications

Markarian, N., Yeksel M., Khusid B., Farmer K., Acrivos A., Limitations on the scale of an electrode array for trapping particles in microfluidics by positive dielectrophoresis , Applied Physics Letters, (Accepted for publication on April 17, 2003)

Markarian, N., Yeksel M., Khusid B., Farmer K., Acrivos A., Trapping particles in microfluidics by positive dielectrophoresis, Twenty-ninth Annual Northeast Bioengineering Conference, Newark, NJ, March 22 and 23, 2003.

Qiu, Z., Acrivos A., Markarian N., Khusid B., Electric-field-induced dielectrophoresis and heterogeneous aggregation in dilute suspensions of positively polarizable particles, American Physical Society, 55th Annual Meeting of the Division of Fluid Dynamics, Dallas, TX, November 24-26, 2002.

Acrivos, A., Markarian N., Qiu Z., Khusid B., Farmer K., A Multi-channel Dielectrophoretic Micro-device for Pressure Driven Suspension Flow, The AIChE 2002 Annual Meeting, Indianapolis, Indiana , November 3 - 8, 2002.

Qiu, Z., Markarian N., Khusid B. and Acrivos A., Positive dielectrophoresis and heterogeneous aggregation in high-gradient ac electric fields, J. Appl. Phys., 92, 2829, 2002.

Acrivos, A., Qiu Z., Khusid B., Markarian N., Particle segregation in a flowing suspension subject to high-gradient strong electric fields, Sixth Microgravity Fluid Physics and Transport Phenomena Conference, Abstracts, Cleveland, OH, August 14-16, 2002 p. 35-36.

Markarian N., Qiu Z., Studies of the particle motions in a suspension subject to high-gradient ac electric field. Fourteenth U.S. National Congress of Theoretical and Applied Mechanics, Blacksburg, VA, June 23-28, 2002.

Acrivos A., Qiu Z., Khusid B., Markarian N., Positive dielectrophoresis and aggregation In suspensions of highly polarized particles subjected to high-gradient AC electric fields in macro-scale flow and micro-fluidics, *American Physical Society, 54th Annual Meeting of the Division of Fluid Dynamics,* San Diego, CA, November 18-20, 2001.

Acrivos A., Qiu Z., Khusid B. and Markarian N., Effects of high-gradient ac electric fields on the suspension flow in a rotating channel, The AIChE 2001 Annual Meeting, Reno, Nevada, November 4 - 9, 2001.

Fraser M., Magoun, Ip P., Force K., Horsburgh S., Acrivos A., Khusid B., Markarian N., Final Report - Virtual instrument development and test suite (VIDTS), September 4, 2001, Sponsored by DARPA (DoD), Issued by U.S. Army Aviation and Missile Command Under Contract No. DAAH01-01-C-R028.

This dissertation is dedicated to my loving parents who provided the inspiration and support.

ACKNOWLEDGEMENTS

I would like to express my sincere gratitude and appreciation towards my advisor Dr. Boris Khusid for his valuable guidance, friendship and continuing support. I am deeply indebted to Dr. Andreas Acrivos for his continuing guidance and support. I thank him for giving me the opportunity to work with and being the member of his research group at The Levich Institute of The City College of New York. Without his valuable support this dissertation would not have been completed. I also express my gratitude towards Dr. Kenneth Farmer for providing guidance and support and much valuable advice. Special thanks are due to Dr. Avraham Harnoy, Dr. Ernest Geskin, Dr. Rajesh Dave, and Dr. Robert Pfeffer for serving as members of my dissertation committee.

I appreciate the active support and input of my friends and colleagues Dr. Anubhav Tripathi, Dr. Mahesh Tirumkudulu, Dr. Zhiyong Qiu, Anil Kumar, Mike Yeskel, Bo Jin. I also appreciate the encouragement and help from my friends Konstantin Babets, Dmitriy Shishkin, and many other friends at NJIT.

And finally, grateful thanks and deep appreciation to my father Ashot, mother Tamara, sister Emma and friend Yelena for their support, encouragement and love through all these years. I could not have done it without you.

TABLE OF CONTENTS

TABLE OF CONTENTS
(Continued)

Chapter **Page**

LIST OF FIGURES

LIST OF FIGURES
(Continued)

Figure **Page**

LIST OF FIGURES
(Continued)

Figure **Page**

LIST OF FIGURES
(Continued)

Figure **Page**

LIST OF FIGURES
(Continued)

Figure **Page**

CHAPTER 1

INTRODUCTION

1.1 Dielectrophoresis and its Applications

Small particles from one micron (10^{-6} m) up to one millimeter (10^{-3} m) in size are becoming increasingly important in today's technological world. Though often hidden from view, they play a major role in many mechanisms and devices – from electrostatic copiers and printers to fluidized beds. A rapidly emerging area involves particles of biological origin – the characterization, handling, and manipulation of individual cells and DNA molecules.

Being exposed to an electric or a magnetic fields, a particle experiences a force and a torque which depend on its electrical and magnetic properties as well as on the particle shape and volume.

In this work, the effects of the dielectrophoretic force will be considered. *Dielectrophoresis* (hereafter referred to as DEP) refers to the force exerted on the induced dipole moment of an uncharged dielectric and/or conductive particle by a spatially nonuniform electric field

The first significant demonstration of biological dielectrophoresis involved the separation of living biological cells (Pohl, 1978). Pohl envisioned both clinical and laboratory applications of such a technology. Due to the rapid progress made over the past decade, biological DEP certainly merits special focus in any discussion of applications.

(1) Electrofusion

A dramatic success of dielectrophoresis is its use by Zimmermann and his colleagues in electric field-mediated cell fusion (Zimmermann and Vienken, 1982). In this procedure, a suspension containing two cell types that are to be fused is introduced into a chamber with an electrode array that creates a nonuniform electric field. The nonuniform field, which has a typical frequency in the range of 100 to 1000 kHz and a magnitude of approximately 100V/cm, collects a fraction of these cells on electrode surfaces where the cells of the two types inevitably encounter each other and form chains. When a sufficient number of chains of the desired type have formed, a series of short DC pulses, typically ~ 10 μsec at ~ 1kV/cm, is applied to the electrodes. The strong DC pulses puncture or disrupt the membranes in the region of contact between the cells which then initiate their merger or fusion into hybrids that, presumably, incorporate desirable attributes of each constituent. Potential applications for this technology are envisioned in the production of hybridomas for antibody production useful in cancer research and treatment.

(2) Cell manipulation

Washizu (Washizu,1990) has investigated applications of DEP for manipulating cells and other biological particles, and has primarily focused on the development of practical technologies for automated processing of cells and other biological particles, such as DNA. He has developed a microminiature assembly line for cell fusion called a *fluid-integrated circuit* (FIC), which incorporates photolithografically fabricated electrode and insulator contours with a miniaturized piezoelectric pump (Masuda et al., 1989; Washizu

et al., 1990). The capability to transport cells, one at a time, through complex processing protocols using these rather simple electrode configurations has been demonstrated. One example is the unique cell positioning system shown in Figure 1.1(a), which assembles cell chains prior to electrofusion. The insulating barrier constricts the electric current to flow through the aperture, thus intensifying the electric field so that two cells introduced on either side of the barrier are attracted to the aperture where they form a cell chain. The cell shift register of Figure 1.1(b) works on a similar principle; by applying an AC voltage sequentially to the electrodes, single cells are transported along the structure one at a time.

Washizu also reports success in collecting and positioning DNA molecules and other biological macromolecules with microfabricated electrodes (Washizu and Kurosava, 1990; Washizu et al., 1993b). In this process, the dielctrophoretic force is harnessed to collect and position the particles.

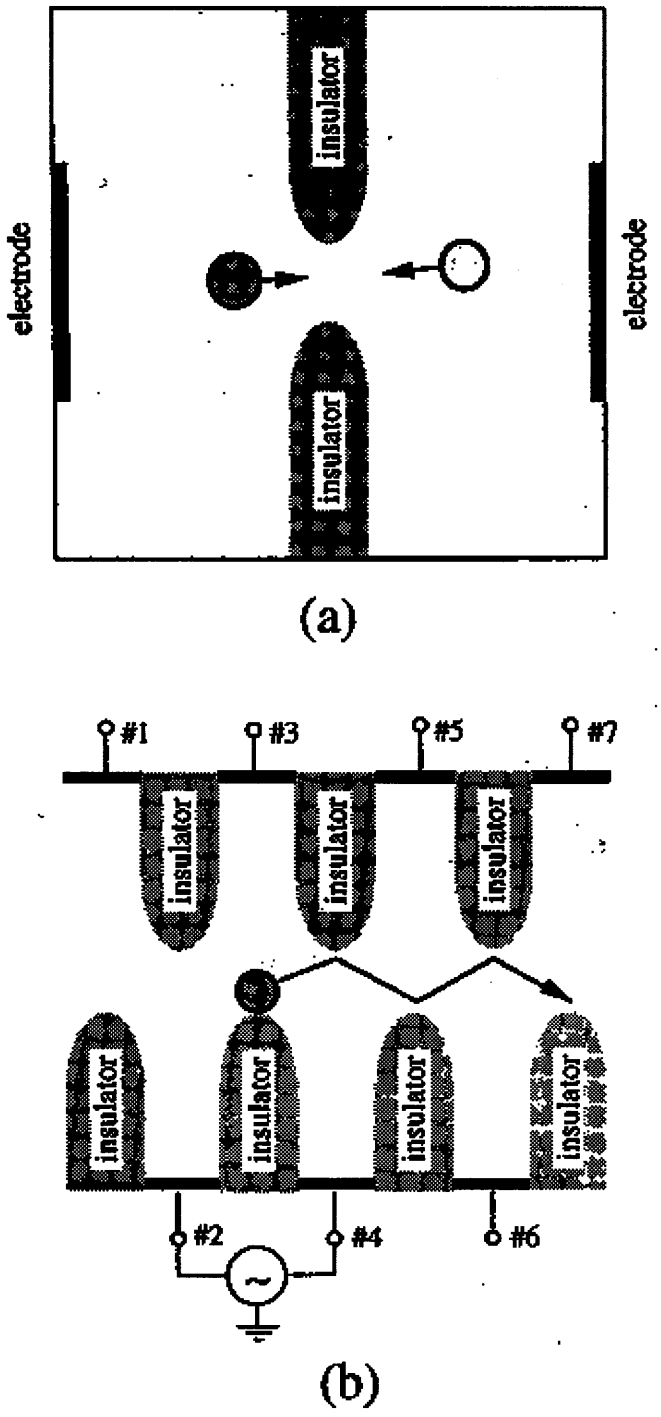

Figure 1.1 Fluid integrated circuit concepts of Washizu (1990) using dielectrophoretic effect for handling and manipulation of biological cells.
(a) Electrode/insulator structure for automated electrofusion system
(b) Dielectrophoretic cell shift register

(3) Basic cell studies

One method of investigating the cell structure is the use of DEP measurement to develop models of their dielectric properties. The task is usually posed as an inverse problem to the investigator, where the cell structure must be inferred from measured DEP spectra.

Marszalek (Marszalek et al., 1989) used a simple device which contained a vertically aligned set of closely spaced electrode wires with variable-frequency AC voltage applied between them to obtain cell spectra. By releasing cells one at a time and then monitoring them with a microscope as they sank, he observed their response to the two-dimensional nonuniform electric field. The technique involved recording the (inertialess) motion in the horizontal plane for various applied voltages at different frequencies. Both negative and positive DEP spectra of Neurospora crassa (slime) were obtained in this way.

A technique more suited for measuring the DEP spectra of cell populations uses interdigitated electrodes mounted in an optical sample chamber to monitor the frequency-dependent collection of cells (Price et al., 1988; Burt et al., 1989). An advantage of this system is that it is readily automated. An optical detector measures the DEP cell collection by monitoring light transmission through a chamber. To distinguish negative from positive DEP, fairly sophisticated image analysis methods are required (Gascoyne et al., 1992). The technique has been used over the frequency range from 1 Hz to 2 MHz to investigate the effects of certain chemical agents on the surface charge and membrane conductivity in mammalian cells.

The unique capability of the DEP levitation (one of the DEP theory applications (Jones, 1995)) is its capability of measuring properties of a single cells and chains.

Figure 1.2 illustrates the essential features of a simple computer-controlled DEP levitation system. The particle is illuminated from the side and its shadow is focused on a photodiode array or a video camera. Axial displacements of the particle are translated to a digital signal that is converted to analog, amplified, and used to modulate the amplitude of the AC levitation voltage. The technique has been used to measure the membrane capacitance c_m of single-plant protoplasts and (mammalian) ligament cells (Kaler and Jones, 1990). This is accomplished by obtaining the DEP spectra of individual cells and then comparing them to the predicted spectra of a simple spherical shell model.

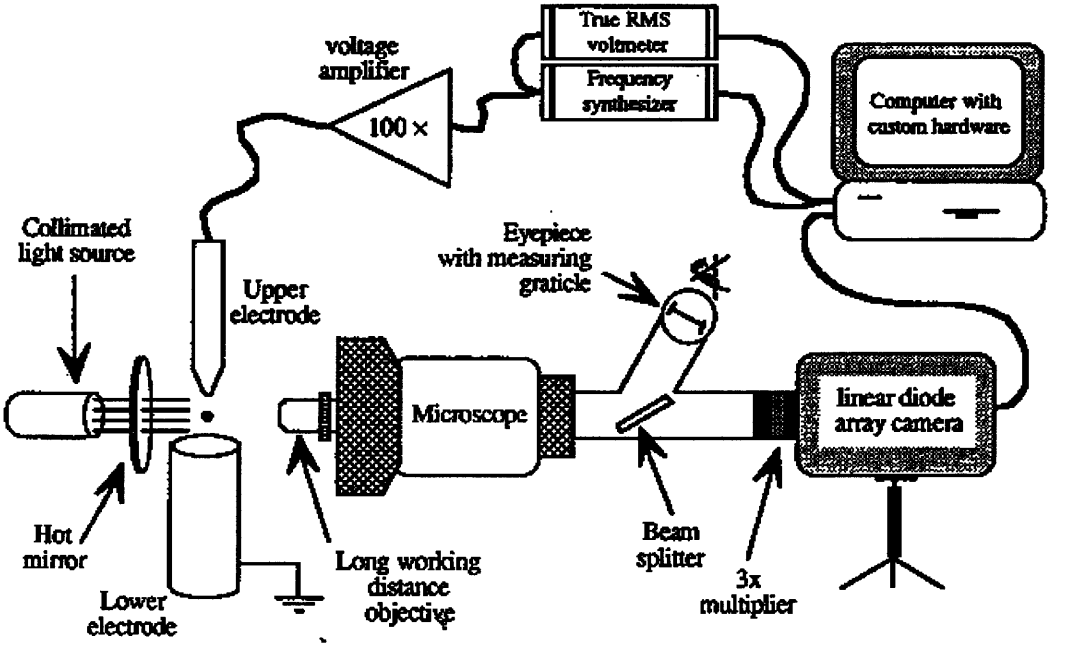

Figure 1.2 Feedback control levitation system for automated acquisition of DEP spectral data. (from T. N. Tombs and T. B. Jones, "Effects of moisture on the dielectrophoretic spectra of glass spheres", IEEE Transaction on Industry Applications, vol.29, pp.281-285, © 1993 IEEE.)

1.2 Theoretical Background

A variety of energy dissipation mechanisms, including conduction and dielectric relaxation phenomena, can influence the behavior of a suspension subject to an electric field. When the dissipation of electric energy is present (the so-called *not-perfect dielectric*), the time-variation of the dipole moment acquired by a suspension subject to a field does not follow the time variation of the applied field. For example, the polarization of such a suspension exhibits a time delay when an electric field is suddenly applied and a phase lag when an electric field is a sinusoidal function of time. The nature of these phenomena will be explained briefly in this chapter. In contrast, the so-called model of a *perfect dielectric*, i.e., without energy loss, is applied to a system whose polarization instantaneously follows the time variation of the applied field.

Throughout this work, the suspensions whose polarization cannot be described by the model of a perfect dielectric will be considered. This means, for example, that the dielectric permittivity of such a suspension exposed to an AC electric field is a complex number that includes both real and imaginary parts. The latter characterizes the loss of electric energy during a cycle of the field oscillation. In contrast, the dielectric permittivity of a perfect dielctric is a real number.

1.2.1 Dielectric Response of Materials

The macroscopic response of an isotropic dielectric exposed to a time varying, relatively weak electric field, E(t), can be described (in SI units) by the following equation (Russel et al., 1989):

$$D(t) = \varepsilon_0 E(t) + \varepsilon_0 \int_0^{\infty} f(\tau) E(t-\tau) d\tau , \qquad (1.1)$$

where D(t) is the electric displacement, ε_0 is the dielectric constant of vacuum, and the scalar relaxation function $f(\tau)$ characterizes the history–dependence of the material polarization. This function accounts for some inertia of the displacement of charges when the material is subjected to a field. The linearity of Equation (1.1) with respect to the electric field strength enables the decomposition of the polarization of a material subjected to an AC electric field, $E(t) = E(\omega)\exp(i\omega t)$, into Fourier components such that

$$D(\omega) = \varepsilon^*(\omega)E(\omega) \tag{1.2}$$

where ω is a frequency of the applied field and ε_0 is included, for brevity, as a factor into $\varepsilon^*(\omega)$. $D(\omega)$ is, in general, out of phase with $E(\omega)$. The complex number $\varepsilon(\omega)$ which relates them is called the complex dielectric permittivity. Splitting $\varepsilon(\omega)$ into its real and imaginary parts yields

$$\varepsilon^*(\omega) = \varepsilon'(\omega) - i\varepsilon''(\omega) \tag{1.3}$$

where $\varepsilon'(\omega)$ determines the polarization of the dielectric whereas $\varepsilon''(\omega)$ specifies the energy loss. For example, a widely used Debye's model for the polarization of a non-perfect dielectric (Daniel, 1967) leads to the following expressions for $\varepsilon'(\omega)$ and $\varepsilon''(\omega)$:

$$\varepsilon'(\omega) = \varepsilon_\infty + \frac{\varepsilon_s - \varepsilon_\infty}{1+\omega^2\tau^2} \tag{1.4}$$

$$\varepsilon''(\omega) = (\varepsilon_s - \varepsilon_\infty)\frac{\omega\tau}{1+\omega^2\tau^2}$$

where ε_s and ε_∞ refer to the static and optical dielectric constants, respectively. These functions are illustrated in Figure 1.3.

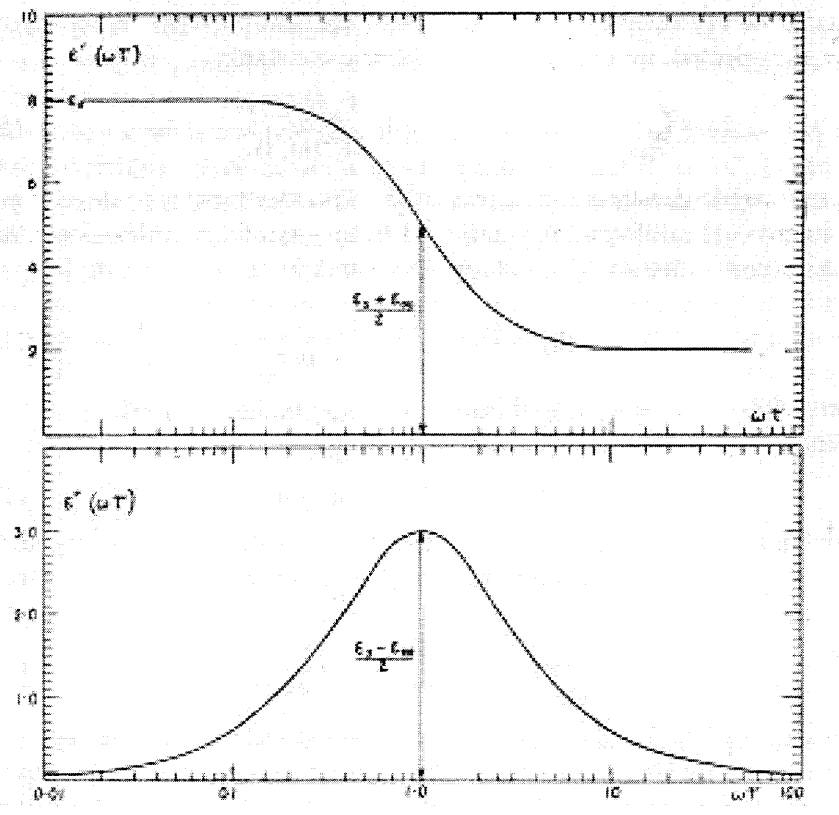

Figure 1.3 Dielectrics with a single relaxation time (Daniel, 1967).
(a) The real part of $\varepsilon^*/\varepsilon_0$ as a function of $\log(\omega\tau)$ according to the Debye equations
(b) The imaginary part of $\varepsilon^*/\varepsilon_0$ for the same dielectric

For the model of a perfect dielectric with $f(\tau) = \chi \cdot \delta(\tau)$ where $\delta(t)$ is a delta-function, Equation (1.1) yields

$$D(t) = \varepsilon_0 E(t) + \varepsilon_0 \chi E(t) = \varepsilon_0 (1+\chi) E(t) \tag{1.5}$$

where χ is the electric susceptibility of the dielectric (Feynman et al., 1965). Equation (1.5) is usually written as

$$D(t) = \varepsilon E(t) \tag{1.6}$$

where $\varepsilon = \varepsilon_0 (1+\chi)$ is the dielectric constant of the material. For an AC field:

$$D(\omega) = \varepsilon E(\omega) \tag{1.7}$$

This expression shows that the dielectric displacement of a perfect dielectric does not depend on the frequency of the applied field. Moreover, the dielectric constant ε does not contain imaginary part, so that there is no phase shift between the electric displacement and the applied filed. Plots for the dielectric constants for both cases are depicted in Figure 1.4. Model of a perfect dielectric is more applicable for insulating liquids such as transformer oils when the real part of the dielectric constant does not vary in a wide range of frequencies and its imaginary part can be neglected.

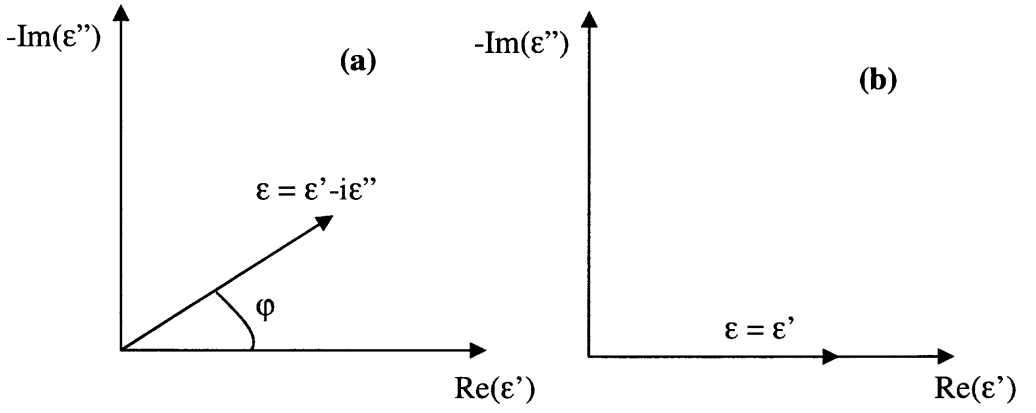

Figure 1.4 Dielectric permittivity of a non-perfect dielectric.
(a) Non-perfect dielectric, where φ is the phase shift between the electric displacement $D(t)$ and the applied electric field $E(t)$
(c) Perfect dielectric, no phase shift

As was mentioned earlier, in this work the model of a not perfect dielectric will be used mostly. For example, Figures 1.5 and 1.6 show the real part and imaginary parts of the complex dielectric permittivities of corn oil and a suspension of 5% aluminum oxide particles in corn oil. The measurements were conducted in the frequency range from 1Hz to 3MHz at 20^0C on the BDS 80 Dielectric Spectrometer, Novocontrol. As can be seen from these graphs, these systems cannot be described by a model of a perfect dielectric. Generally, the model of a perfect dielectric is of very limited use for colloidal suspensions (Dukhin et al., 1974).

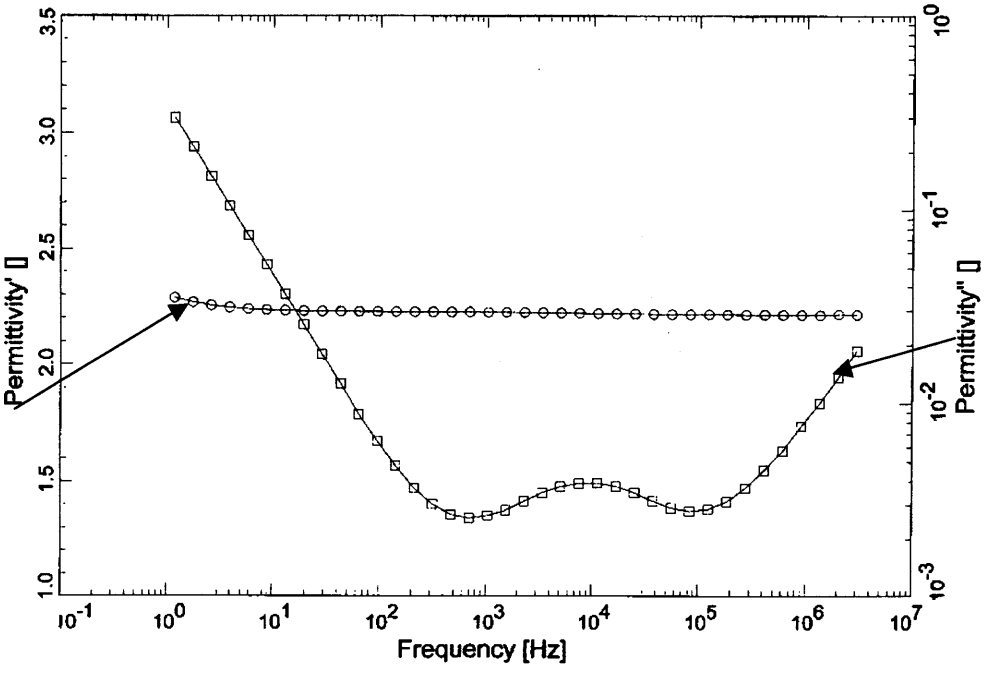

Figure 1.5 Real (permittivity') and imaginary (permittivity") parts of the dielctric constant for pure corn oil.

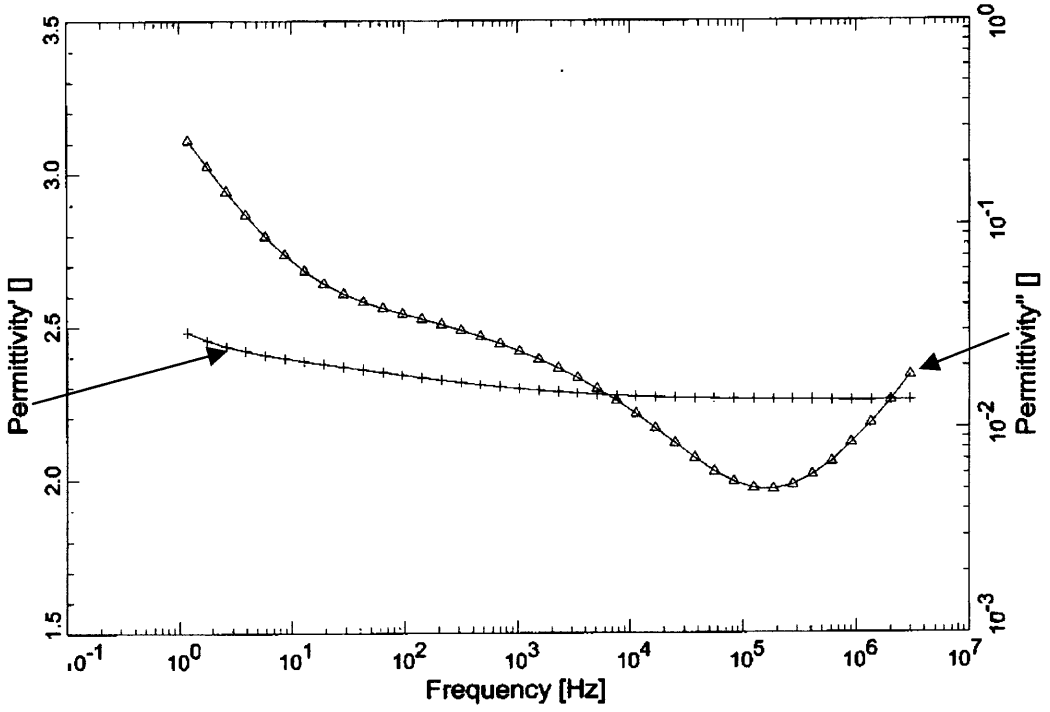

Figure 1.6 Real (permittivity') and imaginary (permittivity") parts of the dielctric constant for 5% concentrated suspension of aluminum oxide particles in the corn oil.

1.2.2 Theory of the Ponderomotive Force

The first step in the theory of the electrohydrodynamics of suspensions is to evaluate a net force acting on a particle. This reveals the so-called ponderomotive force exerted on dielectric particle by a spatially nonuniform electrostatic field. The dipole consists of equal and opposite charges, +q and –q located a vector distance $\bar{d}$ apart, subject to an electric field $\bar{E}$ (Figure 1.7).

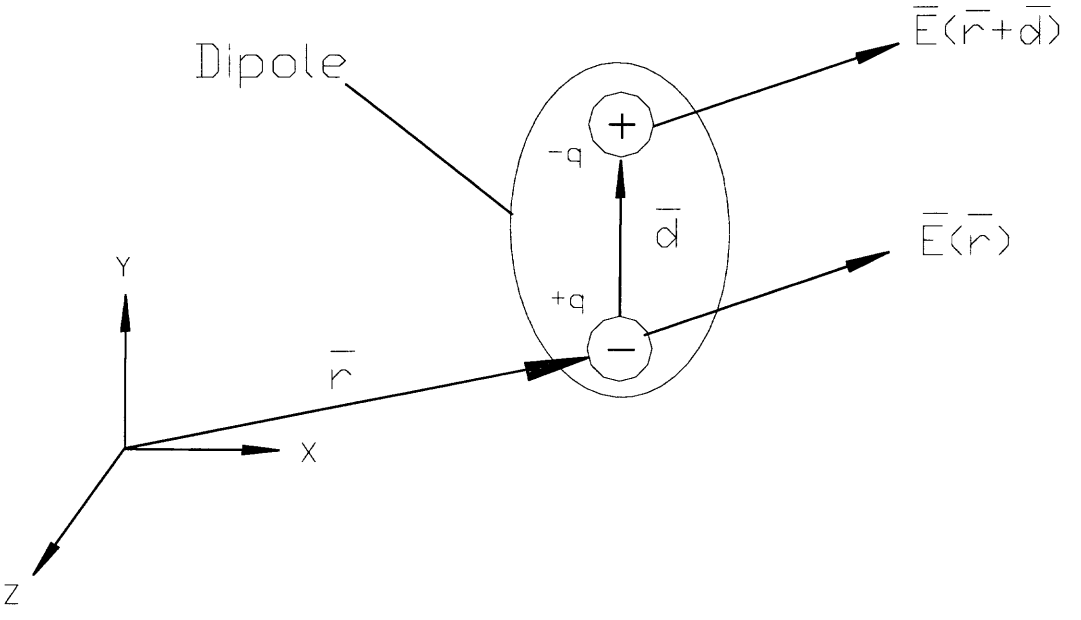

Figure 1.7 Net force on a small dipole of strength p=qd in a nonuniform electric field.

If the applied field is spatially nonuniform, then these two charges (+q and –q) will experience different values of the vector field $\overline{E}$ and, thus, the dipole will experience a net force. Summing the forces acting on these charges gives (Jones, 1995)

$$\overline{F} = q\overline{E}(\overline{r} + \overline{d}) - q\overline{E}(\overline{r}) \tag{1.8}$$

where $\overline{r}$ is the position vector of –q. Equation (1) can be simplified when $|\overline{d}|$ is small compared to the characteristic dimension of the electric field nonuniformity. In this case, the electric field can be expanded about position $\overline{r}$ using a vector Taylor series expansion; that is

$$\overline{E}(\overline{r} + \overline{d}) = \overline{E}(\overline{r}) + \overline{d} \cdot \nabla\overline{E}(\overline{r}) + \cdots \tag{1.9}$$

where all additional terms, of order higher than d, have been neglected. Substituting Equation (1.9) in Equation (1.8), the following result is obtained

$$\overline{F} = q\overline{d} \cdot \nabla\overline{E} + \cdots \tag{1.10}$$

If the limit $|\overline{d}| \longrightarrow 0$ is taken in such a way that $\overline{p} \equiv q\overline{d}$ (the dipole moment) remains finite, then the following expression for the force acting on an infinitesimal dipole results:

$$\overline{F}_{dipole} = \overline{p} \cdot \nabla\overline{E} \tag{1.11}$$

Equation (1.11) shows that no net force is exerted on a dipole unless the externally imposed electric field is spatially nonuniform.

For a special case of a homogeneous, dielectric sphere immersed in a dielectric fluid, the expression for the effective dipole moment is (Jones, 1995)

$$p_{eff} = 4\pi\varepsilon_f \beta a^3 E_0 \tag{1.12}$$

where a is the radius of the particle, E_0 is the magnitude of the applied field, β, known as the Clausius-Mossotti function, characterizes the effective polarization of a spherical

particle as a function of ε_f (the permittivity of the suspending fluid) and ε_p (the permittivity of the particle)

$$\beta(\varepsilon_p, \varepsilon_f) = \frac{\varepsilon_p - \varepsilon_f}{\varepsilon_p + 2\varepsilon_f} \tag{1.13}$$

With the use of Equation (1.12) and (1.13), Equation (1.10) yields the following expression for the dielectrophoretic (DEP) force acting on a perfect dielectric particle (Pohl,1951)

$$\overline{F}_{DEP} = 2\pi\varepsilon_f a^3 \left(\frac{\varepsilon_p - \varepsilon_f}{\varepsilon_p + 2\varepsilon_f} \right) \nabla E_0^2 \tag{1.14}$$

The examination of the Equation (1.13) demonstrates the important features of the dielectrophoretic effect experienced by a particle. They are the following:

1. F_{DEP} is proportional to the particle volume
2. F_{DEP} is also proportional to ε_f , the dielectric permittivity of the fluid in which the particle is suspended
3. The DEP force vector is directed along the gradient of the electric field intensity ∇E_0^2 , which, in general, is not parallel to the electric field vector $\overline{E_0}(\bar{r})$
4. The DEP force depends on the magnitude and the sign of the Clausius-Mossotti function β

Depending on the sign of β, two dielectrophoretic effects are distinguished:

Positive dielectrophoresis: $\beta > 0$ (or $\varepsilon_p > \varepsilon_f$). Particles are attracted into the region of *high electric fields* and repelled out of the region of *low electric fields*.

Negative dielectrophoresis: $\beta < 0$ (or $\varepsilon_p < \varepsilon_f$). Particles are attracted into the region *of low electric fields* and repelled out of the region of *high electric fields*.

Figures 1.8(a) and (b) illustrate the positive and negative dielectrophoretic phenomena for two different arrangements of electrodes. In the concentric cylindrical geometry of Figure 1.8 (a), the observed force is parallel to the electric field vector, that is, $\overline{F}_{DEP} \| \overline{E}_0$. On the other hand, between the nonparallel electrode plates shown in Figure 1.8 (b), the DEP force and the electric field vector are orthogonal, that is, $\overline{F}_{DEP} \perp \overline{E}_0$. In the general case, the force vector $\overline{F}_{DEP}$ can have any orientation with respect to the electric field vector

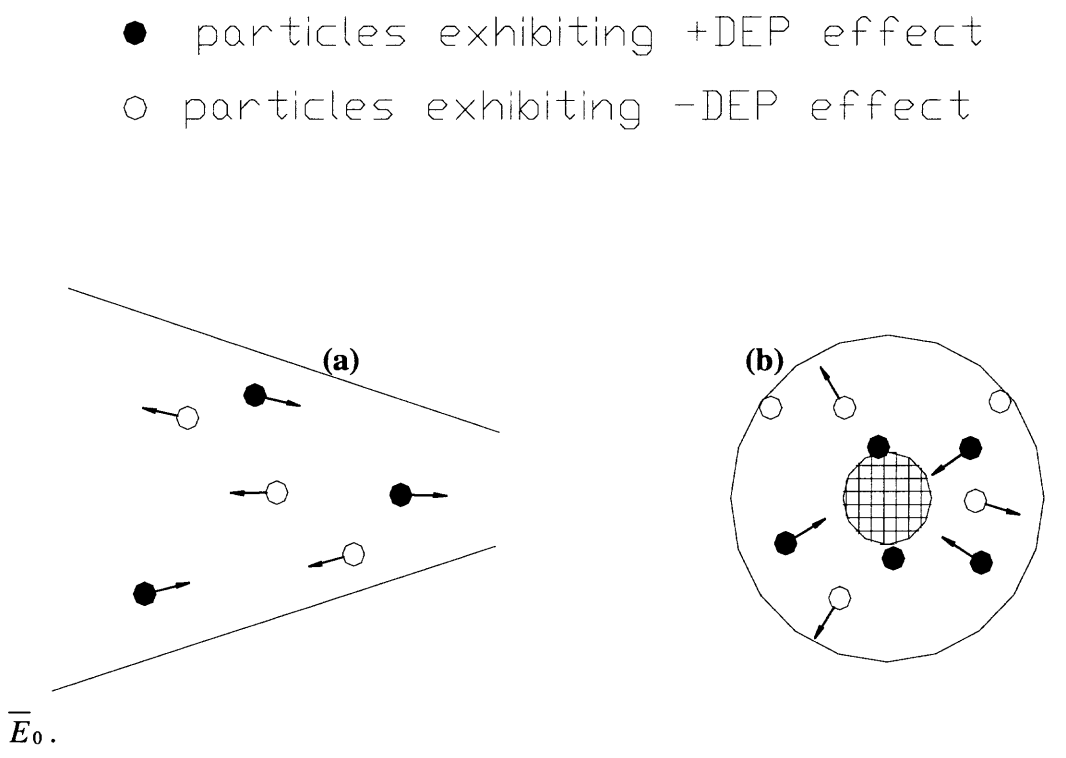

Figure 1.8 Positive and negative dielectrophoretic effects in different electrode structures.

(a) Electric field vector perpendicular to its gradient: $\overline{F}_{DEP} \perp \overline{E}_0$

(b) Electric field parallel to is gradient: $\overline{F}_{DEP} \| \overline{E}_0$

Now consider a suspension where spherical particles and a fluid medium have, in addition, finite conductivities, σ_p and σ_f, respectively. When such a suspension is subjected to an AC electric field of magnitude E_0 at radian frequency ω, the equation for the complex effective moment will be (Jones, 1995):

$$p_{eff}^* = 4\pi\varepsilon_f \beta^* a^3 E_0 \tag{1.15}$$

where the Clausius-Mossotti factor becomes a function of the complex permittivities containing magnitude and phase information about the effective dipole moment

$$\beta^*(\varepsilon_p^*, \varepsilon_f^*) = \frac{\varepsilon_p^* - \varepsilon_f^*}{\varepsilon_p^* + 2\varepsilon_f^*} \tag{1.16}$$

with the complex permittivities for the particle and the suspending medium given by the following expressions

$$\varepsilon_p^* = \varepsilon'_p - i\varepsilon''_p + \sigma_p / i\omega \tag{1.17}$$

$$\varepsilon_f^* = \varepsilon'_f - i\varepsilon''_f + \sigma_f / i\omega \tag{1.18}$$

Here ε''_f and ε''_p are the frequency dependent dielectric loss terms.

The time-average dielectrophoretic force in this case will be (Jones, 1995)

$$\left\langle \overline{F}_{DEP} \right\rangle = 2\pi\varepsilon_f a^3 \,\mathrm{Re}[\beta^*(\omega)]\nabla E_{rms}^2 \tag{1.19}$$

where E_{rms} is the root-mean-square magnitude of the imposed AC electric field. The real part of the Clausius–Mossotti function $\mathrm{Re}[\beta^*(\omega)]$ determines the frequency dependence of the time-average dielectrophoretic force.

In order to compute the dielectrophoretic force, the real part of the relative polarization, $\mathrm{Re}[\beta^*]$, needs to be determined, which requires measurement of the

dielectric permitivity of the particle, ε^*_p, which is hard to measure experimentally as it is very much sensitive to the medium in which measurements are being performed. An alternative way is to measure experimentally the complex permitivity of suspension of randomly distributed spherical particles along with the complex permitivity of the pure fluid and then applying Maxwell-Wagner expression (Equation(1.19)) the real part of the relative polarization $\mathrm{Re}\lfloor\beta^*\rfloor$ can be determined. The widely used Maxwell-Wagner expression for the complex permittivity ε^*_s of a suspension of randomly distributed spherical particles yields (Dukhin et al., 1974)

$$\frac{\varepsilon_s^* - \varepsilon_f^*}{\varepsilon_s^* + 2\varepsilon_f^*} = \varphi\beta^* \tag{1.20}$$

where φ is the volume concentration of the particles, ε^*_f and ε^*_p are the complex dielectric permittivities of the suspending fluid and the particle, respectively, and β^* is the relative particle polarization.

1.3 Unresolved Problems

The focus of the experimental and theoretical research on dielectrophoretic phenomena has varied through the years, depending on the field of application that was targeted. The theoretical studies focused on deriving expressions for the dielectric force acting on a single dielectric particle (not perfectly insulating or perfectly conducting, layered, non-spherical, etc.) immersed in a dielectric (not perfectly insulating or perfectly conducting) medium. On the other hand, much of the early experimental work on dielectrophoresis in suspensions dealt with the design and fabrication of dielectrophoretic filters for removing particulates from fluids (Pohl, 1978, Lin et al., 1983). Because of the complexity of such filters due to their complicated geometry and associated flow patterns, these investigations were concerned mainly with the collection efficiency of these devices, as

gauged by the difference between the inlet and outlet suspension concentrations, as a function of the applied voltage, the field frequency, the flow rate, and the type of particles.

Recent investigations of dielectrophoretic phenomena in suspensions have focused on the development of micro-devices for the separation of biospecies (Zimmermann, 1996, Pethig et al., 1992). Most studies of biological suspensions used a flat, transparent horizontal micro-channel that was equipped with an array of miniature electrodes on the bottom, and in which the particle motions were observed from the top by microscopy. But because of the small size of their devices and the complexity of the electric field configurations and flow patterns involved, as well as the poor characterization of the dielectric properties of such suspensions, none of the authors of the studies referred to above attempted to investigate quantitatively the particle motions in their flowing suspensions.

The currently favored approach to the qualitative interpretation of the ac-field driven manipulation of suspensions is based on a model (Chang et al., 1996, Pohl et al., 1984, Pohl, 1978, Zimmermann, 1996 , Koch et al., 2000, Jones, 1995) which considers only the force exerted on a single particle by an external field and neglects the field-induced and hydrodynamic interparticle interactions both being inversely proportional to the interparticle distance raised to the power three. On the other hand, the purpose of the field-induced separation is to concentrate particles in certain regions of a device. This clearly raises the fundamental question regarding the extent to which these slow decaying electrical and hydrodynamic collective interactions can be neglected, and the predictions of a single-particle model can be used. Another important issue that still remains open is

how to characterize the polarization of a particle exposed to a strong electric field. The main purpose of the present work is to address experimentally and theoretically both these questions.

1.4 Field-Induced Heterogeneous Aggregation of Particles

Khusid and Acrivos (Khusid and Acrivos, 1996) developed a thermodynamic theory for the equilibrium characteristics of dielectrophoresis accompanied by phase transitions. Now, the kinetics of this phenomenon is considered. Specifically, suspensions so dilute that the field-induced aggregation proceeds significantly slower than the dielectrophoretic redistribution of the suspended particles are focused on. Under these conditions, the dielectrophoretic force concentrates particles in certain areas of an electric chamber where they then undergo a field-driven phase transition. This process to be referred to as *particle heterogeneous aggregation* is advantageous in numerous applications for controlling and manipulating suspension flow where one desires to remove the particles from the suspending liquid, or to separate particles having different polarization or size.

The effects of the *interparticle interactions* on the behavior of a low conducting suspension subjected to a strong electric field were considered in (Khusid and Acrivos, 1995, Khusid and Acrivos, 1999) where a theory was developed for the thermodynamics of the electric-field-driven phase separation of a quiescent suspension in low- and high concentrated phases. This theory is based on the model of the Maxwell-Wagner interfacial polarization of colloids (Dukhin et al., 1974, Russel et al., 1989) and the Lorentz model to describe long-range interactions of polarized particles (Landau et al., 1984). It provides a consistent interpretation of numerous available data on the field-

induced structure formation in suspensions. One of the main predictions of this theory is that there exists a similarity between the phase diagrams "the particle concentration vs. the field strength" of conducting colloids subject to electric fields and "the concentration vs. temperature" phase diagrams for the first-order phase separation in quenched conventional binary systems with a high-temperature miscibility gap. This important result will make it possible to exploit the great body of experimental data and theoretical models available for the quenching of atomic systems and use it as a framework for interpreting the morphology and kinetics of aggregation patterns in suspensions generated by the application of electric fields. This theory yielded a complete set of phase diagrams of suspensions subject to electric fields expressed in terms of λ and φ where $\lambda = \varepsilon_0 \varepsilon_f E^2 v_p / k_B T$ is the ratio between the electric energy of the interparticle interactions and the thermal energy, $k_B T$, and φ is the volume fraction of the particles. As an example, the simplest suspension phase diagram is sketched in Figure 1.9, where M and U denote the metastable and unstable domains, respectively. The *one-phase* region of the phase diagram includes the random spatial arrangement of the particles, whereas the *two-phase* region corresponds to the appearance of a field-induced phase separation. The coexistence curve outlines a two-phase region in the phase diagram. The distinction between the metastable and unstable domains corresponds to two mechanisms for the field-induced structure formation in a suspension: spinodal decomposition and nucleation, as occurs in binary atomic systems.

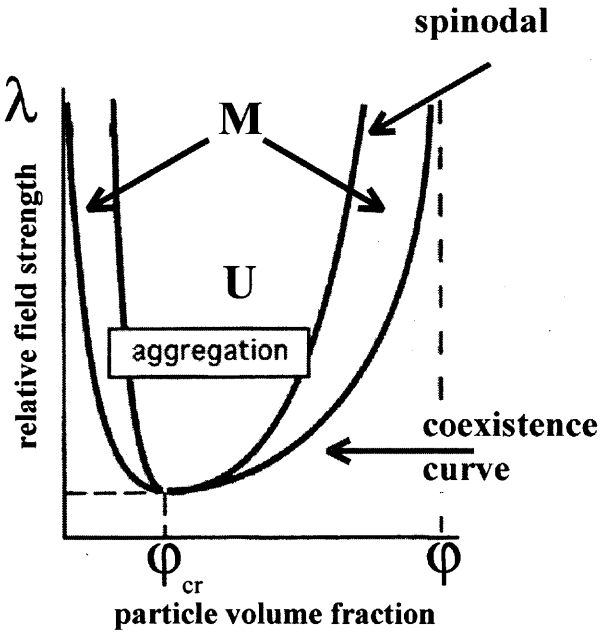

Figure 1.9 Phase diagram "the particle concentration vs. the field strength" of suspensions subject to electric fields. The metastable and unstable domains are denoted by M and U, respectively; λ is the relative strength of the field; φ is the particle volume concentration (Khusid and Acrivos, 1999).

In (Khusid and Acrivos, 1996) thermodynamic theory for the case of high-gradient fields was generalized and then the combined effects of dielectrophoresis and field-induced phase transitions in quiescent colloids was considered. It was found that, under certain conditions, dielectrophoresis would be accompanied by a phase transition in a certain portion of the suspension where the pathway representing the local values of the particle concentration and the field strength in the suspension phase diagram, Figure 1.9, would cross the coexistence curve. It was predicted that in this case, the dielectrophoretic force will cause the particles to accumulate in certain regions and, as soon as their local concentration exceeded the critical value, the suspension would undergo a phase transition. Depending on the sign of the particle polarizability, the strength of the electric field in this region would be either high or low. The coupling of these two field-induced

processes was predicted to lead to the formation of a concentrated layer of particles in those regions where, depending on the sign of the particle polarizability, the strength of the electric field is either high or low. In the present work, the kinetics of this phenomenon favorable for many applications are addressed theoretically and experimentally.

A suspension exposed to an electric field so strong that its state corresponds to the unstable domain U in the phase diagram in Figure 1.9 nearly over the entire volume of the system is considered. Then the behavior of the suspension will depend on the ratio of two time scales, τ_a and τ_d. The former refers to the characteristic time for the field-induced structure formation in a suspension subjected to a spatially uniform field whereas the latter is a measure of the time required for a particle to move over a characteristic length of the system, d, under the action of the dielectrophoretic force, Equation (1.19). The time scale τ_a for the structure formation can be estimated by considering the time taken for a particle to move over the interparticle distance under the action of the dipole-dipole attraction and the viscous drag. For a relatively rapid aggregation under conditions where there is no contribution of the conductivity effects to the interparticle interactions and the applied field is sufficiently strong so that particle Brownian motion effects can be neglected (Khusid and Acrivos, 1999), the expression given in (Shapiro et al., 1985, Hass et al., 1993) can be used:

$$\tau_a \approx \frac{\eta_f}{\varepsilon_0 \varepsilon_f (\mathrm{Re}(\beta) E)^2} \xi(\varphi), \qquad \xi \approx 0.4\left[(\pi/6\varphi)^{5/3} - 1\right], \qquad E \sim V_{rms}/d \tag{1.21}$$

where η_f is the viscosity of the suspending fluid, ξ is a coefficient which depends on the volume fraction of the particles and $E \sim V_{rms}/d$ is the field strength with V_{rms} being the

root mean square of the applied ac voltage. The factor $1/\varphi^{1/3}$ in ξ refers to the ratio of the average distance two neighboring particles need to travel in order to aggregate to the particle radius (Shapiro et al., 1985). Using the expression for τ_d, when Brownian motion and gravity effects can be neglected (c.f. Equation (3.5) given in chapter 3), therefore on account of Equation (1.21)

$$\frac{\tau_d}{\tau_a} \approx \frac{3d^2|\mathrm{Re}(\beta)|}{a^2\xi(\varphi)} \tag{1.22}$$

where a is the particle radius.

To-date, all the experimental and theoretical studies of the field-induced structure formation in suspensions have been related to a variety of applications involving electrorheological fluids, for which the particle homogeneous aggregation is the typical regime, i.e., $\tau_d >> \tau_a$. In this case, the macroscopic spatial particle redistribution during the field-induced aggregation is negligible. In contrast, the opposite extreme $\tau_d << \tau_a$ corresponding to the particle heterogeneous aggregation shall be considered here.

CHAPTER 2

AN INTRODUCTION TO THE INSTRUMENTS USED FOR MEASURING VARIOUS PROPERTIES OF THE SUSPENSIONS

2.1 Introduction

In this section, a short description of the instruments and methods, which were used to measure various properties of the suspensions is presented. These measurements are essential and had to be performed before any comparison could be made between the theoretical results and the experimental data.

2.2 BDS 80 Dielectric Spectrometer and WinDETA Software

This instrument was used for the measurement of the dielectric properties of the suspensions and has the major advantages that it can be used for a broad range of frequencies and temperatures. The frequency of the applied field is an important parameter, which can be used for changing the electrical properties of the molecule by changing the polarization as well as for studying the relaxation process in the molecules by changing the test signal.

This instrument can be used for measuring the dielectric and magnetic properties of the material with five free variables: frequency, temperature, AC voltage, time and DC bias, out of which four free variables can be arranged in arbitrary order. For each free variable, the user can create a value list containing up to 1000 points with linear, logarithmic or arbitrary distance between the points. In addition to fixed setpoints, an

arbitrary series of temperature ramps or time intervals for continuous measurements can be defined. Some of the basic features of this instrument include:

- A Frequency range: $10\,\mu Hz \rightarrow 1.8GHz$
- Accuracy: $\tan(\delta) < 10^{-4}$
- An Impedance range: $1Ohm \rightarrow 10^{14}\,Ohm$

This instrument is connected to a computer system, where WinDETA software allows the user to control various parameters for any measurement along with a control over the start and end conditions by setting the free variables to the desired values. During the measurement, the data is displayed on-line as a graph and as a numeric table in a log window. In addition, all the activities of WinDETA and the state of the devices are presented in a message window. Finally, the actual system state is graphically displayed in a status window.

2.3 Particle Counters

These analytical instruments were used for the characterization of the particle size distribution in the suspensions. Two devices were used, specially deigned for two different particle size ranges:

- COULTER® LS™ 230 Enhanced Laser Diffraction Particle Size Analyzer.
- COULTER® N4 Plus™

2.3.1 COULTER® LS™ 230

COULTER® LS™ 230 operates using the Laser Diffraction method, which operates on an optical principle that small particles in the path of a light beam scatter the light in characteristic, symmetrical pattern that can be viewed on a screen. Given a certain pattern of scattered light intensity as a function of angle to the axis of the incident beam ("flux pattern"), the distribution of the particle sizes can be deduced (Figure 2.1)

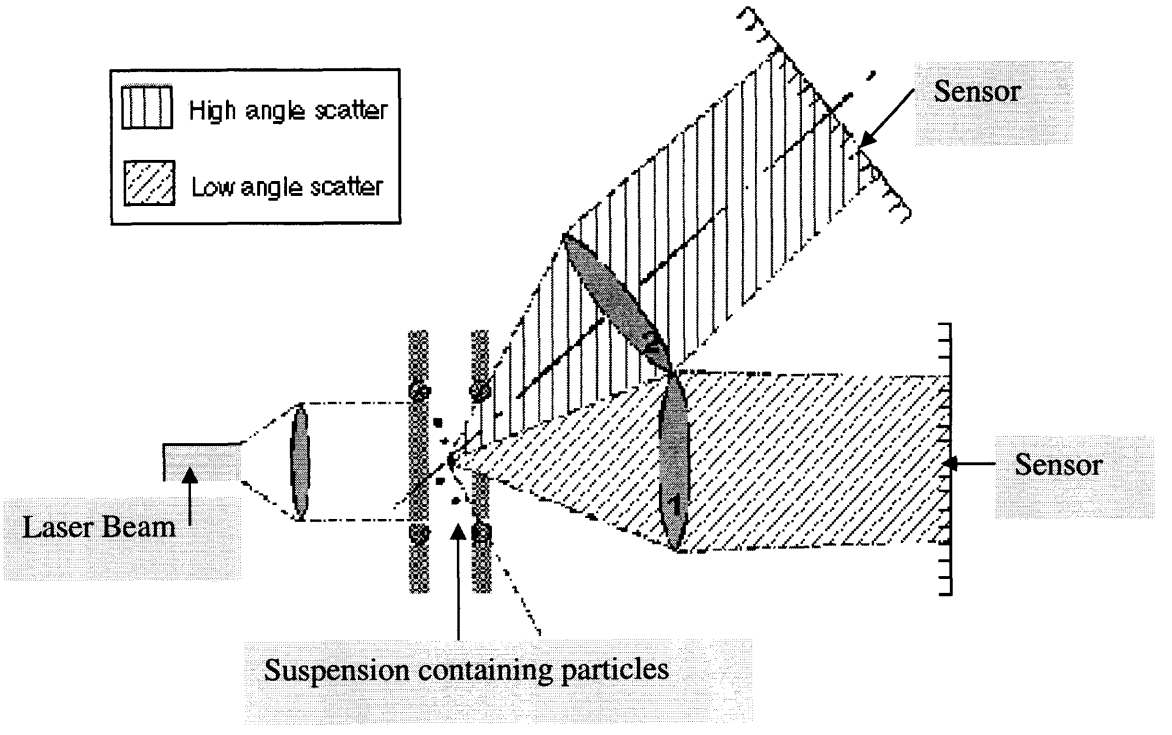

Figure 2.1 Laser Diffraction method (Beckman Coulter).

The simplest flux pattern, that is formed by a monomodal dispersion of spheres, consists of a central bright spot (known as the airy disk), surrounded by concentric dark and bright rings whose intensity diminishes further from the center of the pattern, i.e., at higher scattering angles. The scattering angle, at which the first dark ring, or the diffraction minimum, occurs, depends on the size of the particles, the smaller the particle, the higher the angle of the first dark ring (or, alternatively, the larger the size of the airy disk).

These flux patterns also obey the rule of linear superposition. In other words, the pattern from a mixture of two (or more) monomodal dispersions of the particles can be constructed by adding the intensity functions of the constituent particles in the mixture. The goal of a Laser Diffraction particle size measurement is to measure the flux pattern accurately enough to determine the distribution of the particle size in suspension. This instrument is capable of measuring particle sizes from 0.04μm-2000μm in a single scan, using 116 size channels.

2.3.2 COULTER® N4 Plus™

The COULTER® N4 Plus™ Submicron Particle Size Analyzer is based on Photo-Correlation Spectroscopy method, which is also referred to as dynamic light scattering or quassi-elastic light scattering. This technique is applicable to particles, in a liquid, which exhibit a state of random movement due to Brownian motion (i.e., particles generally of 2-3μm diameter or smaller). The pace of the movement of these particles is inversely proportional to the particle size (the smaller the particle, the faster they move, or diffuse), and the pace can be detected by analyzing the time dependency of the light intensity fluctuations scattered from the particles when they are illuminated with a laser beam.

This instrument is capable of measuring particle size range from 3nm to 3μm. It has one 80-channel multi-tau correlator (the hard-wired computation circuit which characterizes the rate of fluctuations in scattered light intensity) and optimizes resolution across the dynamic range of the instrument.

CHAPTER 3

THEORETICAL AND EXPERIMENTAL STUDIES OF THE FIELD-INDUCED PARTICLE MOTIONS AND HETEROGENEOUS AGGREGATION IN DILUTE SUSPENSIONS OF POSITIVELY POLARIZED PARTICLES SUBJECT TO HIGH – GRADIENT ELECTRIC FIELDS

3.1 Experimental Procedure

A. Electro-hydrodynamic setup

Most of the previous experimental work on electro-hydrodynamics was related to the development of high-throughput apparatuses (Chang et al., 1995; Pohl et al., 1984; Pohl, 1978). However due to the complexity of the geometry, the field configuration and the associated flow patterns of such setups and the poor characterization of the properties of the suspensions used in their experiments, previous investigators were mainly concerned with the productivity of their devices expressed as a function of the applied voltage, the field frequency, the flow rate, the type of particles, etc. Correspondingly, such devices cannot be employed for the quantitative analysis of electro-hydrodynamic phenomena. In contrast to these studies, the electro-hydrodynamic experiments were conducted (Dussaud et al., 2000) in a chamber with well-defined configurations of the electric field and the flow pattern where a flowing suspension was exposed to a strong electric field under conditions such that the electric field lines were arranged in the channel cross-section perpendicular to the streamlines of the main flow. Also, extremely dilute suspensions ($\varphi \sim 10^{-4}$) were employed consisting of low-polarized, neutrally buoyant,

monosized 63-μm hollow ceramic spheres which exhibited negative dielectrophoresis ($\mathrm{Re}(\beta^*) \sim -0.04$). The application of a high-gradient ac field caused these particles to concentrate within thin stripes parallel to the streamlines above the grounded electrodes (regions of a nearly zero electric field) and to travel with the suspending fluid within these stripes. This study provided a quantitative verification of the theoretical expression for the dielectrophoretic force, Equation (1.19), for the case of not perfectly insulating or perfectly conducting systems. Moreover, it demonstrated that, for particles subjected to strong fields (~several kV/mm), Equation (1.16) can employ the value of the particle polarization, β, measured at low field strength (~several V/mm).

It was found, however, that the setup developed in (Dussaud et al., 2000) was limited to experiments on neutrally buoyant suspensions since even a very small density difference between the suspending fluid and the particles caused the latter to sediment. The requirement of zero buoyancy limits severely the choice of suspension constituents and, in particular, the variation of the polarization mismatch between the particles and the suspending fluid that can be achieved. To diminish the effects of the gravitational force, a special setup was designed and fabricated in which the chamber was slowly rotated around a horizontal axis along with a special technique to energize the electrodes (Figure 3.1). In the rotating framework, the gravitational force averaged over the period of rotation equals zero, and a small particle travels with the main flow in a spiral along the channel. The spiral diameter can be estimated by balancing the gravitational and viscous drag forces acting on a particle (chapter 3.3). Most experiments were conducted with the channel rotating at 4 rpm. Under these conditions, the spiral diameter of the particles was

about of 16% of the channel height and their maximum centrifugal acceleration was $5 \cdot 10^{-4}$ g at the channel periphery.

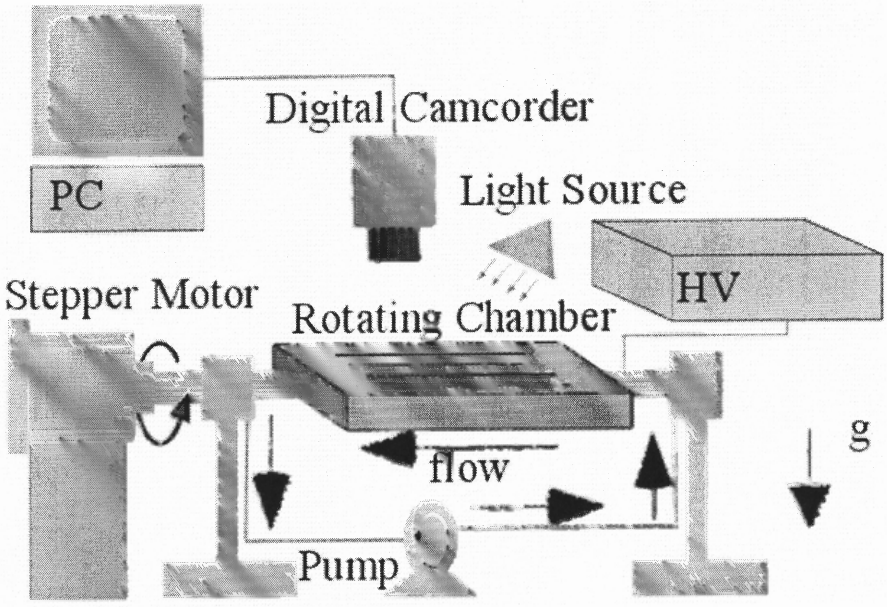

Figure 3.1 Schematic of the experimental setup with a rotating electro-hydrodynamic chamber.

The experiments were performed in a horizontal parallel-plate channel, 6 cm wide, 12 cm long, and 3 mm high (Figure 3.2) made of Acrylic with its top consisting of a glass plate coated with a transparent conducting indium tin oxide film (Gray Glass Co., NY). This film was used to provide a uniform grounding of the top of the channel which, being transparent, allowed to record the particle motions. The glass plate was sealed with a PTFE gasket. The grounding of the channel top gave a well-defined boundary condition for computing the electric field. The bottom of the channel, consisting of a plate 12 mm in thickness, was equipped with 16 linear, flat, electrodes, each 11 cm long and 1.6 mm wide, arranged parallel to the flow in order to generate the electric field configuration similar to that in (Dussaud et al., 2000). The electrodes made from square brass tubes were embedded into 1.6-mm deep groves at 2 mm intervals and the electrode edges were smoothed to suppress sparking.

To generate a high-gradient electric field, these electrodes were alternately energized and grounded via copper wires which were connected to a pair of brass cylinders separated by a 1-cm thick insulating plate. This whole device was allowed to rotate around the horizontal axis, as was the case with the channel. Every cylinder was equipped with a brass wire embedded into a grove (5 mm deep and 5 mm wide) machined around it and the ends of each brass wire were fixed to an insulating plastic plate. These wires were used to apply a high-voltage electric field to the electrodes. Sliding easily over the inner surface of the grooves, these wires maintained good electric contact with the rotating cylinders without sparking. The applied ac field, the frequency and the amplitude of which varied from 100 Hz to 1000 Hz and from 1 kV to 5 kV rms

(the root mean square), was produced with a high-voltage amplifier (Model 10/40, Trek Inc., New York). By operating at such frequencies and voltages, electrophoresis and electro-convection in the pure suspending fluid was eliminated, but dielectrophoresis and structure formation was allowed to operate within the suspension. A Laser Doppler technique for measuring the fluid velocity was used to probe for the possible presence of electro-convection in the pure suspending liquid.

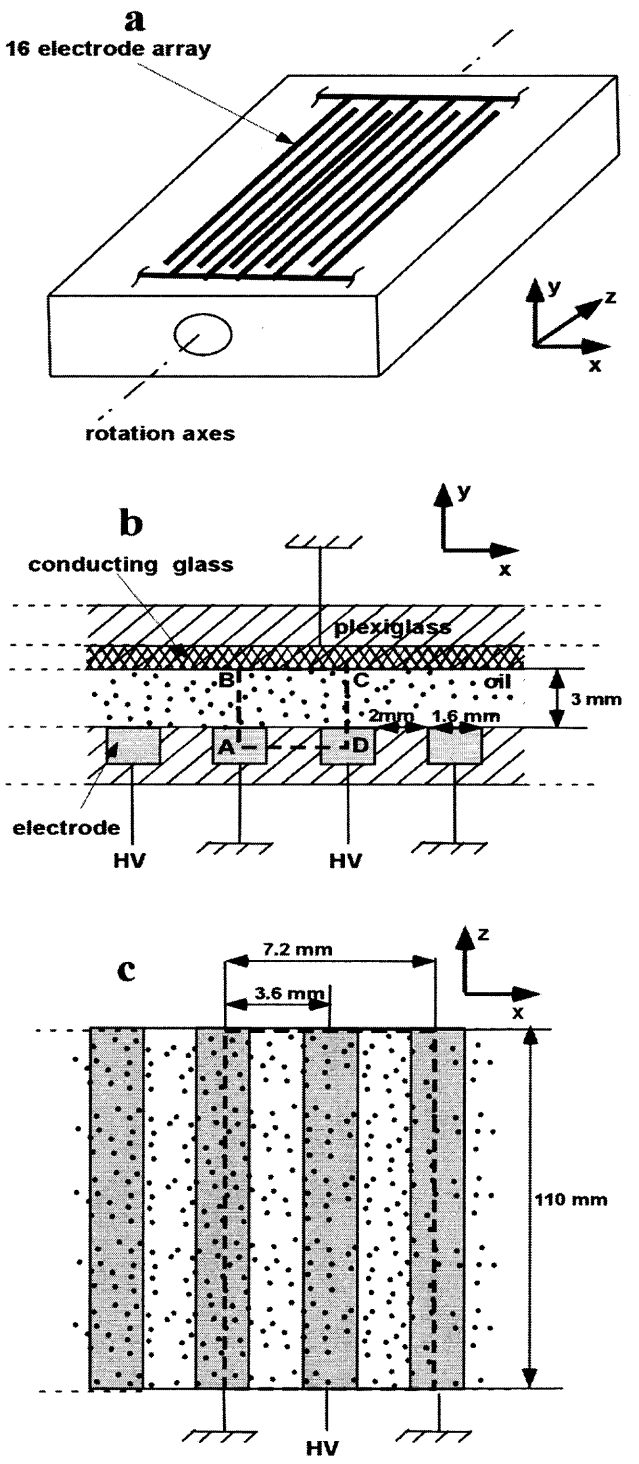

Figure 3.2 (a) The parallel-plate channel equipped with an electrode array. (b) Cross-sectional view of the channel and the electrode-assembly details. (c) Top view of the channel.

To rotate the channel a step motor with a step controller (SmartStep, IDC, CA) was used, which was programmed to bring the channel instantaneously at preset positions. This allows to acquire high quality images of the spatial particle distribution in the channel. To flow the suspension parallel to the electrodes, a peristaltic pump which was fitted with a pulsation dampener (Cole-Parmer) and was connected to the rotating channel through a pair of swivel fittings (Figure 3.1) was used. The experiments were performed at 23°C.

A spread cone light beam from a strong light source (MHF-G150LR, Moritex, Japan) was used to illuminate the suspension through the transparent top plate at an angle of about 30^0 relative to the horizontal plane with the electrodes (Figure 3.1). The particle motions and their segregation were recorded also through the top plate by a digital camera (PV-DV950 camera, AG-1960 VCR, both Panasonic) equipped with 48-mm F-1.6 lens. The camera was oriented perpendicularly to the channel axis and was focused on the electrode array (Figure 3.1). To examine different regions of the channel, the camera was mounted on a translation stage. Continuous recordings of the particle behavior in the rotating channel were conducted and, as needed, pictures of the particle distribution by bringing the channel at the preset positions so as to have the camera aimed at the channel top plate were taken.

B. Materials

The suspension consisted of a fraction of sieved aluminum oxide spherical particles (AL-604, 99.9%, AEE, NJ) suspended in Mazola corn oil. The particle size distribution of this fraction was measured with a Beckman-Coulter Laser Diffraction Particle Size Analyzer LS 230. The average diameter of the particles was 89.6 μm, and 50% of the particles had diameters between 69 μm and 107 μm. The particle density was 3.75 g/cm^3. The density of the corn oil was 0.92 g/cm^3 and its viscosity was 59.7 cp at 23°C.

To measure the complex permittivity of the suspensions and that of the continuous phase, the standard technique of dielectric spectroscopy (Hill et al., 1969) was used. The measurements were performed on a Broadband Dielectric Spectrometer (BDS)-80 (Novocontrol, GmBH) in a spatially uniform low electric field (~ 4 V/mm) in the range of frequencies from 0.1 Hz to 7 MHz. Using the BDS-80 thermostat, the specimen temperature was kept at 23.00 ± 0.01 °C during the measurements. The dielectric sample cell consisted of a round plate capacitor (D=20 mm) filled with the specimen, and the cell constant was determined with pure hexadecane (Aldrich, 99%+). For the dielectric measurements, the concentration of the suspension varied from 5% to 25% by volume. The high sensitivity of the BDS-80 enabled to conduct reproducible measurements on 5-% suspensions when the relative difference between the dielectric permittivities of the specimen and the continuous phase was at least 5%. To calculate the particle polarizability an approach validated in (Dussaud et al.,) was used. Specifically, the concentration and frequency dependence of the suspension complex dielectric permittivity, ε_s^*, was measured, and then β was computed by employing the Maxwell-Wagner expression for ε_s^* of a suspension of randomly distributed spherical particles

(Equation1.20, chapter 1.2)

The main difficulty in measuring β^* for the aluminum oxide particles dispersed in the corn oil was that the former settled in the dielectric cell filled with the specimen before the dielectric measurements could be conducted. To overcome this limitation, a very viscous homogeneous fluid was prepared, which had nearly the same complex dielectric permittivity as that of the pure corn oil and then it was used as the continuous phase in the suspensions for the dielectric measurements. After testing several materials, a mixture of the corn oil with 5.2% (by weight) of bee's wax (Van Dyke's, SD) was chosen. To prepare this suspending fluid, the mixture was slowly heated (~0.2^0C/min) while continuously stirring it in a magnetic stirrer until the wax had melted. Heating the mixture was kept for another 30 minutes and then slowly cooled to room temperature. The frequency dependence of the complex dielectric permittivities of the suspending fluid and that of the pure corn oil at 23^0C coincided in the range of frequencies from 10 Hz to 0.1 MHz, which was significantly broader than that used in previously described electro-hydrodynamic experiments. Aluminum oxide particles were then dispersed in this very viscous fluid by rotating a bottle at 6 rpm. The gravitational settling of the former was so slow that no discernible settlement could be detected in a couple of days.

The concentration dependence of the real part of the ratio $\left(\varepsilon_s^* - \varepsilon_f^*\right)/\left(\varepsilon_s^* + 2\varepsilon_f^*\right)$ for several frequencies is shown in Figure 3.3(a), from which the real part of the particle polarizability and its frequency dependence, shown in Figure 3.3(b), were calculated using Equation (1.20) (chapter 1.2).

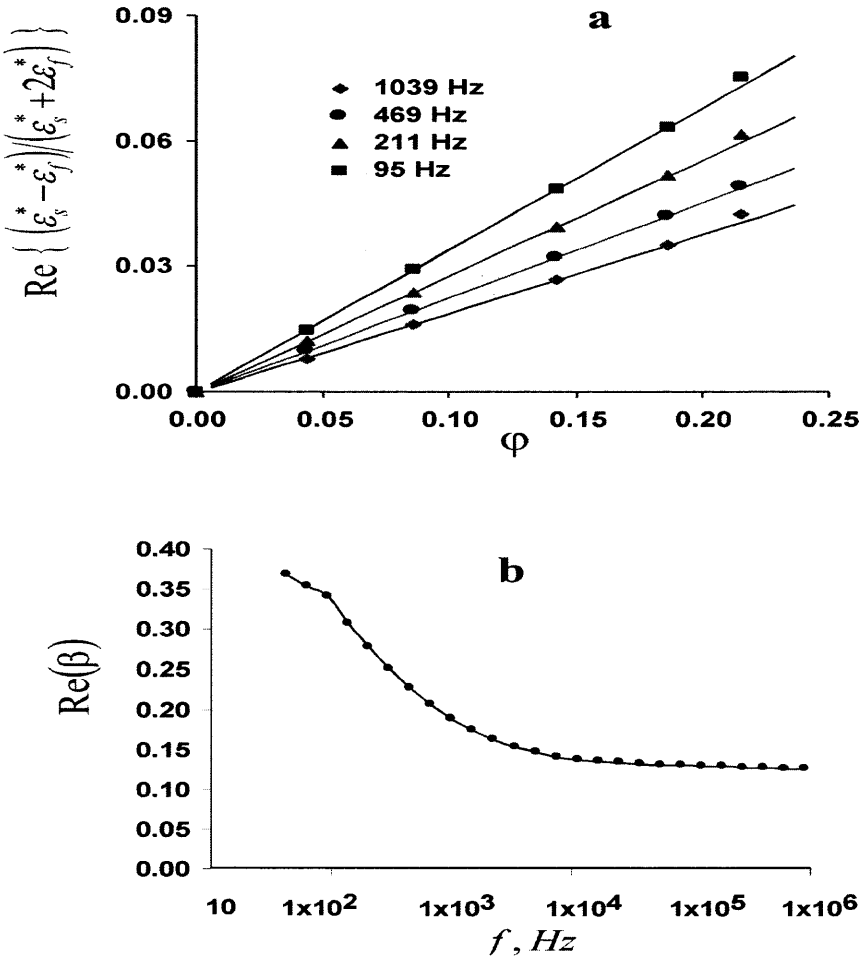

Figure 3.3 (a) The dependence of the real part of $(\varepsilon_s^* - \varepsilon_f^*)/(\varepsilon_s^* + 2\varepsilon_f^*)$ on the particle volume concentration, φ. (b) The frequency dependence of the real part of the particle polarization, $\mathrm{Re}(\beta^*)$.

C. Procedures

Experiments

The setup was prepared for each experiment in several steps. First the vertically arranged channel was slowly filled with the pure corn oil from the bottom to the top and was kept in this position for about two hours to remove any trapped air bubbles. Then the channel was placed in the setup and set into rotation. The corn oil was next displaced by the suspension which was slowly pumped into the rotating channel from a reservoir equipped with a magnetic stirrer. The channel electrodes were energized after 30 min following the displacement of the corn oil. Flowing experiments were performed by continuously cycling a fixed volume of a suspension (nearly equal to the channel volume) through the rotating channel in which the suspension was exposed to an electric field.

To diminish the effects of the centrifugal force, the data on the particle motions and segregation were taken at the middle of the channel where the centrifugal acceleration was about ten times lower than at its periphery. In order to clean the channel between each series of experiments, the pure corn oil was pumped through the de-energized rotating channel.

Image analysis

On the images acquired through the channel top, the Al_2O_3 particles appeared as shiny dots due to the light being scattered by them. The relative changes of the distribution of the gray level (GL) on consecutive black & white images taken at equal time steps were used to estimate the kinetics of the field-induced particle motions and their segregation. The GL of a pixel, defined as the relative local brightness, have a maximum range from 0

(black) to 255 (white). The images were analyzed using the VISILOG-5 (Noesis, Inc.) image analysis software. VISILOG-5 allows one to collect the readings of GL over a selected rectangular box on an image and calculate the average. The average value of GL/255 represents the white fraction on a selected area. VISILOG-5 also provides a procedure for measuring the variation of the white fraction along a selected line parallel to one of the box sides. Here, for every point on this line, the software takes the readings of GL through the box in the direction perpendicular to the line and calculates their average.

Photos were taken of a sediment formed on the bottom of the channel by the gravitational settling of initially uniformly suspended particles in order to evaluate the relation between the amount of the segregated particles and the GL. The experiments were conducted on initially very dilute suspensions with particle concentrations $\varphi = (1-15)\cdot 10^{-3}$. This range in ϕ was chosen because a particle number balance shows that, under these conditions, it is possible to accommodate all the settled particles into a single-particle layer at the bottom of the channel. Next, the rotating channel (Figure 3.1) was slowly filled with the suspension so that the suspended particles were uniformly distributed. Then, when the plane with the electrodes was horizontal, the rotation was stopped and the particles were allowed to settle. The images of the sediment layers are presented in Figures 3.4(a)-3.4(d). To measure the GL of the sediment, the electrode edge was surrounded by a box the dimensions and location of which were similar to those used later in the field-related experiments. The data reported in Figure 3.4(e) indicate that the difference between the GL of a sediment and that of the pure liquid increases with increasing particle concentration in the suspension but then gradually saturates most

likely due to the formation of a partially multi-layered sediment. Nevertheless, the data in Figure 3.4e demonstrate that an increase in the GL can be considered as an acceptable parameter to qualitatively represent the increase in the amount of the segregated particles.

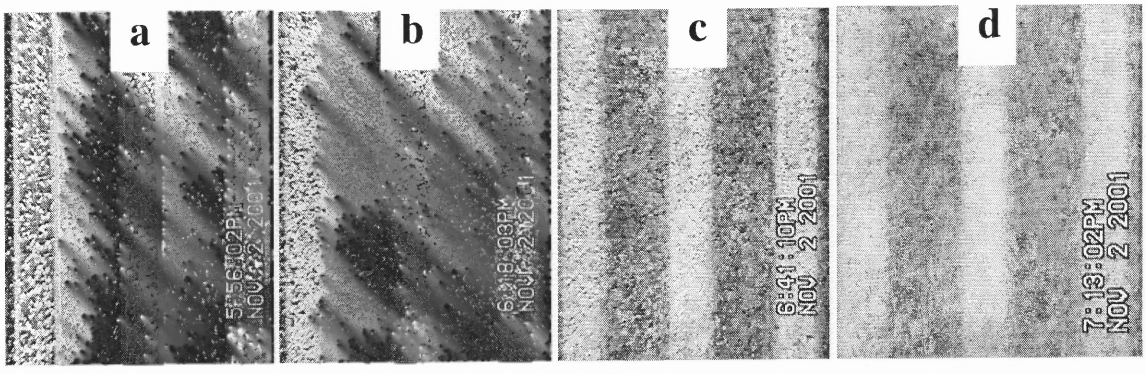

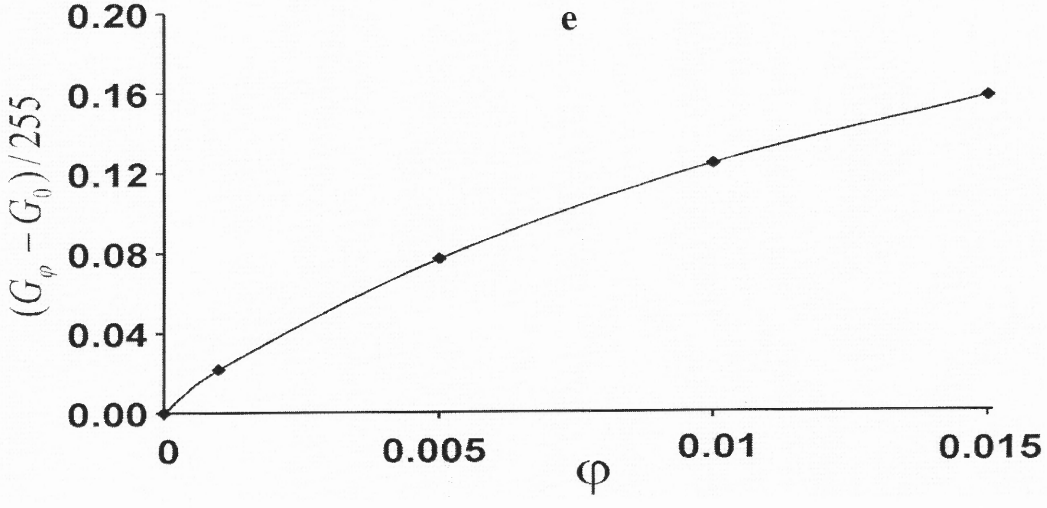

Figure 3.4 The sediment layers formed by the gravitational settling of particles in suspensions with particle concentrations (v/v): (a) 10^{-3}, (b) $5 \cdot 10^{-3}$, (c) 10^{-2}, (d) $1.5 \cdot 10^{-2}$ following the cessation of the channel rotation. (e) The dependence on particle concentration (v/v) of the difference between the GL of a sediment and that of the pure liquid.

With this in mind, changes in the white fraction in a selected area on black & white images were also used to characterize the field-induced segregation of the particles on the electrode edges in initially dilute suspensions with $\varphi \leq 10^{-3}$. In the experiments without flow, the value of GL was tracked, averaged over a selected box surrounding the electrode edge, as a function of the time the suspension had been exposed to the field. The width of the box, 0.7 mm, was chosen so that it covered the particle layer and its length was typically about 7 mm which was large enough to reduce the fluctuations in the data. The value of $(GL(t)-GL_0)$ with GL_0 being the initial value was considered as representing the amount of particles that had segregated on the electrode edge following the application of the field. On the other hand, in flowing experiments, the longitudinal variation of $(GL-GL_0)$ along a rectangular box surrounding the whole electrode was measured in order to characterize the non-uniformity of the steady-state particle distribution in the flow direction. To reduce the fluctuations in the data, a sliding averaging of the readings was performed over a length of 1 mm along the channel axis.

It is worth noting that a particle number balance for a suspension with $\varphi = 10^{-3}$ shows that if all the suspended particles, after having settled, had been joined together to form single-particle lines along the electrode edge, a structure would have been built up consisting of about two lines of particles placed next to one another along the electric field lines. This indicates that an increase in the GL following the application of a field provides an accepted quantitative measure of the amount of the segregated particles for $\varphi \leq 10^{-3}$.

3.2 Single – Particle Model for Dielectrophoresis in a Rotating Channel

First, the main dimensionless parameters characterizing the suspension flow in a rotating system for experimental conditions were evaluated. The local fluid velocity along the channel, $\mathbf{v}_f$, was $\sim 2\,\mathrm{mm/s}$, the particle velocity relative to the fluid, $\mathbf{u}-\mathbf{v}_f$, varied from $\sim 15\,\mu\mathrm{m/s}$ to $\sim 150\,\mu\mathrm{m/s}$, and the channel angular velocity, Ω, was maintained at $\sim 0.4\,\mathrm{s}^{-1}$. The thickness of the so-called Ekman layer (Ungarish, 1993) in which a fluid co-rotates with a solid wall due to viscous forces is $\delta_E = (\eta_f/\rho_f\Omega)^{1/2}$ with ρ_f and η_f being the fluid density and viscosity, respectively. Since δ_E, being about 12 mm for these experiments, exceeded the channel gap, H = 3 mm, it can safely assumed that the suspending fluid was fully co-rotating with the channel. The body force operating in a framework rotating with the channel includes the gravity, centrifugal, and Coriolis components. The Froude number (Ungarish, 1993) $\mathrm{Fr} = \Omega^2 b/g$, where g is the gravitational acceleration and b is a typical distance from the axis of rotation, provides a means of the ratio between the centrifugal and gravity forces. Fr was found to be $\sim 5\cdot 10^{-5}$ for $b = H$ and $\sim 5\cdot 10^{-4}$ at the channel periphery for b= 3 cm (see Figure 3.2). As for the Coriolis force effects, these could lead to the generation of a secondary fluid flow perpendicular to the rotation axis. Taking v_f for the magnitude of the fluid velocity in a secondary flow, which actually overestimates it, yields $\sim 1.5\cdot 10^{-4}$ for the ratio $2\Omega v_f/g$ between the Coriolis and gravity forces. Both these estimates indicate that the contribution of the rotation effects to the body force operating in a framework rotating with the channel was insignificant.

The Reynolds numbers for the fluid flow and for the relative particle motion are defined as (Ungarish, 1993) $\mathrm{Re}_f = \rho_f v_f H/\eta_f$ and $\mathrm{Re}_p = \rho_f U_p a/\eta_f$, respectively, where U_p typifies the relative particle velocity and a is the particle radius. For these experiments, $\mathrm{Re}_f \sim 0.08$ and $\mathrm{Re}_p \sim 10^{-5} - 10^{-4}$. The square of the ratio between the thickness of the viscous Ekman layer and the particle radius expressed by the modified Taylor number (Ungarish, 1993) $\mathrm{Ta} = 2\rho_f \Omega a^2/9\eta_f$ represents the contribution of the rotation effects to the viscous force exerted on a particle moving in a slowly rotating fluid at $\mathrm{Re}_p << 1$. The equations given in Sec. 3.8 of (Ungarish, 1993) indicate that the relative contribution of these effects to the conventional Stokes drag force is proportional to $\sqrt{\mathrm{Ta}}$ which is therefore insignificant in these experiments given that *Ta* was of order 10^{-6}.

To evaluate the importance of Brownian diffusion of the dispersed particles, consider the particle displacement, $\Delta_D \sim \sqrt{D_{Br} t_{exp}}$, over the characteristic time, t_{exp}, of these experiments, where $D_{Br} = \dfrac{k_B T}{6\pi\eta_f a}$ is the diffusion coefficient of a particle. Taking $t_{exp} \sim 1\mathrm{h}$, $\Delta_D \sim 0.5\mu\mathrm{m}$ was obtained, which clearly demonstrates that particle Brownian motion effects were insignificant.

A single-particle model considers only the external forces exerting on a particle and ignores all interparticle interactions. Consider then a framework rotating with the channel. By neglecting Brownian motion, centrifugal and Coriolis forces and balancing the dielectrophoretic force, Equation (1.19), the conventional Stokes drag force, and the gravitational force, for the particle velocity, $\mathbf{u}$, was obtained:

$$6\pi\eta_f a[\mathbf{u}-\mathbf{v}_f(\mathbf{r})]=2\pi\varepsilon_0\varepsilon_f a^3\,\mathrm{Re}(\beta)\nabla E_{rms}^2(\mathbf{r})+\frac{4}{3}\pi(\rho_p-\rho_f)a^3\mathbf{g}e(t) \qquad (3.1)$$

where ρ_p is the particle density and $\mathbf{e}$ is a rotating unit vector along the orientation of the gravity force. To compute the term ∇E_{rms}^2 generated by the electrodes, Laplace's equation for the channel needs to be solve. The field-induced displacement $\mathbf{r}(t)$ of a particle being initially at $\mathbf{r}_0$ is obtained by solving the equation

$$\frac{d\mathbf{r}}{dt}=\mathbf{u} \qquad \mathbf{r}\big|_{t=0}=\mathbf{r}_0 \qquad (3.2)$$

As expected, a single-particle model was found (Dussaud et al., 2000) to describe quantitatively particle segregation in a dilute suspension of negatively polarized particles because such particles accumulate in a low field region where the role of the interparticle electric interactions decreases as this region is approached. In chapter 3.3, the extent to which the model can be applied to the segregation of positively polarized particles which are attracted towards a high field region where the role of their interactions increases progressively as they accumulate there will be considered.

The setup (Figure 3.2) was designed so that the vectors ∇E_{rms}^2 and $\mathbf{e}$ were directed normal to the channel axis whereas $\mathbf{v}_f$, appearing in the flowing experiments, was along the channel axis. In this case, the particle velocity relative to that of fluid, $\mathbf{u}-\mathbf{v}_f$, had components only along the x- and y-directions in the channel cross-section.

The gap between the electrodes was very small with respect to their length in the z-direction, so that the field could be taken as two dimensional, varying only along the cross-section of the channel in the x- and y-directions. Furthermore, because of the symmetry and periodicity of the electrode array in the x-direction, the electric field was

computed only for the element ABCD enclosed by the dashed line in Figure 3.2(b) with the sides having insulating boundaries (by symmetry) and the top grounded. The oil and the channel bottom plate were assumed to form a continuous medium because of their similar electrical properties. The part of the bottom boundary AD of the computational box between the electrodes was taken to be insulating. In fact, the conditions for the field on this line is not important since, if this line was taken as being grounded, which is another extreme boundary condition, the maximum field strength in the oil changed by less than 2% (Dussaud et al., 2000). The numerical procedure used to solve Laplace's equation was described in (Dussaud et al., 2000). The distribution of the field strength between the centers of neighboring grounded ($0 \leq x \leq 0.8$mm) and high-voltage ($2.8 \leq x \leq 3.6$mm) electrodes is depicted in Figure 3.5. Notice that the region of the highest field strength is located at the edges of the electrodes and that of its lowest strength is above the center of the grounded electrode near the midplane of the channel. Therefore, the application of an electric field to the suspension should cause the positively polarized particles to segregate on the electrode edges.

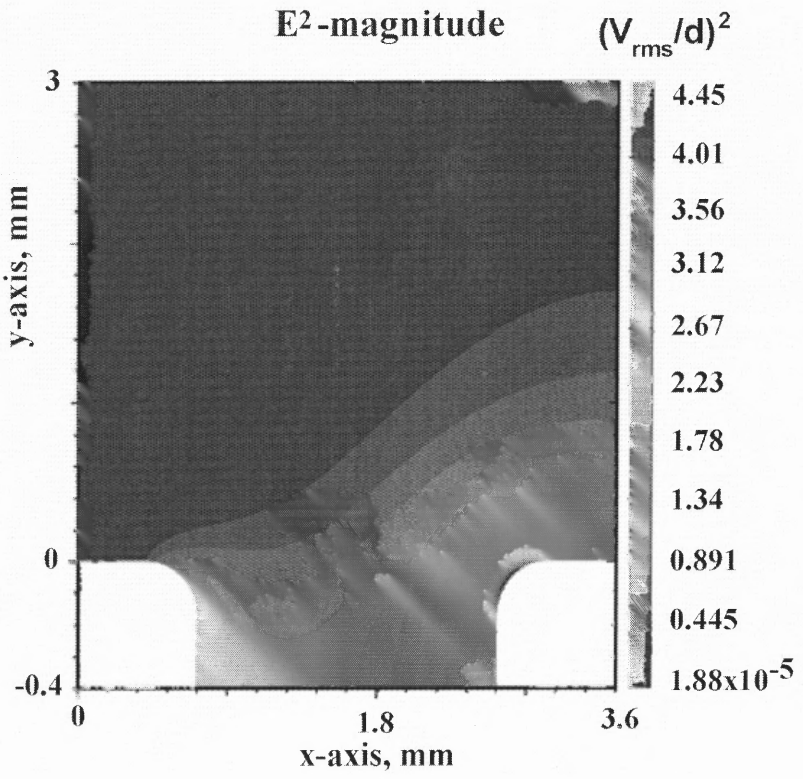

Figure 3.5 The distribution of the square of the field strength, E^2, (expressed in units of V_{rms}^2/d^2) in the element enclosed by the dashed line in Figure 3(b). Grounded and energized electrodes are on the left and on the right, respectively. The top is also grounded.

For a suspension flowing through the rotating channel (Figure 3.2(a)), the fully developed fluid velocity has only a component in the z-direction, $v_{fz}(y)$, given by the well-known expression for the velocity profile in a parallel-plate channel (Batchelor, 1993)

$$v_{fz} = 6U_a \frac{y}{H}\left(1-\frac{y}{H}\right) \qquad U_a = \frac{Q}{A} \tag{3.3}$$

where U_a is the average fluid velocity, Q is the volumetric flow rate, and A is the area of the channel cross section. Since $Re_f << 1$, the entrance length required for a flow to reach the velocity profile given by Equation (3.3) is of the order of the channel gap.

Now consider Equations (3.1)–(3.3) in more detail. Using these equations, it is easy to show that, in the absence of the electric field and without flow, a particle, away from the boundaries, will rotate in a circular orbit with the channel angular velocity Ω. In these experiments, the ratio of the orbit radius, R, to the channel height,

$$\frac{R}{H}=\frac{2(\rho_p-\rho_f)ga^2}{9\eta_f\Omega H} \tag{3.4}$$

was about 0.16 at a rotation speed of 4 rpm.

Next, consider the relative effects of the dielectrophoretic and gravitational forces on the particle motion. Given that ∇E_{rms}^2 is $O\left(V_{rms}^2/d^3\right)$ where d is the gap between neighboring electrodes, it is obtained that the components of the particle velocity in the channel cross-section are $O(d/\tau_d)$ where, on account of Equation (3.1), τ_d, the characteristic time of the dielectrophoresis is given by

$$\tau_d=\frac{3d^4\eta_f}{a^2\varepsilon_0\varepsilon_f|\mathrm{Re}(\beta^*)|V_{rms}^2} \tag{3.5}$$

In addition, the ratio of the gravitational and dielectrophoretic forces in Equation (3.1) is specified by the parameter

$$G=\frac{2(\rho_p-\rho_f)gd^3}{3\varepsilon_0\varepsilon_f|\mathrm{Re}(\beta^*)|V_{rms}^2} \tag{3.6}$$

When the period of the channel rotation is significantly less than the time scale of the field induced particle segregation, $\Omega\tau_d >> 2\pi$, which occurs at a relatively low field strength, the particle motion over a period of rotation can be average and since, in this case, the average gravity force vanishes, the average particle trajectory is governed by the dielectrophoretic force in Equation (3.1). At the opposite extreme of a high field strength,

$\Omega\tau_d << 2\pi$, the gravitational force in Equation (3.1) can be clearly neglected, in which case the Equation (3.5) for the characteristic time of the dielectrophoresis is also obtained. Hence in Sec. 3.5, τ_d was used as a time scale for the presentation of all the experimental and computational data regarding the particle segregation.

Now consider a suspension flowing through a rotating channel and let $z = 0$ and $z = L$ correspond to the channel inlet and outlet cross-sections, respectively. Since, as was said earlier, the fully developed flow direction is perpendicular to the plane of the field lines, the flow does not affect the particle velocity components in the x- and y-directions, while the field does not affect the particle velocity component in the z-direction. Hence, a particle travels along the channel with the local fluid velocity, $v_{fz}(y)$, given by Equation (3.3). At a given distance z in the channel, the particle distribution then depends on both the dielectrophoresis and the dispersion of the *residence times* (the time that a particle spends in a channel) due to the parabolic flow profile. Specifically, a particle which is initially at the point (x_0, y_0, z_0) will be captured in the channel only if

$$\frac{L - z_0}{6U_a} > \int_0^{t_d(x_0, y_0)} \frac{y}{H}\left(1 - \frac{y}{H}\right)dt \qquad (3.7)$$

where $t_d(x_0, y_0)$. the time required for the particle to reach one of the electrodes, depends only on the initial x and y coordinates of this particle. Moreover, on making use of Equation (3.7) for $z_0 = 0$, that part of the inlet cross-section can be determined, such that a particle entering through this region will not have been trapped on the electrodes. Clearly, this part includes all the points $\{x_0, y_0\}$ for which

$$\frac{L}{6U_a} \leq \int_0^{t_d(x_0, y_0)} \frac{y}{H}\left(1 - \frac{y}{H}\right)dt \qquad (3.8)$$

Let A_e be the area of this region. Then, for a uniform inlet particle distribution, the fraction of particles passing through the channel without being captured equals A_e/A which depends on the channel length and the fluid flow rate only through the average fluid residence time, $T = L/U_a$.

To simulate the field-induced particle segregation, Equations (3.1) – (3.3) were solved for each of N non-interacting particles initially, at $t = 0$, randomly distributed in the simulation cell. The particle motion following the application of an electric field, for $t > 0$, was computed for a rectangular cell bounded by two planes passing along the center lines of two grounded electrodes and the inlet and outlet channel cross-sections (Figure 3.2(c)). A particle leaving the cell through one of its longitudinal sides parallel to the yz plane was replaced by its mirror image (the same y and z coordinates) that simultaneously entered the cell through the other side. Also, in line with the conditions of the flowing experiments, a particle leaving the cell through the outlet cross-section was replaced by another particle that simultaneously entered the cell through the inlet channel cross section at a point with, however, randomly taken y and x coordinates. Particles located on the top and the bottom of the channel were not allowed to exit the cell, so that their outward velocity components were ignored. Once a particle came to the electrode edges it was considered to have been trapped and its further displacement was not computed. The numerical procedure used to solve Equations (3.1) –(3.3), which requires the calculation of ∇E_{rms}^2 at any point, was described in (Dussaud et al., 2000). Simulations were performed using a finite element code from a library of C++ subroutines DIFFPACK, developed at the University of Oslo, Norway (Langtangen, 1999). A typical simulation included N = 4800 particles.

3.3 Experimental Data and Comparison with Simulations

A. Particle segregation in rotating suspensions

The rotating channel (Figure 3.1) was slowly filled with a suspension. Then an electric field was applied to this suspension, while maintaining the clockwise rotation speed at 4 rpm, and recorded the motion of the particles until all of them were captured on the electrodes. The field was first applied at the moment when the plane with the electrodes was horizontal. the effect of particle concentration on the field-induced structure formation in suspensions subjected to high-gradient strong electric fields was considered first. Experiments were conducted on suspensions with particle concentrations $\varphi = 10^{-4}, 10^{-3}$, and 10^{-2} exposed to an ac electric field of $V_{rms} = 3$ kV, 100 Hz. For this voltage, $E \sim V_{rms}/d \sim 1.5$ kV/mm and $\lambda = \varepsilon_0 \varepsilon_f E^2 v_p / k_B T = 5.3 \cdot 10^9$. To locate the state of these suspensions on the phase diagram, Figure 1.9, an asymptotic expression for the spinodal at low particle concentrations (Khusid and Acrivos, 1995; Khusid and Acrivos, 1999) was taken

$$\varphi \lambda \Psi_\omega \approx 1 \tag{3.9}$$

where the function Ψ_ω presents the dependence of the electric energy of the interparticle interactions on the field frequency, the electric properties of the particle and the suspending fluid; a rough estimate $\Psi_\omega \sim 3\,\mathrm{Re}(\beta)^2$ yields 0.34 for 100 Hz (see Figure 3.3(b)). Therefore, under these experimental conditions, the left-hand side of Equation (3.9) will be larger than unity when $\varphi \geq 6 \cdot 10^{-10}$. Correspondingly, the states of the suspensions with $\varphi = 10^{-4}$, 10^{-3}, and 10^{-2} fell into the unstable domain U of the phase

diagram in Figure 1.9 suggesting that the particles should aggregate following the application of a spatially uniform ac field of this strength.

Next, the time scales of the field-induced structure formation and dielectrophoresis are estimated. Using Equations (1.21) and (3.5), $\tau_d = 18.5$ s and $\tau_a = 6 \cdot 10^3$ s, 126s, and 2.7s, for $\varphi = 10^{-4}$, 10^{-3}, and 10^{-2}, are obtained respectively. Hence, the rate of the dielectrophoretic particle redistribution compared with the rate of the phase separation in the bulk appears to be slower for $\varphi = 10^{-2}$ and significantly faster for $\varphi = 10^{-3}$ and 10^{-4}. Presented in Figure 3.6, are photos of the structures formed in the suspensions with $\varphi = 10^{-4}$, 10^{-3}, and 10^{-2}, taken at t= 942s, 312s, and 83s, respectively, following the application of an electric field with $V_{rms} = 3$ kV, 100 Hz, which confirm this prediction. Specifically, in contrast to the case with $\varphi = 10^{-2}$, the suspensions with lower concentrations exhibited heterogeneous aggregation when $\tau_d << \tau_a$, so that the particles aggregated on the electrode edges following their accumulation in these regions caused by dielectrophoresis.

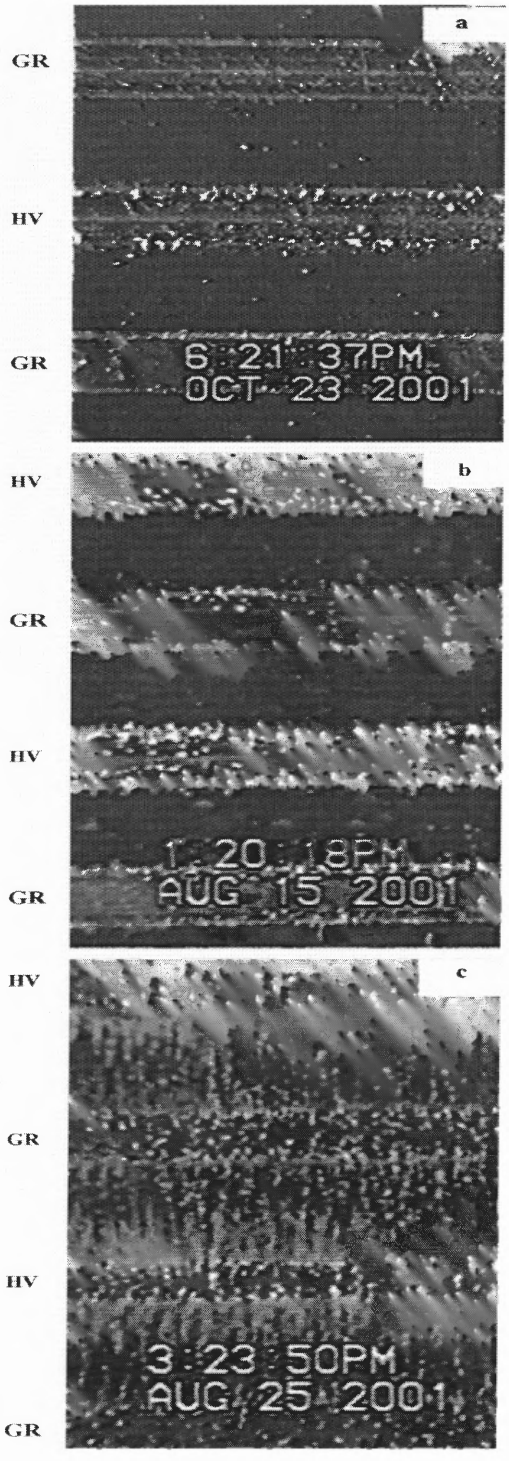

Figure 3.6 The structures formed on the high-voltage (HV) and grounded (GR) electrodes in suspensions with initial particle concentrations (a) 10^{-4}, (b) 10^{-3}, and (c) 10^{-2} (v/v) taken at t= 942s, 312s, and 83s, respectively, following the application of a field with V_{rms} = 3 kV , 100 Hz ; rotation speed 4 rpm. The electrode width is 1.6 mm.

Since the condition for the field-induced heterogeneous aggregation to occur is independent of the applied voltage, Equation (1.22), the effects of the field amplitude and frequency on this phenomenon on a suspension with $\varphi = 10^{-3}$ are chosen to study. V_{rms} from 1 kV to 5 kV at 100 Hz was varied and the frequency from 100 Hz to 1 kHz at $V_{rms} = 3$ kV, while maintaining the rotation speed at 4 rpm. To compare the predictions of a single-particle model with experimental data, the field-induced time evolution of an initially random distribution of particles was computed by taking the value of $\mathrm{Re}(\beta)$ corresponding to the frequency of the applied field (Figure 3.3(b)).

Figures 3.7(a)-(d) present the photos of the field-induced time evolution of an initially uniform distribution of particles in a suspension with $\varphi = 10^{-3}$ following the application of a field with $V_{rms} = 3$ kV, 100 Hz.

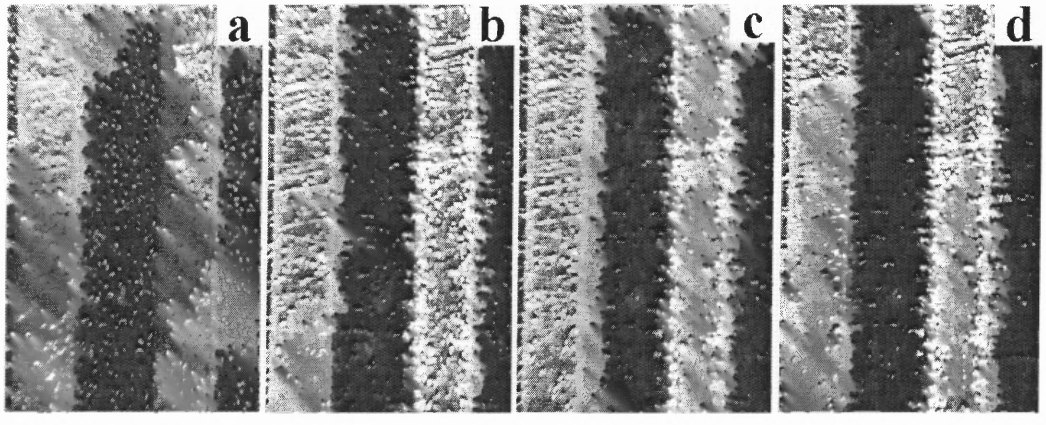

Figure 3.7 The particle distribution in a suspension with 10^{-3} (v/v) particle concentration (a) before and (b)-(d) following the application of a field ($V_{rms} = 3$ kV, 100 Hz) at t= 0 (b) 42s, (c) 119s, and (d) 238s; rotation speed 4 rpm. Grounded and energized electrodes are on the left and on the right, respectively. The electrode width is 1.6 mm.

For comparison, in Figures 3.8(a)-(e) the results of the simulations of the particle motions are shown under the same conditions as would be observed through the channel top (i.e., only their x and z coordinates) and through the channel cross section (i.e., only their x and y coordinates). The computed particle positions are depicted for a region between the centers of neighboring grounded ($0 \leq x \leq 0.8$mm) and high-voltage ($2.8 \leq x \leq 3.6$mm) electrodes.

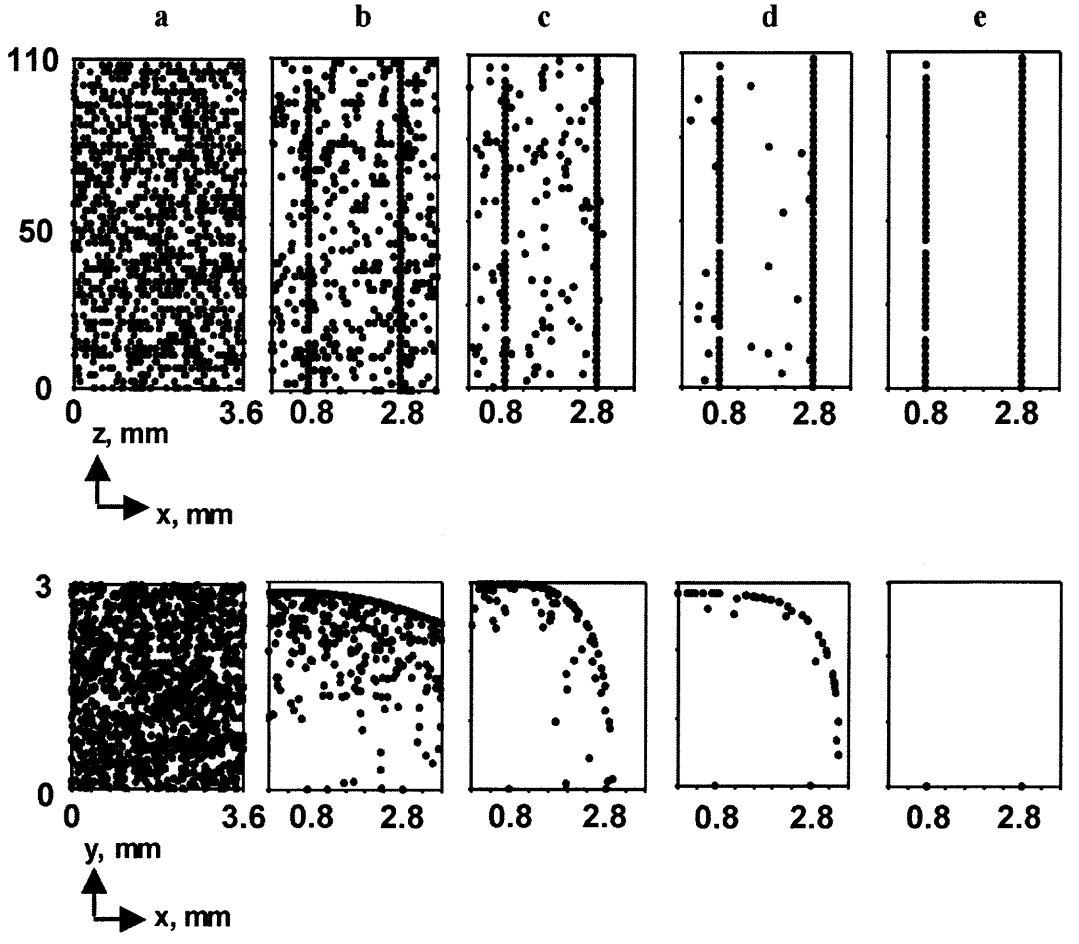

Figure 3.8 Simulation of the field-induced particle motions under the same conditions as those for Figure 3.7; $G = 1.9$, $\Omega\tau_d = 7.75$. Depicted are the particle distributions to be observed through the channel top (their x and z coordinates, mm) and through the channel cross section (their x and y coordinates, mm) at t/τ_d = (a) 0, (b) 2.5 (t = 46 sec), (c) 6.5 (t = 119.6 sec), (d) 13 (t = 239.2 sec), (e) 32 (t = 588.8 sec). Grounded and energized electrodes are on the left and on the right, respectively.

The random particle distribution before the electric field was applied is shown in Figure 3.7(a). At early times after the application of the field, particles are seen to have moved towards the edges of both the high-voltage and the grounded electrodes (Figure 3.7(b)) consistent with the simulations shown in Figure 3.8(b). After 2 min, a significant decrease in the number of particles was noted in the region between the electrodes (Figure 3.7(c)) very similar to that predicted in Figure 3.8(c) and the particles were found to form thin layers on the edges of the both electrodes (Figures 3.7(c)-3.7(d)). Moreover, although a substantial change in the particle distribution was observed to have occurred within the first minute (Figures 3.7(a)-3.7(b)), this change was less pronounced between the second and fourth minutes (Figures 3.7(c)-3.7(d)) with some particles still remaining between the electrodes. The computed time variations of the particle distribution depicted in Figures 3.8(a)-(d) also predict this trend. However, as seen in Figures 3.8 (c) and (d), the decrease in the computed number of particles remaining between the electrodes is greater than that observed during the same time in Figures 3.7 (c) and (d). In fact, the simulations predict that the particles shown in Figure 3.8(a) will collapse eventually into two lines on the top view and on two points in the cross-sectional view corresponding to the electrode edges, $x = 0.8\text{mm}$ and $x = 2.8\text{mm}$ (Figure 3.8(e)), since the model, Equations (3.1)-(3.3), treats the particles as points.

The computed field-induced evolution of the particle distribution in the channel cross-section is depicted in Figures 3.8(a)-(e). It is seen that the particles which were initially located near the electrodes move faster than the others thereby creating regions of clear fluid in the channel cross-section. The trajectories of six selected particles presented in Figure 3.9 show that, at very early times, a particle located in a region of low

field gradient moves slowly at first, and then rapidly accelerates as it approaches one of the electrodes. The circular orbits appeared on the trajectories (Figure 3.9) when the duration of the particle motion is longer than the period of chamber rotation.

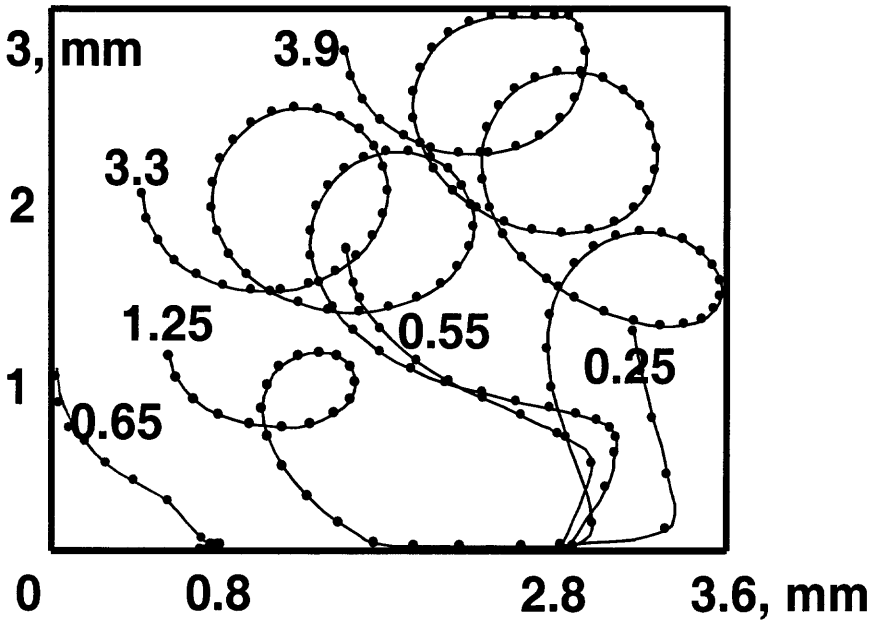

Figure 3.9 The trajectories of six selected particles under the same conditions as those for Figure 3.8; $G = 1.9$, $\Omega\tau_d = 7.75$. The consecutive particle positions are depicted at equal time steps. The number given for every trajectory is the time, t/τ_d, required for a particle to reach the electrodes. Grounded and energized electrodes are on the left and on the right, respectively.

The rotation of the channel affects the particle motions and creates a difference between the amounts of the particles that have aggregated on the two edges of the same electrode. This effect is most pronounced at the high-voltage electrodes and at later times where, as seen in a typical photo in Figure 3.10, more particles were collected on that edge which lies in the direction of the channel rotation from the center of an electrode

than on the other. Computer simulations also predict this trend. Shown in Figure 3.10 is this ratio as a function of $\Omega\tau_d/2\pi$ which was computed for the range of voltages and frequencies of electric fields applied in these experiments. In particular, this ratio equals 1.25 for the conditions of the experiments presented in Figure 3.7 whereas the maximum value, 1.52, corresponds to a field with $V_{rms} = 1$ kV, 1 kHz. Notice that the ratio between the gravitational and dielectrophoretic forces, G, also varies along the curve plotted in Figure 3.10 since $2\pi G/\Omega\tau_d = 1.57$ was fixed in these experiments.

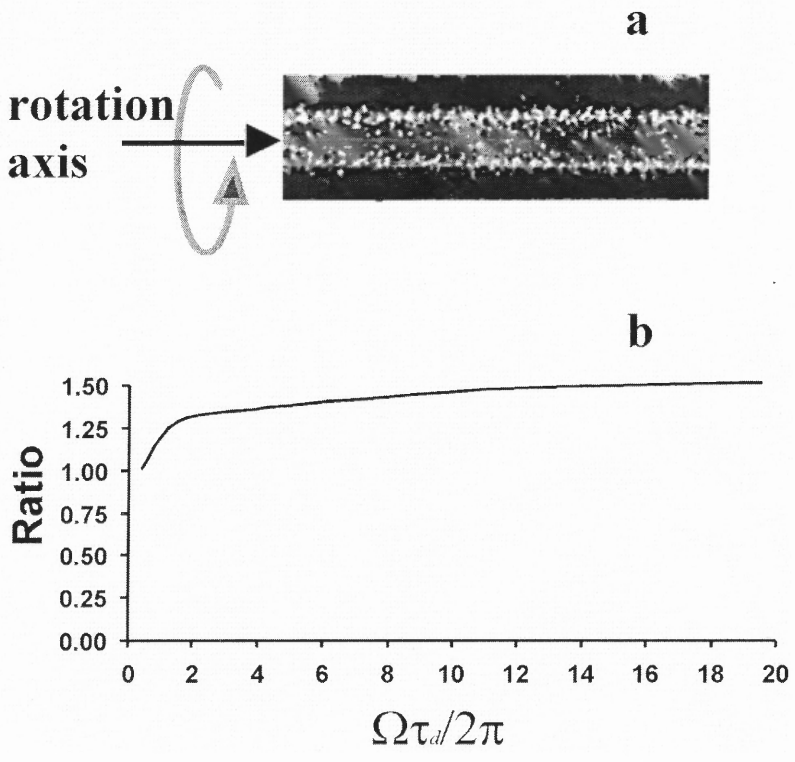

Figure 3.10 The computer simulations of the ratio between number of the particles arriving at different edges of a high-voltage electrode vs. $\Omega\tau_d/2\pi$ for the range of voltages and frequencies of electric fields applied in experiments. The photo illustrates the layers formed on the edges of a high-voltage electrode at V_{rms} =1kV and 100 Hz, correspondingly at $\Omega\tau_d/2\pi$=11.04 and G=17.36.

To characterize the kinetics of the field-induced particle accumulation on the electrodes, the average value of the GL in the vicinity of the edges of the high-voltage and grounded electrodes as a function of time following the application of a field was measured. This value of the GL represents the average thickness of the layer formed by the particles (Figures 3.7(a)-(d)) (see chapter 3.2 for details). To diminish the effects of rotation, the values of GL for both edges of the same electrode were combined. The relative changes of GL were then computed as

$$I_{HV}(t) = \frac{GL_{HV}(t) - GL_{HV,0}}{[GL_{HV}(\infty) - GL_{HV,0}] + [GL_{GR}(\infty) - GL_{GR,0}]} \qquad (3.9')$$

$$I_{GR}(t) = \frac{GL_{GR}(t) - GL_{GR,0}}{[GL_{HV}(\infty) - GL_{HV,0}] + [GL_{GR}(\infty) - GL_{GR,0}]} \qquad (3.9'')$$

where the subscripts "HV" and "GR" denote the high-voltage and grounded electrodes, respectively, $GL_{HV,0}$ and $GL_{GR,0}$ were the values before the electric field was applied and $GL_{HV}(\infty)$ and $GL_{GR}(\infty)$ were the maximum values attained at the end of aggregation. Making use of the characteristic time of dielectrophoresis, Equation (3.9), allows to combine the data on $I_{HV}(t)$ and $I_{GR}(t)$ for different voltages and frequencies of the applied field into two bands in Figures 3.11(a)-(b). For comparison, the computed time variations of the fraction of the particles which reached the edges of the high-voltage and grounded electrodes for electric fields with 100 Hz, $V_{rms} = 1$ kV and 5 kV and $V_{rms} = 3$ kV, 100 Hz and 1 kHz are also plotted in Figure 3.11. As can be seen from Figures 3.11(a)-(b), the predicted rate of the particle accumulation is consistent with the experimental data. The difference at later times is most likely caused by the gradual

saturation of GL due to the formation of multi-layered structures on the electrode edges. The morphology of the aggregation pattern will be discussed in chapter 3.4C.

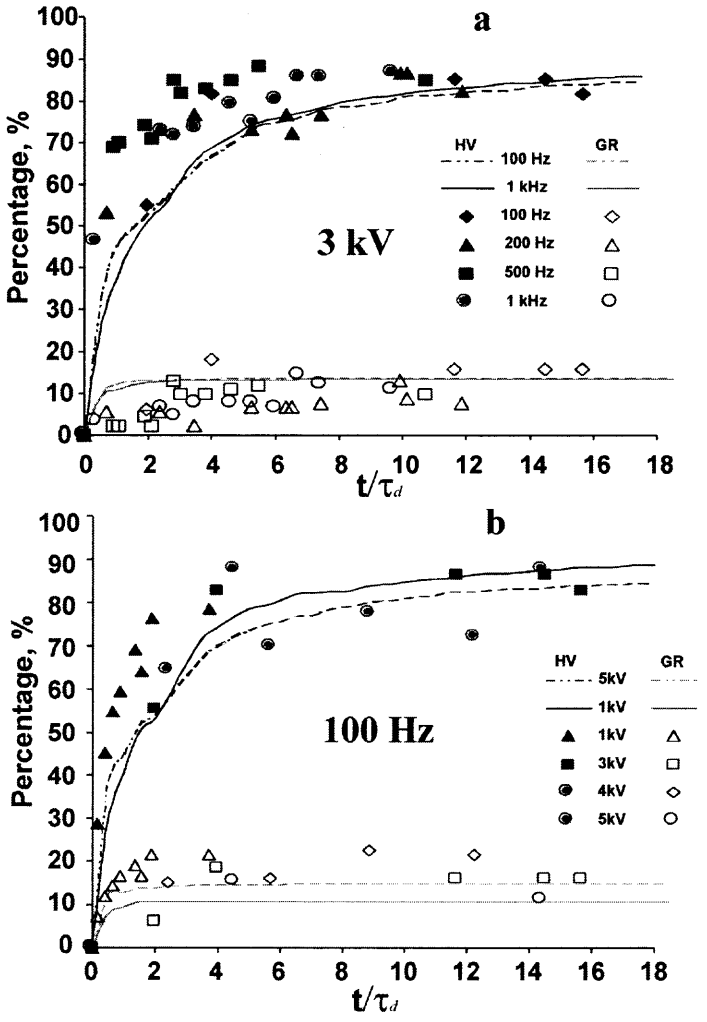

Figure 3.11 The experimental data (filled and empty symbols) and computational results (solid and dashed lines) on the kinetics of the particle aggregation on the electrodes for (a) different frequencies and (b) voltages of the applied field. The experimental data on the time variation of I_{HV}, I_{GR}, and simulation results for a fraction of segregated particles are plotted against a non-dimensional time, t/τ_d, with τ_d given by Equation (3.5). Filled symbols and empty symbols correspond to the high-voltage, HV, and ground, GR, electrodes, respectively. The dashed and solid lines represent computed data for (a) 3 kV, 100Hz ($\tau_d = 18.4$s, $G = 1.9$, $\Omega\tau_d = 7.75$) and 3kV, 1kHz ($\tau_d = 32.5$s, $G = 3.4$, $\Omega\tau_d = 13.5$), and (b) 5kV, 100Hz ($\tau_d = 6.6$s, $G = 0.69$, $\Omega\tau_d = 2.78$) and 1kV, 100Hz ($\tau_d = 165$s, $G = 17.36$, $\Omega\tau_d = 69.39$), respectively.

B. Suspension flow through the rotating channel

The rotating channel (Figure 3.1) was initially filled with a 10^{-3}(v/v)-suspension. Then, following the application of an electric field at the moment when the plane with the electrodes was horizontal, the suspension was cycled through the channel which was rotating clockwise at 4 rpm, until all the suspended particles were captured on the electrodes. The flow rate was taken as 20 ml/min giving for the average fluid residence time $T = 59.4$ s and for the shear rate at the wall $\dot{\gamma}_w = 3.7\ s^{-1}$. The electric fields with $V_{rms} = 3$ kV, 100 Hz and $V_{rms} = 1$ kV, 100 Hz, which were used in most flowing experiments, gave a ratio of dielectrophoresis to residence times, τ_d/T, equal to 0.31 for the former and 2.78 for the latter. For these fields, the values of the Mason number (Zukoski et al., 1993; Hasley et al., 1992)

$$Ma = \frac{8\eta_f \dot{\gamma}_w}{\varepsilon_0 \varepsilon_f E^2 \Psi_\omega} \quad \text{with} \quad E = \frac{V_{rms}}{d},$$

which characterizes the ratio between the viscous force acting on a particle and the interparticle dipolar interaction, were $Ma = 0.09$ for 3 kV and $Ma = 0.82$ for 1 kV, respectively.

The photo presented in Figure 3.12 illustrates the final thickness of the layer formed by the particles aggregated on the high-voltage electrode near the channel inlet. While the plots refer to the measured longitudinal variation of the GL of this layer in the entrance region. As seen in Figure 3.12, the GL decreases away from the channel inlet and then, after about 7 mm, appears to fluctuate around a constant value equal to the average over a more distant part of the electrode. Also depicted in this figure is the longitudinal variation of the number of the particles captured on a high-voltage electrode

predicted by the single-particle model, Equations (3.1)-(3.3). In line with the image analysis procedure, the sliding averaging of the theoretical data along the channel was performed using a length of 1 mm which is not large enough to suppress the fluctuations. On the other hand, the use of a significantly larger averaging interval would have rendered the GL essentially constant through the entrance region.

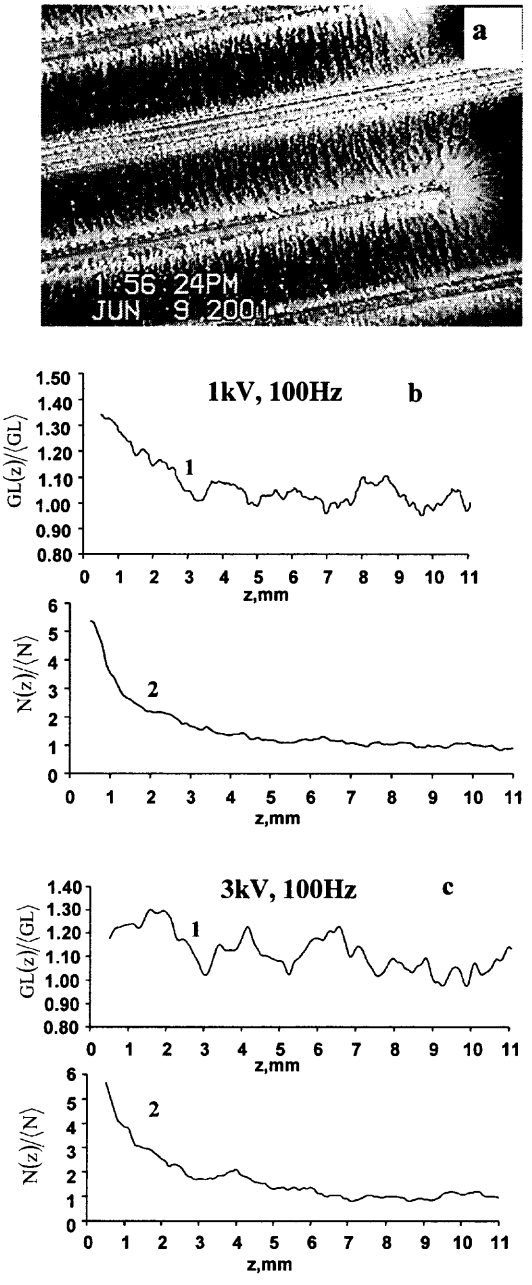

Figure 3.12 The experimental and computed data on the distribution of the particles accumulated on a high-voltage electrode along the entrance region in a flowing 10^{-3} (v/v)-suspension exposed to an electric field with (a) $V_{rms} = 1$ kV, 100 Hz at t= 1997s and (b) $V_{rms} = 3$ kV, 100 Hz at t= 634s flow rate 20 ml/min, rotational speed 4 rpm. Photos show the structures formed near the channel inlet. 1, $GL(z)/\langle GL\rangle$, is the relative value of the GL, 2 is a computed fraction of the particles, $N(z)/\langle N\rangle$, segregated at a distance z. $\langle GL\rangle$ and $\langle N\rangle$ are the values averaged after 7 mm from the inlet.

Shown in Figure 3.13 is the time variation of the GL for a high-voltage electrode in the middle of the channel following the application of the electric field:

$$J_{HV}(t) = \frac{GL_{HV}(t) - GL_{HV,0}}{[GL_{HV}(\infty) - GL_{HV,0}]}, \tag{3.10}$$

where $GL_{HV,0}$ and $GL_{HV}(\infty)$ are the GL values before the electric field was applied and the maximum values attained at the end of the aggregation, respectively. The data on $J_{HV}(t)$ and the simulation results are presented in Figure 3.13 for different voltages using Equation (3.5) for the characteristic time of dielectrophoresis. In Figures 3.12 and 3.13, the values of the GL for both edges of the same electrode have been combined since the total amount of the segregated particles is less sensitive to the rotation effect shown in Figure 3.10.

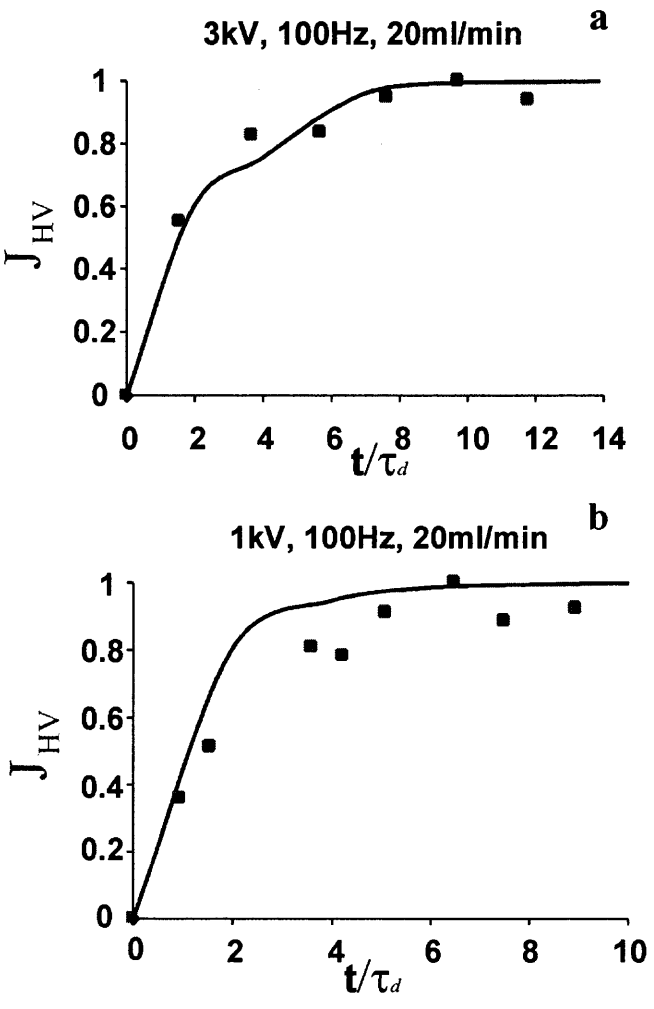

Figure 3.13 The experimental and computed data on the kinetics of the particle aggregation on a high-voltage electrode in the middle of the channel for a flowing 10^{-3} (v/v)-suspension following the application of an electric field with (a) $V_{rms} = 3$ kV, 100 Hz ($G = 1.9$, $\Omega\tau_d = 7.75$) and (b) $V_{rms} = 1$ kV, 100 Hz ($G = 17.36$, $\Omega\tau_d = 69.36$); flow rate 20 ml/min, rotational speed 4 rpm. The experimental data on a fraction of segregated particles, J_{HV}, and computed results are plotted against a non-dimensional time, t/τ_d, with τ_d given by Equation (3.5).

Now consider the predictions of the single-particle model. Simulations showed that the average fluid residence time at $V_{rms} = 3$ kV, 100 Hz was long enough, i.e. $\tau_d/T = 0.31 < 1$, for 54% of the particles to be trapped on the electrodes without leaving the channel, whereas 14.5% of the particles traveled through the channel more than once. In contrast, the average residence time at $V_{rms} = 1$ kV, 100 Hz was short, i.e. $\tau_d/T = 2.78 > 1$, so that only 24% of the particles, initially presented in the channel, would have been captured on the electrodes without leaving the channel, whereas 53.3% of the particles traveled through the channel more than once. As can be seen from Figure 3.13, the computed time variation of the particle accumulation on a high-voltage electrode in the middle of the channel is consistent with the experimental data. Notice that the agreement between the computed and the experimental data for flowing suspensions (Figure 3.13) seems to be better than that without flow (Figure 3.11). This can be attributed to the fact that the contribution of any secondary effect becomes less important when there is flow. A similar trend was observed in experiments conducted on suspensions of negatively polarized neutrally buoyant particles (Dussaud et al., 2000).

Both the experimental and computational data presented in Figure 3.12 show that the amount of particles captured on the electrodes decreases away from the inlet and then, at a distance greater than about seven millimeters, stay more or less constant. Simulations predict, however, significantly larger variations of the number of the particles captured in this region than those observed. This can be attributed to the deficiency of the theoretical model, Equations (3.1)-(3.3), as well as to the uncertainty in measuring the amount of the segregated particles.

C. Aggregation patterns on the electrode edges

Photos presented in Figures 3.7 and 3.14 illustrate the evolution of the aggregation patterns formed by the particles on the high-voltage and grounded electrodes following the application of an electric field to a rotating 10^{-3} (v/v)-suspension. As can be seen, the particles which have accumulated near the electrodes are observed to cluster together on the edges. This field-induced pattern (Figures 3.7 and 3.14) is drastically different from the random build-up of a layer in the course of gravitational settling in the same and as well as more concentrated suspensions following the cessation of the channel rotation (Figure 3.4). On the other hand, the forces acting on a single particle in these experiments (the dielectrophoretic for the former and the gravitational for the latter) were nearly the same, in particular, the dielectric-to-gravity force ratio, G (see Equation (3.6)), was 1.9 for Figure 3.7 and 4.3 for Figure 3.14. This clearly shows that the interparticle interactions, even for initially very dilute suspensions, appear to govern the particle motions near the electrodes. Of course, a theoretical analysis of the pattern formation is well beyond the scope of the single-particle model, Equations (3.1) - (3.3).

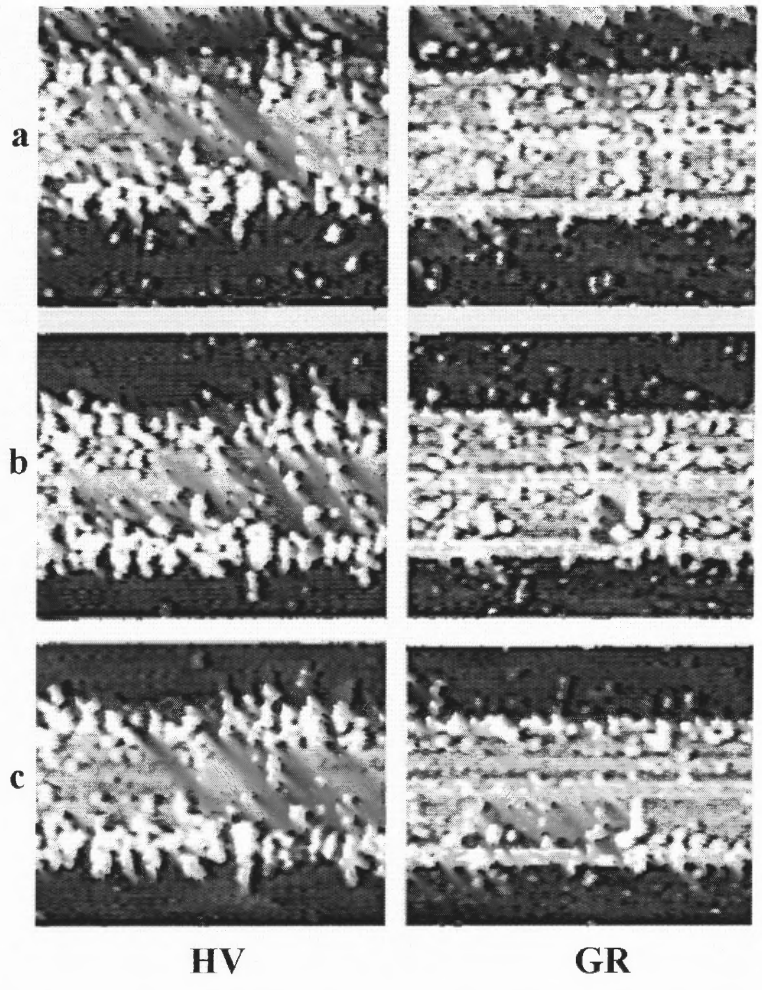

Figure 3.14 The structures formed on the high-voltage (HV) and grounded (GR) electrodes in a 10^{-3} (v/v) suspension following the application of a field with $V_{rms} = 2$ kV, 100 Hz at t= (a) 24s, (b) 50s, (c) 98s, (d) 173s, (e) 312s, and (f) 631s, rotational speed 4 rpm. Under these conditions: $G = 4.3$, $\Omega\tau_d = 17.4$, t/τ_d = (a) 0.51, (b) 1.05, (c) 2.06, (d) 3.62, (e) 6.56, and (f) 13.28. The electrode width is 1.6 mm.

Experiments with different voltages and frequencies of the applied field enabled to suggest a mechanism for the pattern formation on the electrode edges. This mechanism appeared to be similar for both the high-voltage and grounded electrodes, even though the amount of particles accumulated on the former was significantly greater (Figure 3.11). In particular, a set of typical photos in Figure 3.14 depicts consecutive images at the same

location on the electrodes in order to illustrate the kinetics of the particle clustering following the application of a field with $V_{rms} = 2$ kV, 100 Hz. When Figures 3.14(a) - (b) are compared with Figures 3.14(b) - (c), it is apparent that most of the clusters seen in these photos were formed at $t \leq \tau_d$, whereas only few new clusters were formed later, at $t \geq \tau_d$. A similar trend can be observed in the photos of Figure 3.7. On the other hand, the kinetics of the particle accumulation on the electrodes plotted in Figure 3.11 shows that only roughly 50% of the total number of particles have reached the electrode edges at $t \leq \tau_d$ after the application of the field. These data combined with the predictions of the single-particle model depicted in Figures 3.8, 3.9, and 3.11 indicate that, during the initial, relatively fast stage, i.e. for $t \leq \tau_d$, particles close to the edges found energetically favorable sites on the electrodes and then formed most of the nuclei for the growing clusters. Subsequently, in the course of the second stage, $t \geq \tau_d$, new particles coming to the electrode from a more distant part of the channel joined the vertices of these clusters mainly in the direction of the field.

Clustering on the electrodes arises from the competition between the interaction of the particles with a high-gradient field near the edge and the long-range dipolar interactions of nearby particles. Specifically, although the dielectrophoretic force always tends to confine the particles near the edges, the dipole-dipole force either pulls neighboring particles together or pushes them away depending on the relative orientation of the line connecting the particle centers and the electric field direction (Landau et al., 1984). As has been studied thoroughly in the case of bulk magnetic colloids and electrorheological fluids subject to a spatially uniform field, the dipolar interparticle interactions lead to the unlimited growth of chain-like structures aligned in the field

direction whereas, in contrast, the growth of clusters in the course of heterogeneous aggregation in an initially dilute suspension is confined to the electrode edges by the presence of a high-gradient field. As a consequence of this confinement, the particles form arrays of bristles along the electrode edges (Figures 3.7 and 3.14) the length of which increased with an increase in the applied voltage. Calculations of an auto-correlation function for the GL variations along the electrodes revealed that the assembly of bristles did not appear to have any long-range order.

The effects of the flow on the pattern formation on the electrodes were found to be similar for both applied fields. In particular, a set of photos presented in Figure 3.15 shows the structures formed in a flowing suspension on the high-voltage and grounded electrodes following the application of a field with $V_{rms} = 1\ \text{kV}$, $100\ \text{Hz}$ in comparison with those formed in a suspension without flow. The photos for a flowing suspension in Figure 3.15 were taken in the middle of the channel in order to eliminate the entrance effects. As can be seen from Figure 3.15, the presence of flow caused the particles to build shorter bristles, finer clusters, and tighter packed layers. These effects are more pronounced for the lower value of the applied voltage, i.e., for the smaller Mason number. This can be attributed to the fact that the exposure of the clusters to shear stress caused loosely connected particles to be released and to travel along the electrodes thereby covering the edges more uniformly.

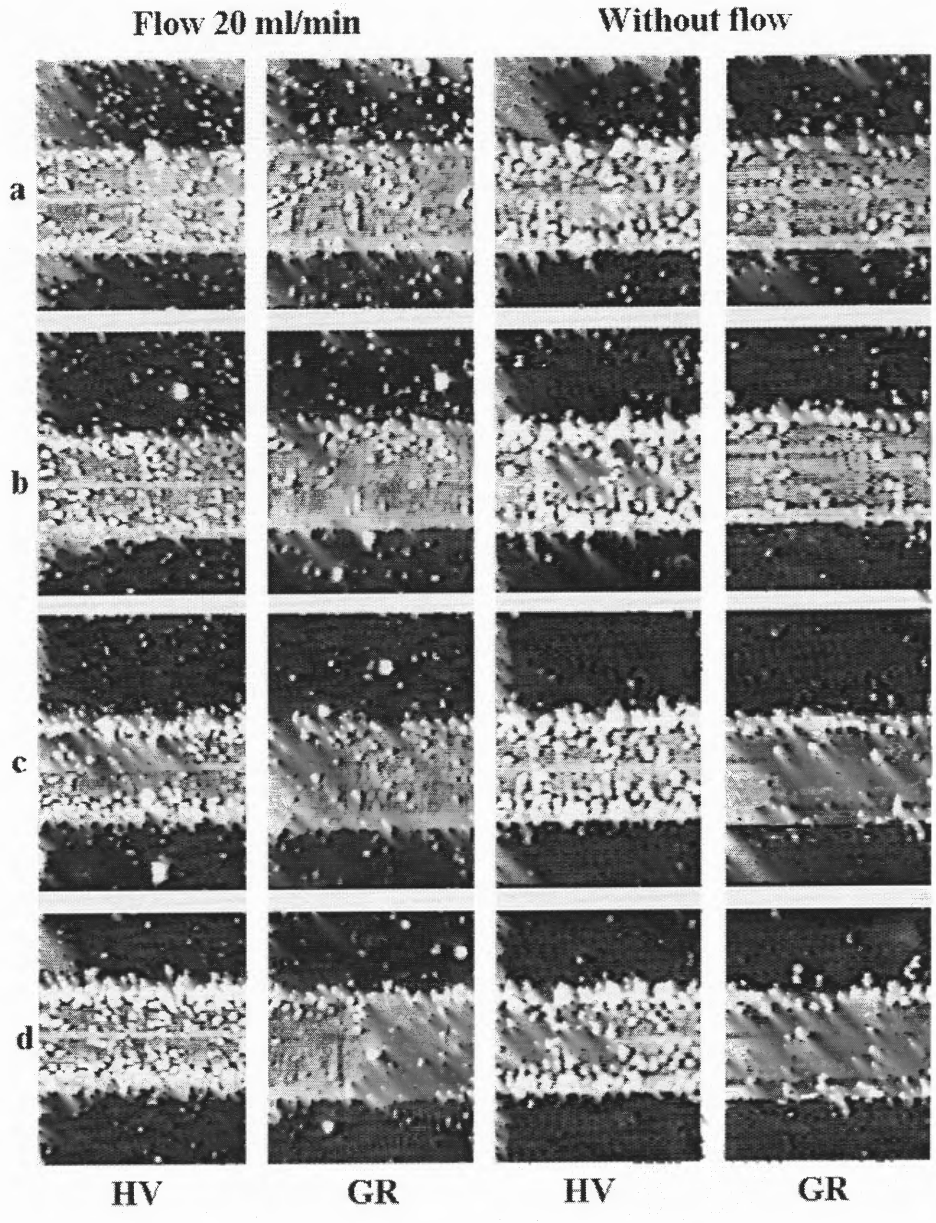

Figure 3.15 The structures formed on the high-voltage (HV) and grounded (GR) electrodes in a 10^{-3} (v/v)-suspension following the application of an electric field with $V_{rms} = 1$ kV, 100 Hz ($\tau_d = 165$ s) without and with flow of 20 ml/min, rotational speed 4 rpm. The electrode width is 1.6 mm. With flow: t = (a) 73 s, (b) 156 s, (c) 257 s, (d) 383 s, (e) 594 s. Without flow: t = (a) 69 s, (b) 149 s, (c) 264 s, (d) 314 s, (e) 617 s.

3.4 Summary and Conclusions

The conditions under which a suspension of positively polarizable particles will undergo a heterogeneous aggregation following the application of a high-gradient strong ac field (~ several kV/mm) were specified and then theoretically the field-induced particle motions and pattern formation in very dilute suspensions under these conditions were examined experimentally. In addition, to prevent the gravitational settling of the particles, a setup in which the electric chamber was kept slowly rotating around a horizontal axis along with a special technique to energize the electrodes was developed, and a single-particle model was used for the simulations of the field-induced particle motions. Also, the real part of the complex value of the particle polarization, which is required for the calculation of the dielectrophoretic force, was measured in a spatially uniform low-strength field (~ V/mm).

The predictions of the single-particle model for the kinetics of the particle accumulation on the electrodes were found to be in a reasonable agreement with experimental data. This demonstrates that the value of the particle polarization measured in low fields can be used for describing the particle motions in strong fields. However, even in an initially very dilute suspension, interparticle interactions were found to govern the formation of arrays of bristles along the electrode edges. The experiments suggested the existence of a two-step mechanism for the formation of the arrays of bristles along the electrode edges, which arose from the interplay of the dielectrophoretic force that confined the particles near the electrode edge and the dipolar interactions of nearby particles.

The slow rotating electric chamber which has been developed makes feasible electro-hydrodynamic experiments on suspensions with particles heavier than the suspending fluid. This significantly extends the choice of suspension constituents which can be used in the experiments because it allows for a much broader variation of the polarization mismatch between the particles and the suspending fluid than is possible if only suspensions containing neutrally buoyant particles are used. The results of these studies provide the basic characteristics of the field-induced particle segregation needed for the design and optimization of electro-hydrodynamic apparatuses.

CHAPTER 4

MANIPULATION OF MICRO - PARTICLES IN MICROFLUIDIC DIELECTROPHORETIC DEVICES

4.1 Introduction

Among a variety of available methods for the manipulation of minute particles in a liquid, dielectrophoresis which employs ac fields is currently becoming one of the major techniques in micro-devices because the application of an ac field suppresses undesirable electrolytic effects and electro-convection in the liquid and employs polarization forces that are insensitive to the particle charge which is difficult to control (Zimmermann, 1996, Koch et al., 2000). Also, positioning particles in pre-selected locations for subsequent analysis is the first step in the operation of micro-analytical systems.

The heart of a dielectrophoretic device is a channel equipped with an array of electrodes to generate a spatially non-uniform ac field that drives particles to the regions of high field strength (*positive* dielectrophoresis) or low field strength (*negative* dielectrophoresis), depending on whether they are more or less polarizable than the suspending fluid (Jones, 1995). Dielectrophoretic phenomena can be easily manipulated by varying not only the strength but also the frequency of an applied field (Jones, 1995). The rapid progress in micro-fabrication technologies through the application of the facilities, methods, and materials of semiconductor industry makes it feasible to fabricate micro-devices in which the application of the voltage of the order of only tens of volts enables one to generate high-gradient strong electric fields (~several kV/mm) over a broad range of frequencies from several Hz to several MHz (Koch et al., 2000). For

comparison, the application of several ac kilovolts is required for millimeter-scale electrodes used in macro-devices to generate the same field. The widespread use of dielectrophoretic micro-devices for pressure driven flows emphasizes the need to study the field-induced particle motions and aggregation in order to facilitate the design, optimization, and operation of such devices.

The field-driven structure formation in a flowing suspension subjected to a high-gradient ac field is governed by the interplay of the dielectrophoretic force and the interparticle electric interactions. Under certain conditions (referred to as *particle heterogeneous aggregation* (Section 1.4)), the coupling of these forces will enable one to concentrate flowing particles in certain areas of an electric chamber where they would then aggregate. This regime is advantageous for positioning particles in pre-selected locations for subsequent analysis in micro-analytical systems. The field-induced particle distribution to be formed along the channel depends on the ratio of the characteristic time of dielectrophoresis, which is a measure of time required for a particle to move across the channel under the action of dielectrophoretic force, to the time that a particle spends inside a channel (the so-called resident time). Increasing the resident time provides more time for electric forces to collect particles at the same location. In this chapter the experimental and theoretical consideration of the kinetics of the heterogeneous aggregation of positively polarized particles in dielectrophoretic microfluidics is given, and the limitations on the scale of an electrode array for trapping particles in microfluidics by positive dielectrophoresis are addressed.

4.2 Field-Induced Heterogeneous Aggregation of Micron Particles

Two types of electrical forces govern the suspension behavior under the action of a spatially nonuniform ac field (Jones, 1995). One of them is the dielectrophoretic force $\mathbf{F}_{dep}$ generated through the interaction of a particle with a spatially non-uniform ac field. In particular, for a sphere (Jones, 1995) it is described by Equation (1.19) (Chapter 1). $\mathbf{F}_{dep}$ moves the particle either towards or away from the high field strength regions. The other force is the long-range interparticle electric interaction generated by the polarization of the particles in an applied field (Halsey, 1992). The main effect of the interparticle interactions is that they, if sufficiently strong, cause a suspension to undergo separation into low- and high-concentrated phases by rearranging the randomly distributed particles into a variety of ordered aggregation patterns (the so-called *electro-rheological effect*) (Halsey, 1992). A thermodynamic theory (Khusid and Acrivos, 1995, Khusid and Acrivos, 1999) for the field-driven phase separation predicts a set of phase diagrams which specify the state of a suspension depending on the volume fraction of the particles, φ, and the relative strength of an applied field $\lambda = \varepsilon_0 \varepsilon_f E^2 v_p / k_B T$ where $k_B T$ is the thermal energy. The concentration dependence of the critical field strength, above which the suspension should undergo the phase separation following the application of a spatially uniform ac field, is given by the spinodal on the phase diagram (Figure 1.9, Chapter 1). An asymptotic expression for the spinodal at low particle concentrations is (Khusid and Acrivos, 1996)

$$\varphi \lambda \Psi_\omega \approx 1, \tag{4.1}$$

where the function Ψ_ω presents the dependence of the electric energy of the interparticle interactions on the field frequency, the electric properties of the particle and the

suspending fluid; a rough estimate yields $\Psi_\omega \sim 3\mathrm{Re}(\beta)^2$. When a suspension is exposed to a spatially nonuniform field so strong that the left-hand side of Equation (4.1) is larger than unity, the dielectrophoresis would be accompanied by the phase separation (Khusid and Acrivos, 1996). Then the suspension behavior will depend on the ratio of two time scales, τ_a and τ_d (Qiu et al., 2002). The former refers to the characteristic time for the field-induced structure formation in a suspension subjected to a spatially uniform field (Equation (1.21), Chapter 1), whereas the latter is a measure of the time required for a particle to travel over a characteristic length of the system, d, under the action of the dielectrophoretic force, Equation (3.5) (Chapter 3). Only when

$$\frac{\tau_d}{\tau_a} \approx \frac{3d^2|\mathrm{Re}(\beta^*)|}{a^2\xi(\varphi)} << 1 \qquad \text{with } \xi \approx 0.4\left|(\pi/6\varphi)^{5/3} - 1\right|, \tag{4.2}$$

the particles are forced to accumulate in certain areas of the micro-device and then to aggregate, a regime referred to as the particle heterogeneous aggregation (Section 1.4).

A single-particle model (Section 3.2) considers the dielectrophoretic force, Equation (1.19), the Stokes drag force, and the gravitational force exerted on a particle and ignores all interparticle interactions. The field-induced displacement $\mathbf{r}(t)$ of a particle being initially at $\mathbf{r}_0$ is obtained by solving the Equation (3.2) (Chapter 3). It is applicable for a domain where the strength of an applied field is smaller than the critical field strength given by Equation (4.1) and for a domain of a larger field strength when the characteristics of the channel meet the requirements given by Equation (4.2). The main non-dimensional parameters of the single-particle model, Equation (3.1) (Chapter 3), are the ratio τ_d/T of the characteristic dielectrophoresis time to the average fluid residence time, $T = L/U_a$, where L is the channel length and $U_a = Q/A$ is the average fluid

velocity with Q and A being the volumetric flow rate and the area of the channel cross section, respectively, the channel length to the electrode width ratio, L/d, and the ratio of the gravitational and dielectrophoretic forces Equation (3.6) (Chapter 3).

The major difference between operational ranges of millimeter-scale and micrometer-scale dielectrophoretic devices lies in the fact that τ_d/T is of the order of several tenths for the former and $\tau_d/T \sim 0.001-0.01$ for the latter.

4.3 Microfabrication and Experimental Procedures

4.3.1 Microfabrication Techniques

Due to the small volume in dielectrophoretic micro-devices, they operate at a flow rate from several tens of nl/min to several μl/min. A technique for the batch fabrication of an apparatus featuring 150 micro-devices placed on a 4-inch silicon wafer is presented. The choice of materials renders these micro-devices mechanically robust and chemically inert. The presented approach radically simplifies the manufacturing of dielectrophoretic devices and their integration into a higher-level system. In particular, several apparatuses of this type can easily be combined to form a unit for matching a flow rate of the order of several ml/min, typical of many applications, by distributing the main stream among a sufficiently large number of micro-devices operating in parallel. The use of a multi-channel apparatus also enables one to conduct at once experiments on the same fluid with different configurations of microelectrodes, thereby significantly reducing the labor in the optimization of a dielectrophoretic device for particular applications. Micro-devices with well-defined configurations of the electric field and the flow pattern where a flowing

suspension is exposed to a strong field such that the electric field lines are arranged in the channel cross section perpendicular to the streamlines of the main flow were designed. With this in mind, channels with electrodes arranged parallel and perpendicular to the flow (Figure 4.1) in order to cover the limiting cases of the array orientation with respect to flow were fabricated.

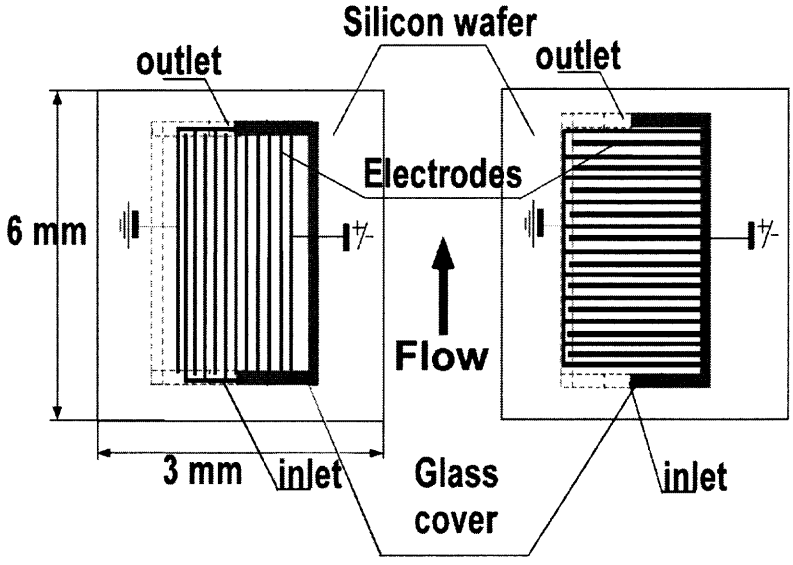

Figure 4.1 Microfluidics with electrodes arranged parallel and perpendicular to the flow.

For each configuration, three different devices having equal electrode width and inter-electrode spacing of 2μm, 5μm, and 10μm, respectively, were constructed. The fabrication process is illustrated in Figure 4.2.

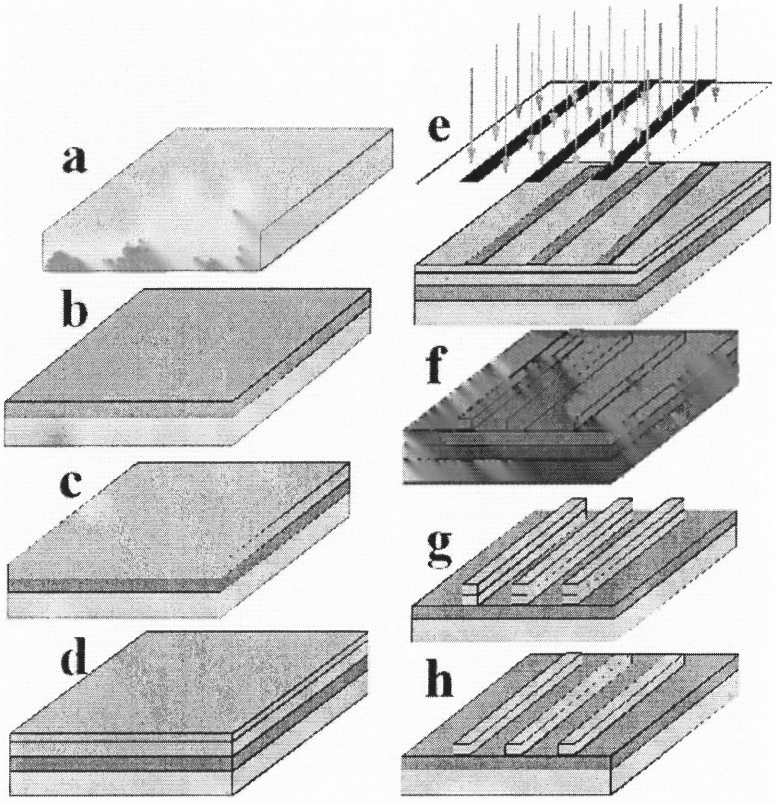

Figure 4.2 Steps in the micro-electrode fabrication process:
(a) Cleaning of the silicon wafer
(b) Deposition of the oxide layer
(c) Deposition of the aluminum layer
(d) Coating with photoresist
(e) UV exposure
(f) Develop
(g) Aluminum etching
(h) Photoresist strip

In the first step, a 4"-silicon wafer was chemically cleaned to remove particulate matter on the surface as well as any traces of organic, ionic, and metallic impurities (Figure 4.2a). After cleaning, silicon dioxide, which serves as a barrier layer, was thermally grown on the surface of the wafer using dry oxygen to form a 500-nm thick insulation layer (Figure 4.2b). Dry oxide provides a dielectric strength (>10^5 V/mm) greater than

wet or deposited oxide. This field strength is more than ten times higher than the electric field used in experiments presented in this chapter. During the next step, a 200-nm aluminum layer was sputtered on the top of the SiO_2 layer (Figure 4.2c). Standard photolithographic techniques were used for the fabrication of microelectrodes. The wafer was coated with positive photoresist (Figure 4.2d), and then the desired pattern was transferred to photoresist by exposure to UV radiation through a patterned chrome-on-quartz mask(Figure 4.2e). The exposed photoresist was then washed away by the developer solution (Figure 4.2f). Aluminum was etched from the unexposed regions using wet etching in an aluminum etch bath (Figure 4.2g), and finally the remaining photoresist was stripped by cleaning the wafer in an m-pyrol bath (Figure 4.2h). The patterned mask was designed in such a way that aluminum was left in the regions surrounding each microelectrode array (Figure 4.3a) to facilitate anodic bonding.

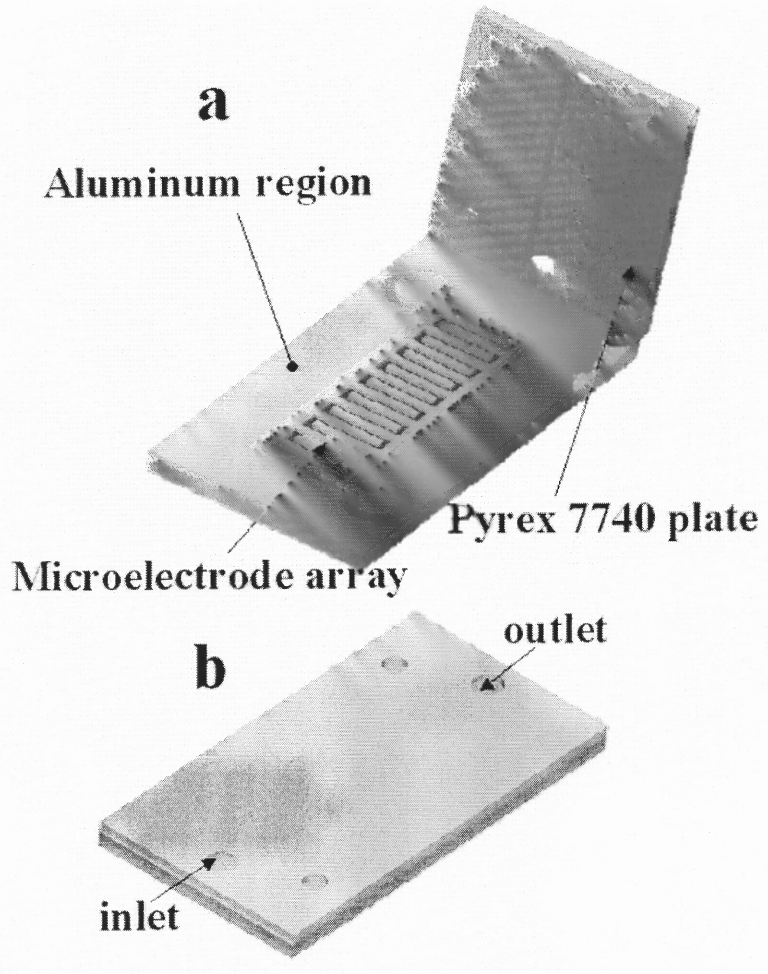

Figure 4.3 3D model of (a) open and (d) closed micro-device.

As illustrated in Figure 4.2, the channel, the fluid inlet and outlet ports, and the side holes for energizing the electrode array, were micro-machined into a Pyrex 7740 glass plate (1 mm thick and 100 mm in diameter), using ultrasonic machining at the Bullen Ultrasonics, Inc., OH. 150 channels and through hole sets were designed and located on the plate to individually match microelectrode arrays on the silicon wafer. Each channel is 600μm wide x 30μm deep x 5000μm long. The diameters of the inlet/outlet ports and side holes are 600μm and 300μm, respectively. As shown in Figure 4.1, the corners and edges of the electrode assemblies are covered by glass to minimize undesired electrolytic effects in the suspending fluid.

The multi-channel apparatus (Figure 4.4) was completed by anodic bonding.

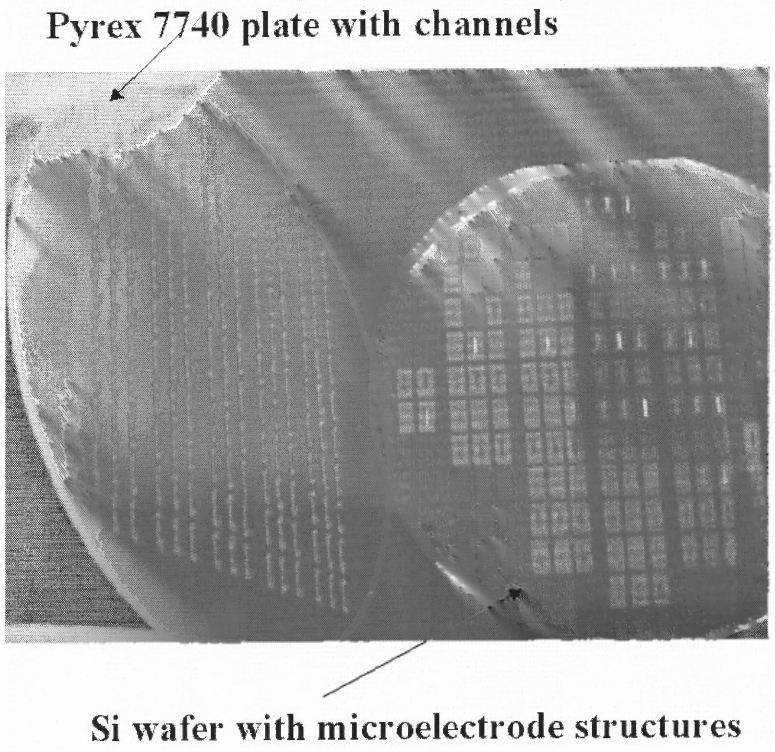

Figure 4.4 Photograph of the wafer containing 150 microelecrode structures and glass cover with microchannels.

First, micro-machined channels in the glass plate were aligned with electrode structures on the silicon wafer using a precision bond aligner, EV 450 (Electronic Visions Inc., AZ). Then, the plate and the wafer were bonded on an EV501 universal wafer bonder (Electronic Visions Inc., AZ). The process was automatically controlled by a program, specifically designed for joining aluminum coated silicon to Pyrex substrates. The assembly was placed in the chamber in which it was heated to 400^0C and then voltage of 500V was applied for 15 minutes, while 100N force was maintained on the structure. The chamber was then cooled to the room temperature. It was found that the combination of these relatively high temperature, voltage and bonding force of 100N, were sufficient to enable good anodic bonding of the aluminum coated silicon wafer with the Pyrex 7740 glass surfaces. It should be noted that no special care was taken to electrically short across the oxide layers on the silicon wafer. In addition, each aluminum region was isolated from the others, and while only a fraction of the field may be used to migrate ions in the Pyrex, strong bonding was obtained. The bonding quality of the assembly was evaluated by visual and qualitative mechanical inspections. The wafers could not be pulled apart, and no channel leakage has been observed. Figure 4.3 illustrates a 3-D schematic of the complete device.

4.3.2 Experimental Setup

The experimental setup is presented in Figure 4.5. Flow through a micro-device was generated and controlled using a syringe pump (PHD 2000 Programmable, Harvard Apparatus, Inc., MA) which injected a suspension via fused silica capillary tubing (Upchurch Scientific, WA). The inlet and outlet of the device were connected to the capillary tubing using microtight tubing sleeves (Upchurch Scientific, WA).

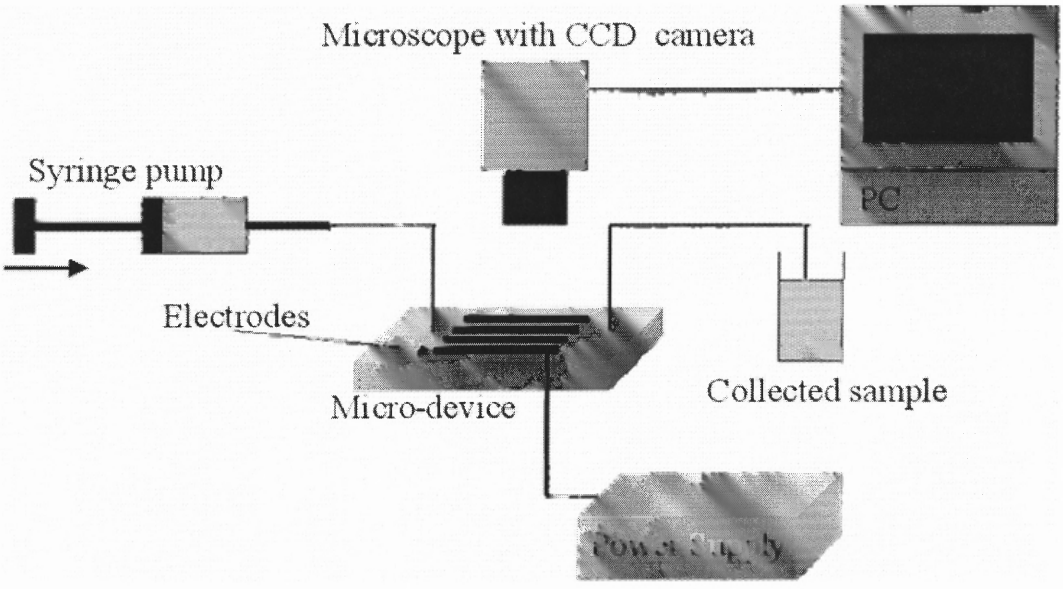

Figure 4.5 Experimental setup

Experiments were performed at 23°C. The suspension was delivered at a constant flow rate into the micro-device and collected from the outlet tubing. To generate a high-gradient ac field (1 kHz for most experiments) inside a channel, electrodes in an array (Figure 4.1) were alternatively energized with a voltage amplifier (Model A800, FLC Electronics AB, Sweden) and grounded, and the silicon wafer was grounded.

The suspension flow in the channel was visualized and recorded using a microscope equipped with an image acquisition unit (DEI-750D, Optronics, CA), which was connected to a computer. On images acquired through the channel top, the Al_2O_3 particles appeared as dark spots whereas aluminum electrodes appeared as white stripes. The changes of the distribution of the gray level (GL) along the channel on black & white images were used to estimate the longitudinal distribution of the particles. The GL of a pixel, defined as the relative local brightness, have a maximum range from 0 (black) to 255 (white). The detailed procedure of using the VISILOG-5 (Noesis, Inc.) image analysis software for measuring GL was described in Section 3.1.

The magnitude of $(GL_0\text{-}GL)$ with GL_0 being the initial value was considered as representing the amount of the particles that had segregated on the electrodes under the action of an electric filed. The longitudinal variation of $(GL_0\text{-}GL)$ along a rectangular box surrounding the whole electrode was measured in order to characterize the non-uniformity of the steady-state particle distribution in the flow direction. For the cases where the electrodes were arranged parallel to the flow, snapshots of 4 successive sections of the micro-channel starting from the inlet area were combined, thereby having the length of a box for the GL measurement of about 1000μm. To reduce the fluctuations in the data, a sliding averaging of the readings was performed over a length of 10μm along the channel axis. For channels with perpendicular arrangement of the electrodes with respect to the flow, the GL variation along the length of the channel was obtained by measuring $(GL_0\text{-}GL)$ on each electrode separately.

Notice substantial limitations of using the magnitude of GL for the estimation of the amount of segregated particles. Specifically, GL measurements do not distinguish

between a single and multiple layers of the segregated particles on the portion of an electrode that is being analyzed.

4.3.3 Suspension Properties

The suspension consists of a fraction of sieved aluminum oxide spherical particles AL-601, 99.9%, AEE, NJ, suspended in Dioctyl Terephthalate, 98%, Aldrich Chemical Co. This suspending fluid was chosen to match the refraction index of the Pyrex glass. The particle density is 3.75 g/cm^3. The density and viscosity of Dioctyl Terephthalate are 0.98 g/cm^3 and 76.0 cp at 23°C, respectively. The particle size distribution on a number basis (Figure 4.6) was measured with a Beckman-Coulter laser diffraction particle size analyzer LS 230. The average radius a of the particles is 1.36μm , and 80% of the particles have radii between 0.59 and 2.12μm (Figure 4.6).

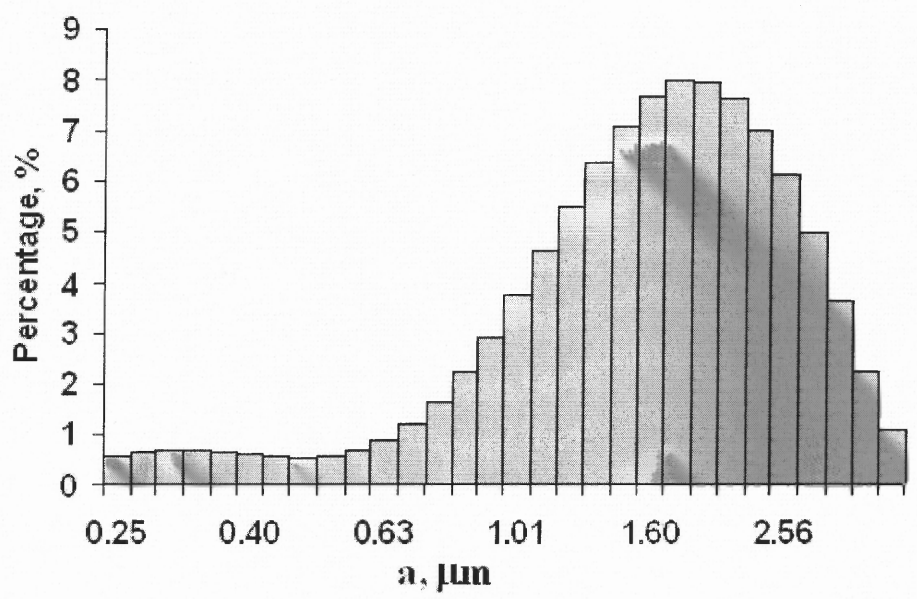

Figure 4.6 The particle size distribution of the suspension, measured in the Beckman Coulter LS230 and then used in the computations .

As was demonstrated in Chapter 3, the field dependence of the particle polarizability, β, appears to be independent of the field strength up to several kV/mm typical of dielectrophoresis applications. Hence, an approach utilizing low-strength fields for measuring β was employed. To this end, the complex dielectric permittivities of the suspending fluid, ε_f^*, and suspensions, ε_s^*, with $\varphi = 1, 5, 10, 15$ (v/v)% were measured in the range of frequencies from 0.1 Hz to 7 MHz on a broadband dielectric spectrometer (BDS-80, Novocontrol, GmBH), utilizing a standard technique of dielectric spectroscopy for low-fields (~4 V/mm). Then, the Maxwell–Wagner expression was employed for a suspension of randomly distributed spherical particles (Dukhin et al., 1974, Russel et al., 1989), $(\varepsilon_s^* - \varepsilon_f^*)/(\varepsilon_s^* + 2\varepsilon_f^*) = \varphi\beta$, to calculate β. For the range of frequencies, 0.1-1 kHz, used in the experiments, $\mathrm{Re}(\beta) = 0.35$, and the dielectric constant of Dioctyl Terephthalate, ε_f, is 2.95.

4.4 Experimental Data and Comparison with Simulations

Experiments were conducted on microfluidics of all configurations and electrode widths and spacings shown in Figure 4.1. A micro-device was initially filled with a pure liquid. Then, following the application of a voltage, the suspension was introduced into the channel. The flow rate was taken as 0.02 μl/min giving for the average fluid velocity $U_a = 18.5\mu\mathrm{m/s}$ and for the average fluid residence time $T = 270$ s. For presented experiments, the Reynolds numbers for the fluid flow and for the relative particle motion, defined as $\mathrm{Re}_f = \rho_f U_f H/\eta_f$ and $\mathrm{Re}_p = \rho_f U_p a/\eta_f$, respectively, with $H = 30\mu\mathrm{m}$ being the channel gap and U_p typifying the relative particle velocity, are $\mathrm{Re}_f \sim 10^{-5}$ and

$Re_p \leq 10^{-5}$. The particle displacement caused by Brownian diffusion, $\Delta_D \sim \sqrt{D_{Br} t_{exp}}$, over the characteristic time of experiments $t_{exp} \sim 15\,\text{min}$, with $D_{Br} = k_B T/6\pi\eta_f a$ being the diffusion coefficient of a particle, is $\Delta_D \sim 1.4\mu\text{m}$. The velocity of the gravitational settling of a particle is $v_g = 2(\rho_p - \rho_f)a^2 g/9\eta_f = 0.15\mu\text{m/s}$ giving for the characteristic time required for a particle to settle in the channel $H/v_g = 200\text{s}$. The magnitudes of a 1 kHz voltage applied to the microfluidics with $10-\mu\text{m}$, $5-\mu\text{m}$, and $2-\mu\text{m}$ electrodes were taken 20 V_{rms}, 10 V_{rms}, and 7 V_{rms}, respectively, in order to generate electric fields with similar strengths, V_{rms}/d = 2kV/mm, 2kV/mm, and 3.5kV/mm, but with different gradients of the squared field strength, V_{rms}^2/d^3 = $0.4\cdot10^3\,\text{kV}^2/\text{mm}^3$, $0.8\cdot10^3\,\text{kV}^2/\text{mm}^3$, and $6.1\cdot10^3\,\text{kV}^2/\text{mm}^3$, respectively.

To operate all microfluidics in the regime of the particle heterogeneous aggregation, the experiments were conducted on 0.1(v/v)% suspensions for which the ratio τ_d/τ_a (Eq. (5) with d being the electrode width) varied from $1.7\cdot10^{-4}$ for $2-\mu\text{m}$ channels to $4.2\cdot10^{-3}$ for $10-\mu\text{m}$ channels. Since $Re_f << 1$, the entrance length of the order of the channel gap is required for a flow to reach the fully developed parabolic velocity profile for which the fluid velocity, $\mathbf{v}_f$, has only a z-component along the channel axis, $v_{fz}(y)$, varying along the cross section of the channel in the y direction (Equation (3.3), Chapter 3

The gap between the electrodes was very small with respect to their length, so that the field could be taken as two-dimensional, varying only along the channel cross section perpendicular to the electrodes (Figure 4.7(a)).

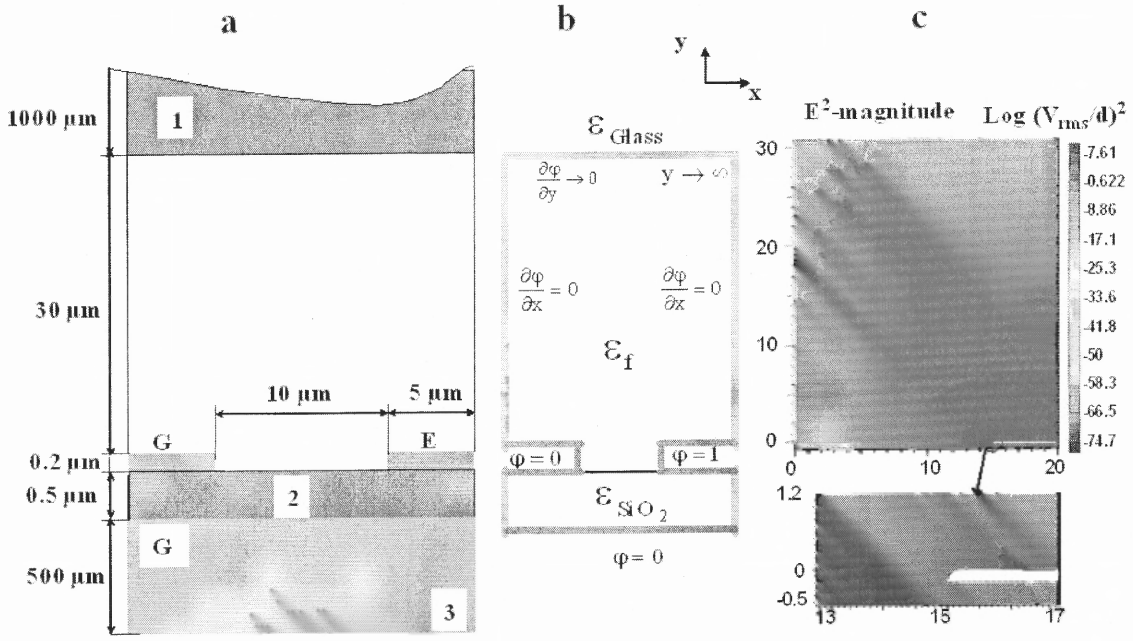

Figure 4.7 (a) Cross-section of the microfluidics which passes through the centers of the grounded (G) and energized (E) electrodes . Pyrex glass cover 1 is on the top, silicon layer 3 is on the bottom, and SiO2 insulating layer 2 is on the top of the Silicon (b) Boundary conditions used in the field calculation, (c) Distribution of the non-dimensionalized square of the magnitude of the electric field in the cross-section of the micro-channel for 10μm electrodes.

Furthermore, because of the symmetry and periodicity of the electrode array, the electric field was computed only for a rectangular box which is bounded by two insulating vertical boundaries (by symmetry) passing through the centers of the neighboring energized and grounded electrodes and by the grounded bottom boundary with the silicon wafer (Figure 4.7). The dielectric constants of the SiO_2 layer and the glass are $\varepsilon_{SiO_2} = 3.9$ and $\varepsilon_{glass} = 5$. Due to a large thickness, vanishing of the vertical component of the electric field at infinity was taken as the boundary condition for the glass cover (Figure 4.7(b)). Simulations were performed using a finite element code from a library of C++ subroutines DIFFPACK (Langtangen, 1999). The distribution of the field strength in a channel with $10-\mu m$ electrodes is depicted in Figure 4.7(c). Notice the appearance of two regions of the highest field strength, a large one near the energized electrode and a small one near the edge of the grounded electrode, and a large region of its lowest strength above the center of the grounded electrode. Hence, the application of an electric field to the flowing suspension should cause the positively polarized particles to segregate mainly on the edges of the energized electrodes. The distributions of the field strength in channels with $5-\mu m$ and $2-\mu m$ electrodes are similar to that presented in Figure 4.7(c), but the field strength decays faster with distance from the electrodes for smaller electrodes. Recall that the solution of Laplace's equation for an array of alternatively energized and grounded electrodes is known to decay exponentially with distance from the array over a characteristic length comparable to the electrode width. For experimental conditions, the dielectrophoretic force, Equation (1.19) (Chapter 1), was smaller than the gravity force in the upper part of the channel cross section but significantly exceeded it close by the electrodes ($\sim d$), giving for G, Equation (3.6)

Chapter 3), values varying from $3 \cdot 10^{-4}$ for $2-\mu m$ electrodes to $5 \cdot 10^{-3}$ for $10-\mu m$ electrodes. Calculated from Equation (4.1) the critical field strength, $0.2 kV/mm$ for a 0.1(v/v)% suspension, was smaller than the field strength in a region near the electrodes ($\sim d$) so that the particles were forced to aggregate there.

To simulate the field-induced particle segregation following the application of an electric field at t=0, solved Equations (3.1), (3.2), and (3.6) were solved for each of N non-interacting particles. The magnitudes of the particle radii were randomly assigned based on the particle size distribution (Section 4.3.3). The model calculations required no fitting parameters because the particle polarizability measured in a low-strength field was used (Section 4.3.3). The micro-devices (Figure 4.1) were designed so that the dielectrophoretic and gravity forces in Equation (3.1) were directed normal to the channel axis. In this case, the relative particle velocity, $\mathbf{u}-\mathbf{v}_f$, has two components in the xy plane for channels having electrodes parallel to the flow (Figure 4.1) and only one component in the y direction for channels having electrodes perpendicular to the flow (Figure 4.1). In line with experiments, it was considered that there were no particles in the channel at t=0. For channels having electrodes arranged parallel to the flow, the particle motions were computed for a rectangular box bounded by two planes passing parallel to the yz plane along the center lines of two neighboring grounded electrodes. A particle leaving the box through one of its longitudinal sides was replaced by another particle that simultaneously entered the box through the other side at a mirror point. For channels having electrodes arranged perpendicular to the flow, the particle motions were computed only for the yz cross section of the channel. Particles located on the top and the bottom of the channel were not allowed to exit the channel, so that their outward

vertical velocity components were ignored. Once a particle came to the electrode edges it was considered to be trapped and its further displacement was not computed. Particles entered the box through the inlet cross section, $z = 0$, at a point with randomly taken y and x coordinates. The entrance time was randomly assigned to each particle from the interval $0 \le t \le t_{exp}$. The numerical procedure used to solve Equations (3.1) and (3.2), which requires the calculation of ∇E_{rms}^2 at any point, was described in (Dussaud et al., 2000). Simulations were performed using a finite element code from a library of C++ subroutines DIFFPACK (Langtangen, 1999). A typical simulation included N = 1000 particles for channels having the electrodes parallel the flow and 2000 particles for channels having the electrodes perpendicular to the flow These numbers are close to the full amount of suspended particles, $\sim \varphi H w U_a t_{exp} / v_p$, that in actual experiments entered a micro-channel through the inlet cross section having the width w equal to that of the computational box used for simulations.

The photos in Figure 4.8 (a) – (d) illustrate the kinetics of the particle segregation along a part of the channel with energized $10-\mu m$ electrodes following the application of an electric field, $20\ V_{rms}$, 1kHz, to a flowing suspension for parallel and perpendicular electrode configuration.

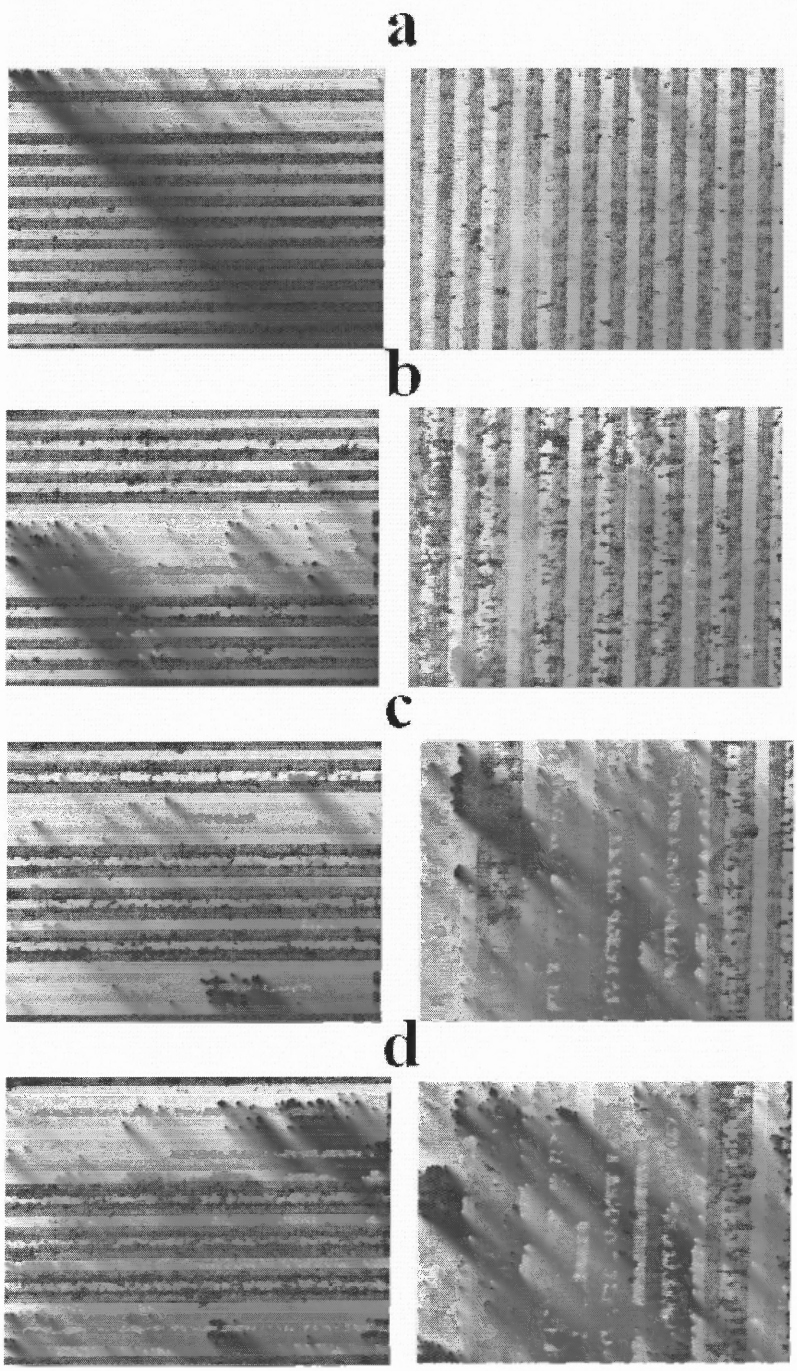

Figure 4.8 Segregation of the particles (*dark*) in a 0.1 (v/v) % suspension along the channel with $10-\mu m$ parallel (left) and perpendicular (right) electrodes (*white*) versus flow direction (from left to right) configuration, following the application of 20 V_{rms}, 1kHz for (a) 0 sec, (b) 180 sec, (c) 360 sec, and (d) 720 sec; the flow rate was $0.02\mu l/min$. The length of the channel which is shown is about $240\mu m$ starting at $200\mu m$ from the inlet (for parallel configuration) and at the first energized electrode (for perpendicular configuration).

For comparison, Figures 4.9(a) – 4.9(d) show the results for the simulations of the particle motions under the same conditions as those for Figure 4.8, as would be observed through the channel top (i.e., only their x- and z- coordinates) in the region between the centers of two neighboring grounded electrodes for parallel arrangement of the electrodes, and in the region which includes first 6 pairs of the grounded and energized electrodes for the perpendicular arrangement of the electrodes.

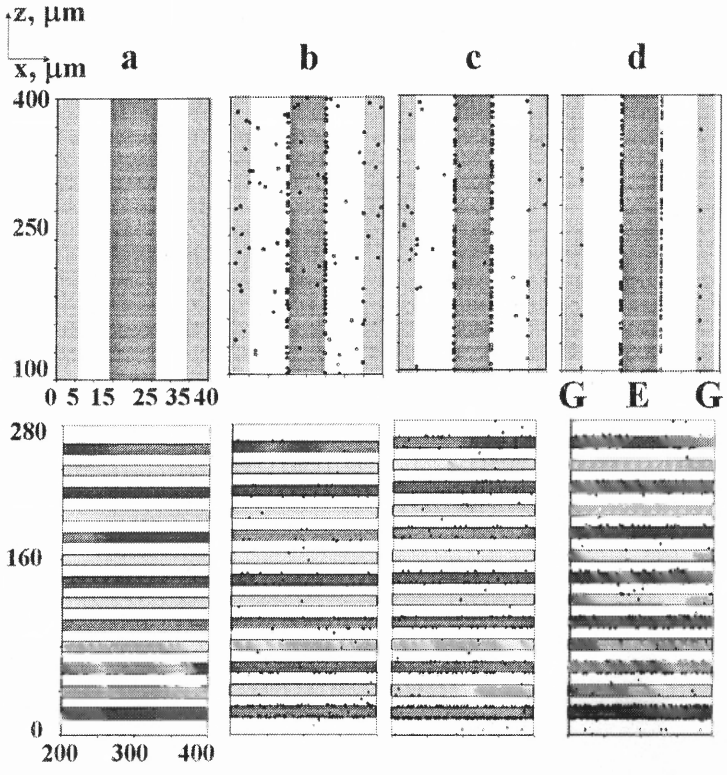

Figure 4.9 Simulation of the field-induced particle segregation along part of the channel starting at 100μm from the inlet (for parallel arrangement of the electrodes) and at the first energized electrode (for perpendicular electrode arrangement at the bottom) under the same conditions as those for Figure 4.8. The vector of the flow direction is oriented from the bottom to the top .The region which is shown for parallel electrodes configuration includes energized (E) and halves of neighboring grounded (G) electrodes. For the bottom set of pictures darker electrodes correspond to energized and lighter to grounded.

Figure 4.8(a) correspond to the time when there are no particles in the channel. At early times after the introduction of particles into the channel and application of the field, particles are seen to have moved towards the edges of the high-voltage electrode Figure 4.8(b) consistent with the simulations shown in Figure 4.9(b). After 3 min, a significant decrease in the number of particles was noted in the region between the electrodes and over the grounded electrodes Figure 4.8(c) very similar to that predicted in Figure 4.9(c). Finally, particles were found to form thin layers on the edges of the energized electrodes Figures 4.8(d)-4.9(d).

The photos presented in Figures 4.10 and 4.11 illustrate the spatial distribution of the particles which have been collected during 15 min in channels with the $10-\mu m$, $5-\mu m$, and $2-\mu m$ electrodes for the both array configurations. As expected, the majority of the particles segregated in the channels with the $10-\mu m$ electrodes are located on the energized electrodes. This selectivity lower, however, for the channels with the $5-\mu m$ electrodes, especially for the case of the electrode array arranged perpendicular to the flow, for which a sizable portion of the particles were trapped on the grounded electrodes. Photos in Figure 4.10(a),(b) demonstrate that the arrangement of the $10-\mu m$ and $5-\mu m$ electrodes parallel to the flow enables one to position the particles that have segregated on the energized electrodes closer to their edges. However, for the perpendicular case Figure 4.11(a),(b) a sizable portion of these particles appear to spread over the whole electrode. The perpendicular configuration of the electrode array also promotes the formation of multi-particle aggregates spanning the neighboring energized and grounded electrodes. The amount of particles trapped in the channels decreases sharply with a reduction in the electrode size and spacing for both types of the electrode

arrangement and nearly no particles were collected in the channel with the $2-\mu m$ electrodes arranged perpendicular to the flow (Figure 4.11(c)). A small population of the particles collected in the channels with the array of the $2-\mu m$ electrodes arranged parallel to the flow appear to be distributed nearly at random, mainly forming large aggregates which cover several energized and grounded electrodes (Figure 4.10(c)).

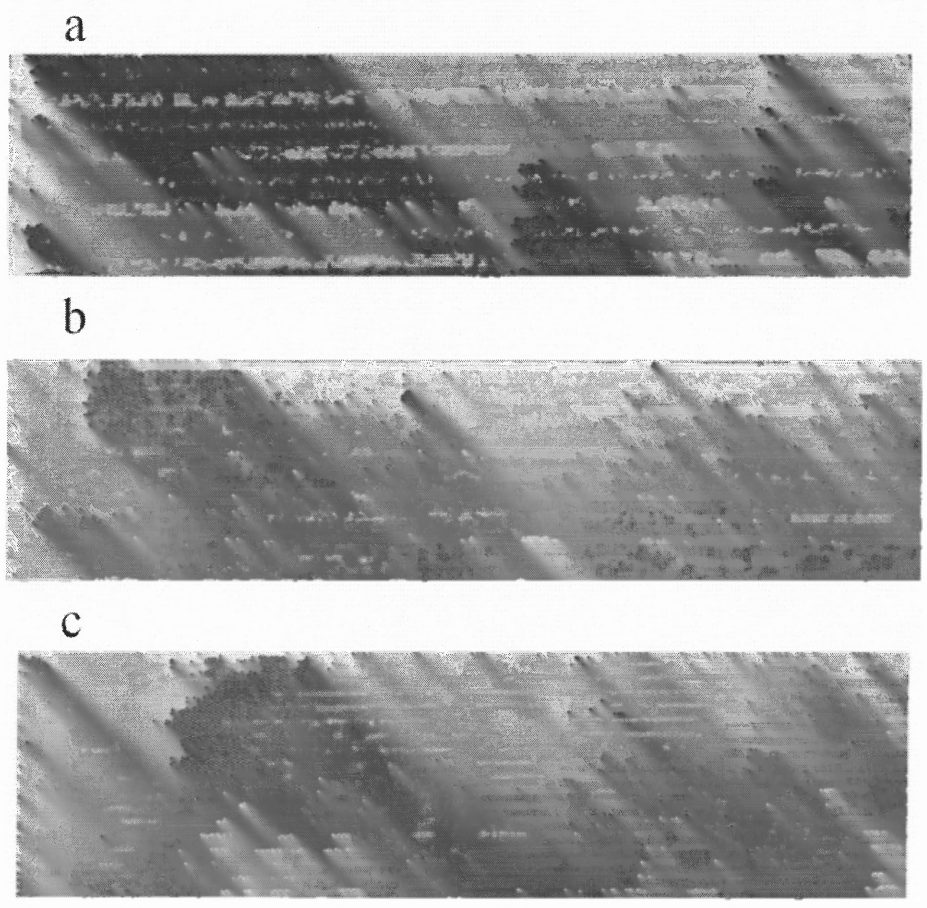

Figure 4.10 The distribution of the particles (*dark*) trapped in microfluidics with parallel arrangement of the electrodes with (a) $10-\mu m$, (b) $5-\mu m$, and (c) $2-\mu m$ electrodes (*white*) following the application of an 1kHz field with (a) 20 V_{rms}, (b) 10 V_{rms}, and (c) 7 V_{rms} to a flowing 0.1 (v/v) % suspension during 15 min; the flow rate was $0.02\mu l/min$. The part of the channel which, is shown starts from the inlet (on the left).

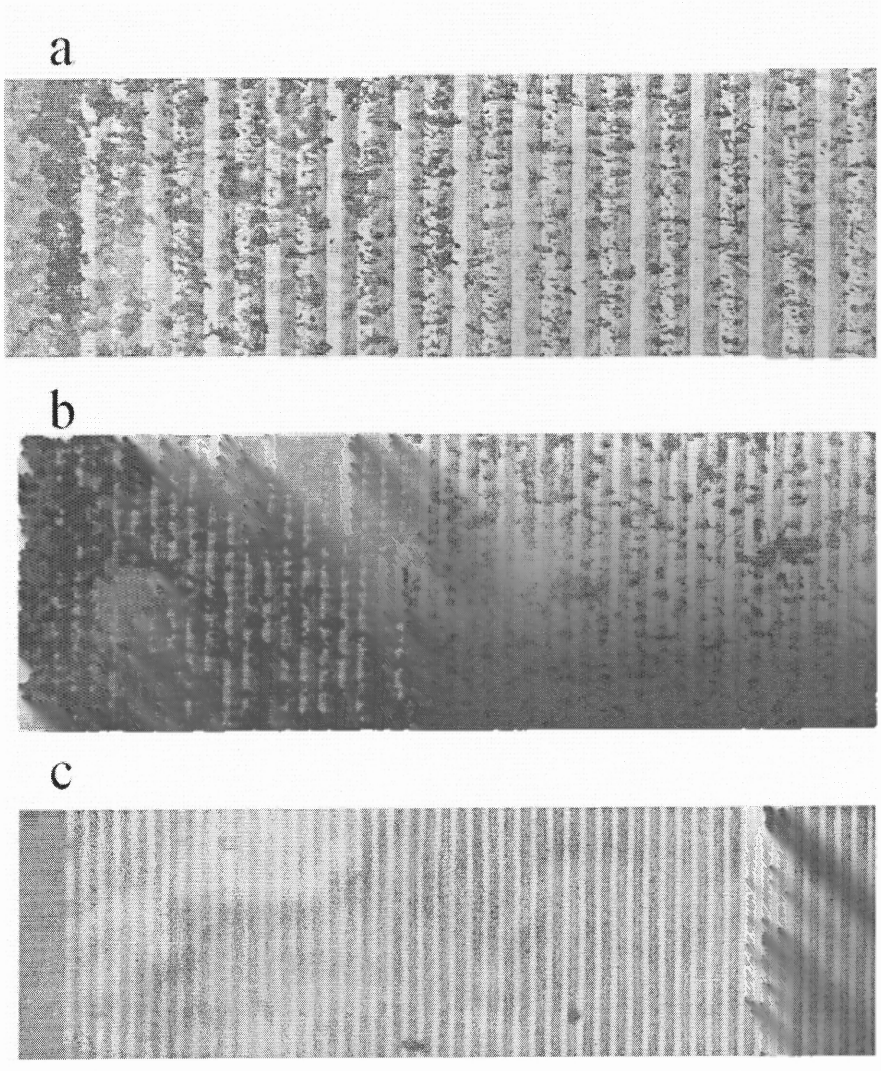

Figure 4.11 The distribution of the particles (*dark*) trapped in microfluidics with parallel arrangement of the electrodes with (a) $10-\mu m$, (b) $5-\mu m$, and (c) $2-\mu m$ electrodes (*white*) following the application of an 1kHz field with (a) 20 V_{rms}, (b) 10 V_{rms}, and (c) 7 V_{rms} to a flowing 0.1 (v/v) % suspension during 15 min; the flow rate was $0.02\,\mu l/min$. The part of the channel, which is shown starts from the inlet (on the left).

Based on Equation (1.19) for the dielectrophoretic force, one may expect that the use of smaller microelectrodes should benefit the precise and controlled manipulation of the particles because this force increases rapidly with decreasing d for the same magnitude of the field strength given that $\nabla \mathbf{E}_{rms}^2 \sim \mathrm{E}_{\mathrm{rms}}^2/\mathrm{d}$. In contrast, the photos in Figures 4.10, 4.11 clearly demonstrate that the precision in positioning the particles on the energized electrodes for both types of the electrode array arrangement decreases as the electrode size and spacing between them are reduced due to the presence of multi-particle aggregates covering several electrodes. To avoid the formation of such aggregates caused by the interparticle dipolar interactions, the dipole-dipole force, $\mathrm{F_{dd}}$, between two particles, one located on the grounded electrode and the other on the neighboring energized electrode, should be significantly smaller than the dielectrophoretic force, Equation (1.19), exerted on these particles. Using the expression for $\mathrm{F_{dd}}$ (Khusid and Acrivos, 1995), it was obtained that in order to meet this requirement the spacing between the electrodes d should satisfy the following inequality:

$$\mathrm{F_{dd}}/\mathrm{F_{dep}} \sim 6\,\mathrm{Re}(\beta)(\mathrm{a}/\mathrm{d})^3 \ll 1, \qquad (4.3)$$

where a is the particle radius. The photos in Figures 4.10,4.11 indicate the significance of this condition since $\mathrm{F_{dd}}/\mathrm{F_{dep}} \sim 5\cdot 10^{-3}$ for the $10-\mu\mathrm{m}$ electrode size and spacing, whereas $\mathrm{F_{dd}}/\mathrm{F_{dep}} \sim 0.7$ for the $2-\mu\mathrm{m}$ electrode size and spacing. Another requirement follows from the fact that the field strength gradient should be sufficiently large over the whole cross section of the channel in order for the particles to move towards the electrode array. Therefore, the electrode size and spacing (d)-to-the channel height (H) ratio, d/H, should not be too small, otherwise the dielectrophoretic force within the bulk of the

channel will not be of sufficient strength to move the particles over an appreciable distance. This is consistent with the observed significant reduction in the amount of collected particles for the $2-\mu m$ electrodes (d/H=0.07) as contrasted with that for the $10-\mu m$ electrodes (d/H=0.3) (Figures 4.10, 4.11).

Now consider the extent to which the predictions of the single-particle model, Equations (3.1) and (3.2) in Chapter 3, can be relied on. Depicted in Figure 4.12 are the computational results for the longitudinal variation of the fraction of the particles trapped on the electrodes under the same conditions as those for photos.

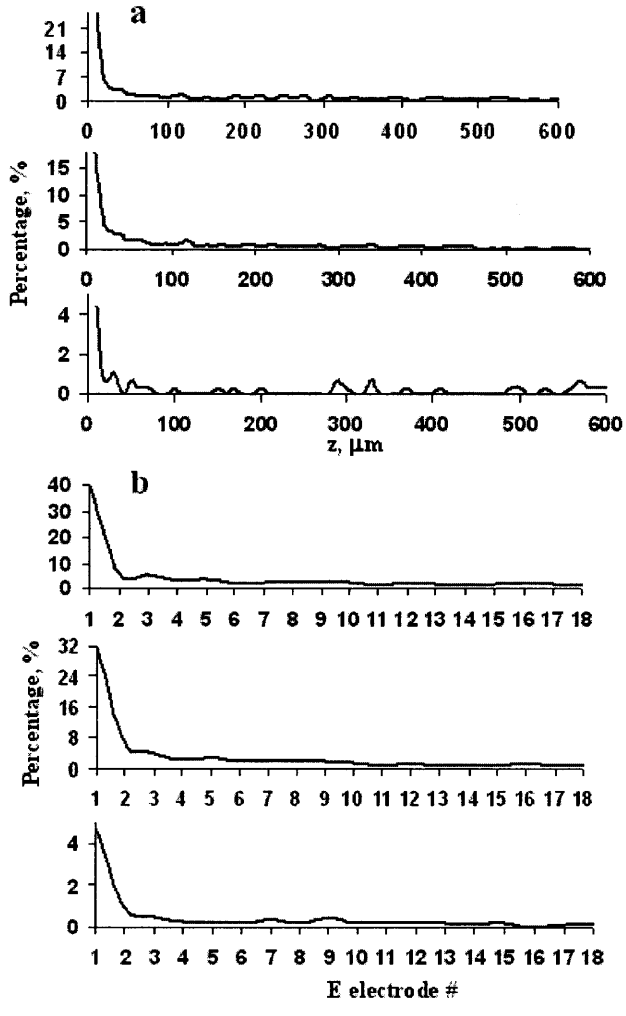

Figure 4.12 Longitudinal variation of captured particles computed in simulations and plotted as a percentage of total number of particles. (a) Parallel electrode configuration, electrode size from top to bottom: 10 μm, 5 μm, 2 μm. (b) Perpendicular electrode configuration, electrode size from top to bottom: 10 μm, 5 μm, 2 μm

Computational data are presented in accord with the image analysis procedure (Section 3.1A). Specifically for the electrode array perpendicular to the flow, the number of particles segregated on each energized electrode was computed, and divided by the total number of the particles, and then plotted the result against the electrode number. For the electrode array parallel to the flow, the number of the particles segregated over the $10-\mu m$ length of the energized electrode was calculated, and divided by the total number of particles, and plotted the result against the electrode length. In line with the experimental results, the simulations predict that the amount of the trapped particles decreases sharply in the entrance region and then slowly decreases further away from the inlet, fluctuating due to the relatively small population of the particles captured on a micron-scale area of the channel. Both the experimental and computational data show that the amount of the particles trapped at the same distance from the channel inlet decreases with a reduction in the electrode size and spacing.

The quantitative assessment of the theoretical predictions was conducted only for channels equipped with the $10-\mu m$ and $5-\mu m$ electrodes because most of the trapped particles formed multi-particle aggregates in channels with the $2-\mu m$ electrodes. The least-squares line method was used to compare the integral $\int_z^L (GL_0 - GL)\,dz$ with the fraction of the particles $P(z)$ to have traveled beyond a certain length of an energized electrode for the array arranged parallel to the flow or a certain number of an energized electrode for the array arranged perpendicular to the flow. This procedure enabled us to compare experimental and computational data in regions having a relatively low population of the trapped particles by reducing substantially the data fluctuations. The

comparison was conducted without using data from first three energized electrodes from the inlet for the perpendicular arrays and first $100-\mu m$ from the parallel arrays due to the fact that large amount of particles trapped in those regions covered more than a single layer. As can be seen from Figure 4.13 away from the channel inlet, the relation $\alpha\int_{z}^{L}(GL_0 - GL)\,dz = P(z)$ is satisfied with relatively large values of the correlation coefficient R^2. This demonstrates that the predictions of the single-particle model for the particle accumulation on the electrodes are in a reasonable agreement with experimental data when the channel characteristics meet the requirements given by Equations (4.2) and (4.3). The prediction of the particle aggregation patterns on the electrodes is well beyond the scope of this model.

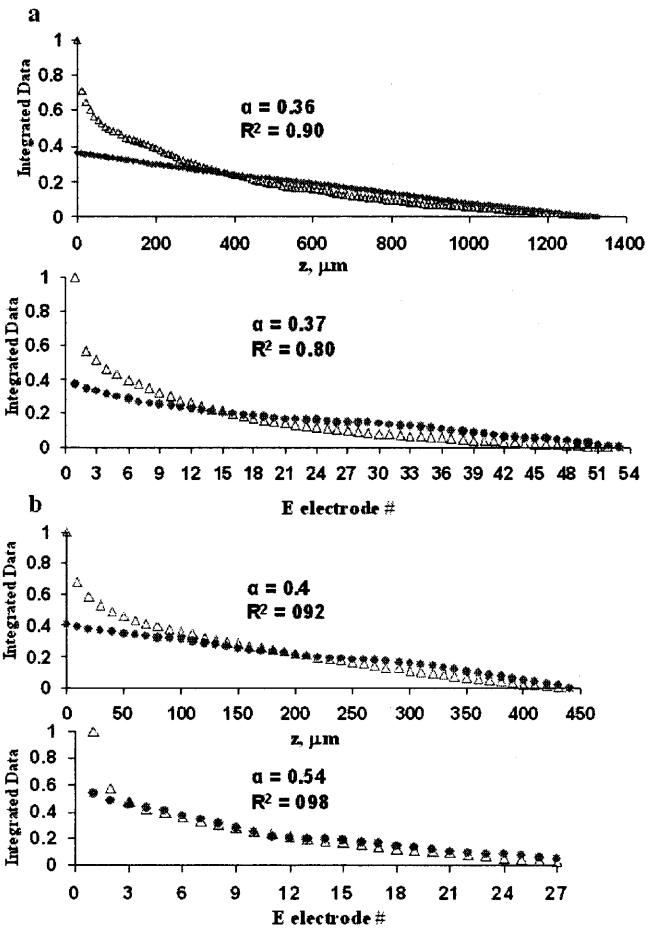

Figure 4.13 Comparison of the integral $\alpha\int_{z}^{L}(GL_0 - GL)\,dz$ (empty triangles) with the fraction of the particles that have traveled beyond the certain length $P(z)$(filled circles): (a) electrode size - 10 μm, parallel configuration (top), perpendicular configuration (bottom) (b) electrode size - 5 μm, parallel configuration (top), perpendicular configuration (bottom).

4.5 Conclusions and Main Results

Employing batch processes, 150 mechanically robust and chemically inert dielectrophoretic microfluidics were fabricated on a 4" silicon wafer. The developed technology is well suited for manufacturing multi-channel micro-devices and their integration into a higher-level system able to handle a flow rate by three orders of magnitude larger. The ac-field-induced motion and segregation of the positively polarized particles in a dilute suspension flowing through a micro-channel were studied experimentally and theoretically. Experiments were conducted on dielectrophoretic microfluidics equipped with electrodes of different sizes arranged parallel and perpendicular to the flow. Microfluidics were operated in the regime of the particle heterogeneous aggregation to prevent the field-induced structuring of the particles in the bulk of a channel. The simulations of the particle motions and their segregation required no fitting parameters because the suspension properties were measured independently.

It was demonstrated that the particles which segregated in the channel form multi-particle aggregates spanning neighboring ground and energized electrodes as long as their dipolar interactions become comparable with the dielectrophoretic force exerted on these particles. This imposes certain limitations, Equation (4.3), on the particle-to-the electrode sizes and spacings ratio in order to position the particles in the pre-selected locations of a micro-device, in contrast to the expectation that the miniaturization of microelectrodes should benefit the precise and controlled manipulation of the particles. Furthermore, the electrodes should not be very small in comparison with the channel height, for otherwise, the dielectrophoretic force which drives the particles towards the electrodes is not

sufficiently large over the whole channel cross section. When the device characteristics meet certain requirements, Equations (4.2) and (4.3), the theoretical predictions for the variation of the amount of the segregated particles along the channel were found to be quantitatively consistent with experimental data in a region away from the inlet, in which the particle population is relatively small. Combined with testing the predictions for the particle accumulation with time in a millimeter-scale channel (Chapter 3), this completes the experimental validation of a theory for the kinetics of dielectrophoretic phenomena in a flowing dilute suspension.

The results of these studies provide the basic characteristics of the ac-field-driven particle motions and segregation in a micro-channel and validate a simulation procedure needed for the design and operation of dielectrophoretic micro-fluidics.

CHAPTER 5

CONCLUSIONS

5.1 Dissertation Conclusions

The main goal of the presented research was to study experimentally and theoretically the motion and aggregation of highly polarizable particles in dilute suspensions subject to high-gradient ac electric fields. The theoretical predictions for the field-induced positive dielectrophoresis and phase transitions were tested in millimeter- and micrometer-scale channels. The model calculations required no fitting parameters because the suspension properties were determined independently.

For millimeter scale devices, the conditions under which a suspension of positively polarizable particles will undergo a heterogeneous aggregation following the application of a high-gradient strong ac field (~ several kV/mm) were specified theoretically, and then the field-induced particle motions and pattern formation in very dilute suspensions under these conditions were examined experimentally. In addition, to prevent the gravitational settling of the particles, a setup in which the electric chamber was kept slowly rotating around a horizontal axis along with a special technique to energize the electrodes was developed, and a single-particle model was used for the simulations of the field-induced particle motions. Also, the real part of the complex value of the particle polarization, which is required for the calculation of the dielectrophoretic force, was measured in a spatially uniform low-strength field (~ V/mm).

The predictions of the single-particle model for the kinetics of the particle accumulation on the electrodes were found to be in a reasonable agreement with

experimental data. This demonstrates that the value of the particle polarization measured in low fields can be used for describing the particle motions in strong fields. However, even in an initially very dilute suspension, interparticle interactions were found to govern the formation of arrays of bristles along the electrode edges. The experiments suggested the existence of a two-step mechanism for the formation of the arrays of bristles along the electrode edges, which arose from the interplay of the dielectrophoretic force that confined the particles near the electrode edge and the dipolar interactions of nearby particles.

The slow rotating electric chamber which has been developed makes feasible electro-hydrodynamic experiments on suspensions with particles heavier than the suspending fluid. This significantly extends the choice of suspension constituents which can be used in the experiments because it allows for a much broader variation of the polarization mismatch between the particles and the suspending fluid than is possible if only suspensions containing neutrally buoyant particles are used.

For micro-scale devices, the ac-field-induced motion and segregation of the positively polarized particles in a dilute suspension flowing through a micro-channel were studied experimentally and theoretically. It was demonstrated that the particles which segregated in the channel form multi-particle aggregates spanning neighboring ground and energized electrodes as long as their dipolar interactions become comparable with the dielectrophoretic force exerted on these particles. This imposes certain limitations, Equation (4.3), on the particle-to-the electrode size and interelectrode spacing ratio in order to position the particles in the pre-selected locations of a micro-device, in contrast to the expectation that the miniaturization of microelectrodes should benefit the

precise and controlled manipulation of the particles. Furthermore, the electrodes width and spacing should not be very small in comparison with the channel height, for otherwise, the dielectrophoretic force which drives the particles towards the electrodes is not sufficiently large over the whole channel cross section. When the device characteristics meet certain requirements, the theoretical predictions for the variation of the amount of the segregated particles along the channel were found to be quantitatively consistent with experimental data in a region away from the inlet, in which the particle population is relatively small.

Combined with testing the predictions for the particle accumulation with time in a millimeter-scale channeler, this completes the experimetal validation of a theory for the kinetics of dielectrophoretic phenomena in a flowing dilute suspension.

In summary, the results of presented studies (i) completed the experimental testing of theoretical predictions for the kinetics of dielectrophoretic phenomena in flowing dilute suspensions, (ii) provided the basic characteristics of the ac-field-driven particle motions and their segregation, and (iii) validated simulation procedures needed for the design and operation of dielectrophoretic devices.

APPENDIX

In order to evaluate the effects of gravity on the particle motions and their segregation, the experiments have been conducted in microgravity environment aboard the NASA research aircraft. This document describes the experimental setup and procedures of the microgravity experiments conducted at Glenn Research Center, Cleveland, OH, and is included in the dissertation with the permission of Prof. Andreas Acrivos.

TEST EQUIPMENT DATA PACKAGE

KC-135 Microgravity Aircraft Tests

1.0 Quick Reference Data Sheet

Principal Investigator:

Professor Andreas Acrivos

Contact Information:

The Levich Institute, Steinman Hall, T1M

The City College of New York / CUNY

140th Street and Convent Avenue, New York, NY 10031

Experiment Title:

Particle Segregation in a Flowing Concentrated Suspension Subject to High-Gradient Strong Electric Fields

Flight Date: October 2002

Overall Assembly Weight (lbs): 447 (267 +180)

Assembly Dimensions (Lx W x H): 48x44x32.5(in), 48x24x9

Equipment Orientation Requests: no special orientation required

Proposed Floor Mounting (Bolts/Studs or Straps): bolts

Gas Cylinder Requests (Type and Quantity): no gas cylinder required

Overboard Vent Requests (Yes or No): No

2.0 Flight Manifest

Dr. Boris Khusid, no flight on KC-135

Mr. Nikolai Markarian, no flight on KC-135

Dr. Anubhav Tripathi, no flight on KC-135

Mr. Mike Yeksel, no flight on KC-135

3.0 Experiment Background

On the basis of the results of our theoretical studies and earth-based experiments [1-4], we generated detailed requirements for low-gravity experiments. These experiments should provide rigorous tests of theoretical predictions for the field-induced particle motions and segregation in a gravity-free environment and better evaluate the effects of gravity-induced flows in ground-based experiments. The short-term KC-135 test project will constitute a basis for a long-term microgravity project.

4.0 Experiment Description

In the KC-135 experiments, a suspension of polarizable particles will be flowing through the Microgravity Dielectrophoretic Flow Device (MDFD) (also referred as a Rotating Chamber) in which it will be exposed to a high-gradient AC electric field. The data to be obtained will be crucial for the development of a theoretical model of electric-field-

driven phenomena in a flowing suspension. For comparison, we will conduct similar experiments in normal gravity environment.

5.0 Equipment Description

The MDFD (Rotating Chamber) includes an electric chamber rotating at 4 rpm to prevent the sedimentation of suspending particles during a gravity part of a flight parabola.
In experiments, we will use two suspensions which exhibit positive and negative dielectrophoresis and, correspondingly, demonstrate different segregation patterns. One of them is a suspension of hollow ceramic spheres (AVEKA) (53-63μm) dispersed in Mazola corn oil (incompressible fluid under test conditions with ρ=0.92 g/cm^3, η =59.7 cp at 23°C), whereas the other is a suspension of aluminum oxide (Al_2O_3) particles (45μm) dispersed in Mazola corn oil (ρ=1 g/cm^3, η=19.7 cp at 23°C). Only 30 ml of each suspension will be used to fill in the Rotating Chamber for one run.

List of system hardware

[1] High Voltage (HV) Power supply:

Radio frequency generator	Wavetek	(3.8 lb.)
High-voltage power amplifier	Model 10/40	(50.65 lb.)
Multi-meter	HP-34401A	(7.65 lb.)
Power Strip (Main strip)		(2.7 lb.)

The components of the unit [1] are bolted to an Aluminum 6061-T6 Plate (W24"xL48") which will be fastened to the aircraft floor. The weight of the plate with the attached components is 180 lbs

[2] Experimental Box:

Peristaltic pump	Masterflex , Model 7520-35	(13.7 lb.)
Silicone tubing	Masterflex , Model 96420-14	
MDFD (Rotating chamber)	Project	(4.5 lb.)
Step-motor	IDC, P32V	(9.2 lb.)
Controller	IDC, SmartStep, Microstepping smart drive	(2.45 lb.)
Light source	Moritex / MHF-G150LR	(8.35 lb.)
Digital camera	Panasonic PV-DV950	(1.8 lb.)
Power Strip		(2.7 lb.)

The components of unit [2] are fastened to the bottom of the acrylic box (44"WxL48"Lx32.5H") which will be bolted to the aircraft floor.

The weight of the acrylic box with the attached components is 267 lb (225+ weights of all components inside).

6.0 Structural Analysis

6.1 Components of Experimental Setup

Setup consists of Experimental Box and Power Supply Plate (Figures 1,2,3.)

Figure A1 Experimental Box.

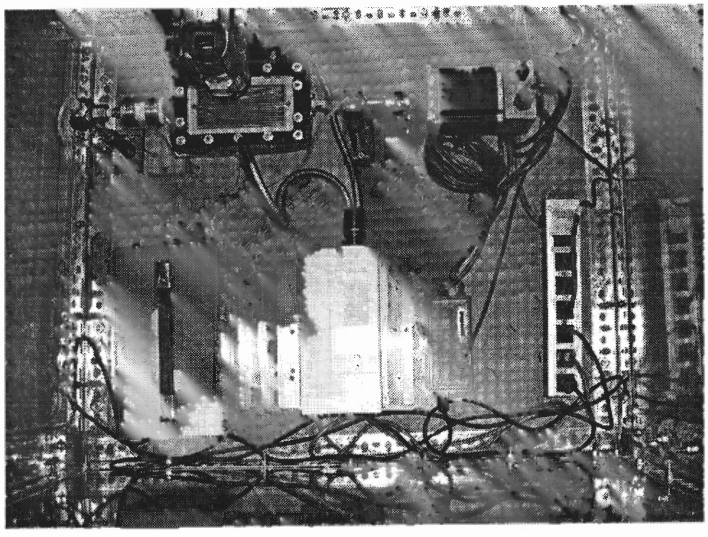

Figure A2 Open Experimental Box: top view.

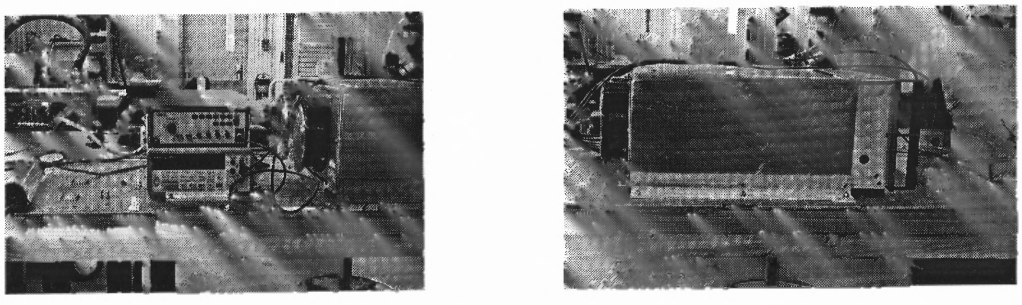

Figure A3 Power supply plate.

The components of the Experimental Box and the Power Supply Plate are listed in Tables 6.1, 6.2 respectively.

Table 6.1.

Component	Weight(lb)	Fasteners used
Rotating chamber	4.5	Mounted on the stands using 4 alloy steel bolts ¼''diameter
Step-Motor	9.2	Mounted on the acrylic bracket using 4 allow steel bolts ¼''diameter
Controller	2.45	1 stainless bolt ¼", 1 alloy steel bolt 1/8" diameter
Digital camera	1.8	4 allow steel bolts ¼''diameter
Light source	8.35	4 stainless steel bolts ¼''diameter
Pump and driver	13.7	4 alloy steel bolts ¼''diameter
Power Strip 1	1	2 alloy steel bolts ¼''diameter

The weight of the acrylic box is 225 lb

The overall weight of the Experimental Box is 267 lb

Table 6.2

Component	Weight(lb)	Fasteners used
Regulated power supply	56.5	Alloy steel and AN steel 10/32" diameter screws See drawing for details

Multi-meter & Function Generator	7.65+3.8= 11.45	Alloy steel and AN steel 10/32" diameter screws See drawing for details
Power Strip 2	1	2 alloy steel bolts ¼''diameter

The weight of the Aluminum plate is 107 lb

The overall weight of the Power Supply Plate is 180 lb

6.2 A sketch of Experimental Setup

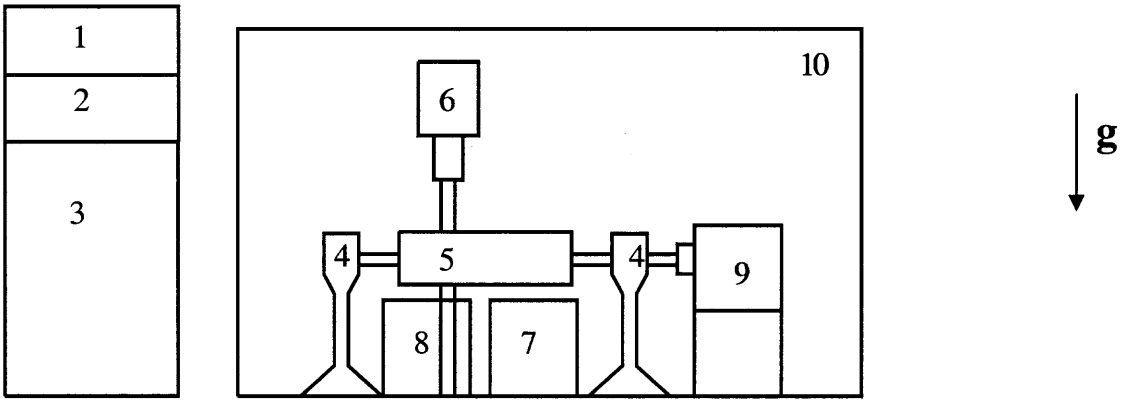

1	**Multimeter**
2	**Function Generator**
3	**High Voltage Amplifier**
4	**Standings**
5	**Rotating Chamber**
6	**Camera**
7	**Pump**
8	**Light source**
9	**Step Motor**
10	**Acrylic Box**

The sharp edges of the acrylic box are padded with a soft material.

All components of the experimental setup are fastened to the bottom plate of the box by the use of, at least, 4 fasteners, (alloy steel bolts ¼ " in diameter). Bolts that were used to assemble an acrylic box are of type SAE J429 grade 8 150000psi (min)

Components of the HV Power Supply Plate are secured using Aluminum 6061-T6 plates and AN steel and Alloy steel bolts 10/32 " in diameter . (see Drawings at the end of this document for details).

6.3 Stress Analysis

6.3.1 Power Supply Plate

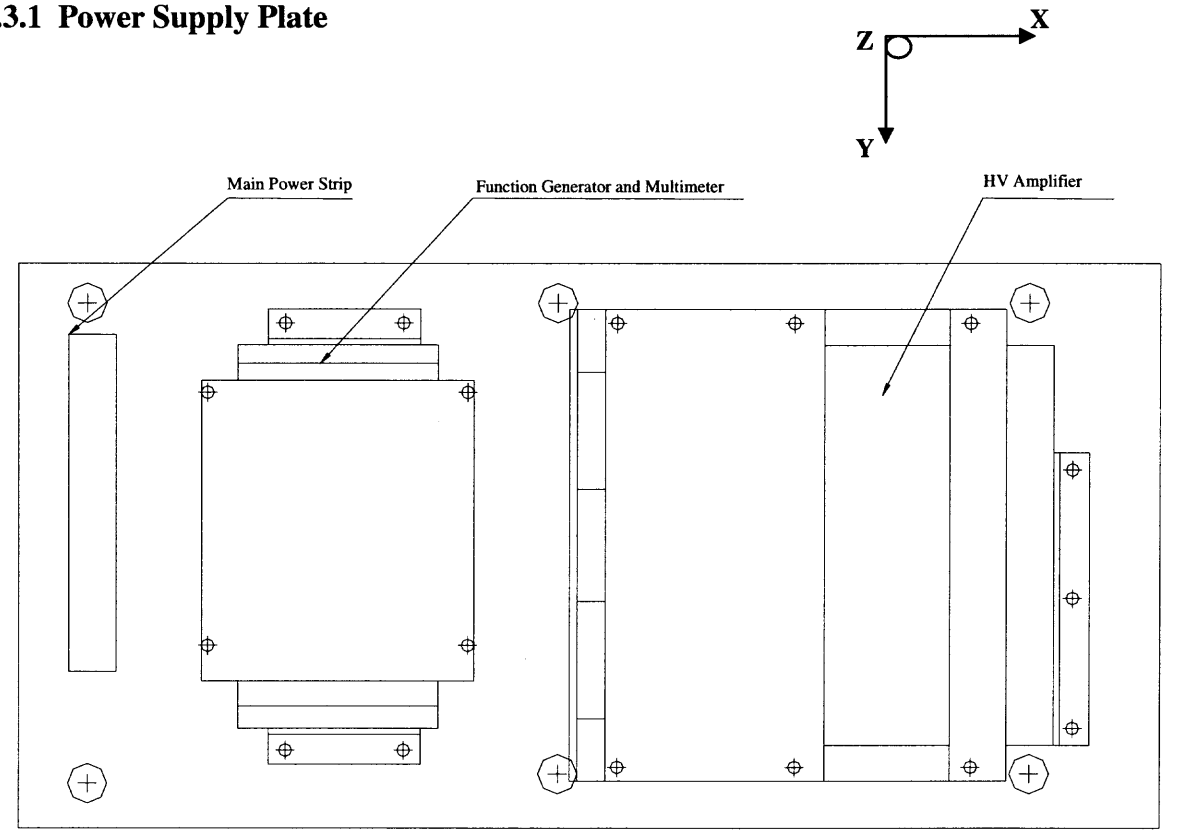

All Components are attched using Aluminum 6061-T6 sheets
with Ø 10/32 Alloy steel and AN steel screws

Load on HV Amplifier fastened to the Power Supply Plate (see Drawings at the end of this document for detailed dimensions)

For Alloy Steel 10-32 screws :

Tensile Ultimate Stress

S_{UT} = 140 ksi

Tensile Yield Stress

S_{YT} = 120 ksi

Shear Ultimate Stress

S_{US} = 84 ksi

Shear Yield Stress

S_{YS} = 70 ksi

Shear Area:

A_s= 0.02835 in^2

Tensile Root Area:

$A_{T,R}$= 0.0175 in^2

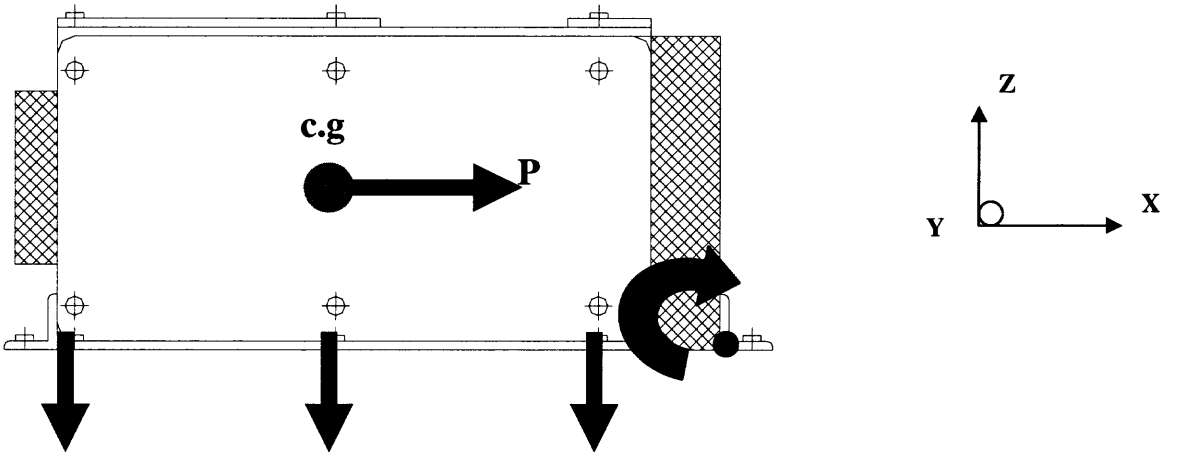

9g load in positive X direction :

Note: Only the bottom 6 Alloy Steel fasteners are considered.

Addition of the top fasteners will only strengthen the assembly, therefore they are ignored.

If safety factors calculated by this method prove unsatisfactory, the top fasteners will be considered in a revision of this analysis.

P = 9W = 9*50.7 = 456.3lb

The HV amplifier is fastened by 6 of the 10-32 Alloy Steel screws.

Maximum Shear Reaction Load:

$R_{s\,max}$ = P/6 = 76lb

Maximum Tensile Reaction Load:

$$R_T = \frac{Pld_{max}}{\sum_i nd_i^2} = \frac{456.3*4.5*18.5}{2((3.5)^2+11^2+(18.5)^2)} = 40\text{lb}$$

Tensile Stress:

$$\sigma = \frac{40}{0.0175} = 2290 psi$$

$$\sigma_1 = \sqrt{2680^2 + 2290^2} = 3525 psi$$

Shear Stress:

$$\tau = \frac{76}{0.02835} = 2680 psi$$

$$\tau_1 = \frac{\sigma_1}{2} = 1765 psi$$

Margins of Safety:

$$M.S_{TU} = \frac{S_{UT}}{\sigma_1} - 1 = \frac{140}{3.53} - 1 = 38.7$$

$$M.S_{TY} = \frac{S_{YT}}{1.5\sigma_1} - 1 = \frac{120}{1.5*3.53} - 1 = 21.7$$

$$M.S_{SU} = \frac{S_{US}}{\tau_1} - 1 = \frac{84}{1.77} - 1 = 46.4$$

$$M.S_{SY} = \frac{S_{YS}}{1.5\tau_1} - 1 = \frac{70}{1.5*1.77} - 1 = 26.4$$

Bearing Load:

For 1/8 " Aluminum (6061-T6) Sheet:

S_{bru} = 88ksi

S_{bry} = 58ksi (Ref. MIL-HDBK-5F page 3-234)

Breaking Stress:

$$F_{br} = \frac{R_T}{d_{bolt} h_{sheet}} = \frac{40}{0.19 * \frac{1}{8}} = 1684 psi$$

$$M.S_{bry} = \frac{S_{bry}}{1.5F_{br}} - 1 = \frac{58}{1.5*1.68} - 1 = 22.0$$

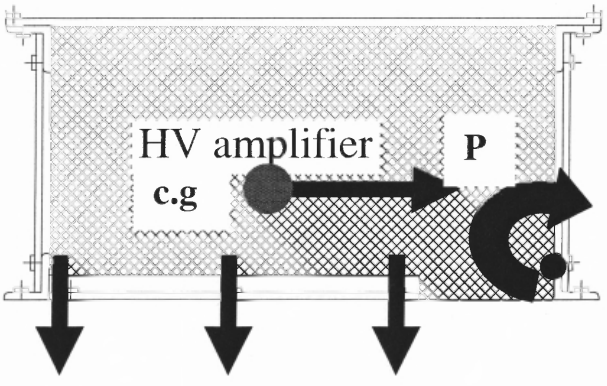

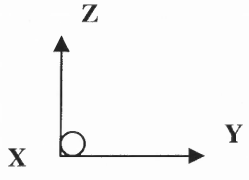

9g load in positive or negative Y direction:

See Note for calculation of load in X direction

P = 9W = 9*50.7 = 456.3lb

The HV amplifier is fastened by 6 of the 10-32 Alloy Steel screws.

Maximum Shear Reaction Load:

$R_{s\,max}$ = P/6 = 76lb

Maximum Tensile Reaction Load in positive Y direction:

$$R_{Tmax} = \frac{Pld_{max}}{\sum_i nd_i^2} = \frac{456.3*4.5*17}{3((1.5)^2+17^2)} = 40\text{lb}$$

So the loads are the same as in the previous case.

Therefore calculations from previous case hold and all the safety margins are the same.

$$M.S_{TU} = \frac{S_{UT}}{\sigma_1} - 1 = \frac{140}{3.53} - 1 = 38.7$$

$$M.S_{TY} = \frac{S_{YT}}{1.5\sigma_1} - 1 = \frac{120}{1.5*3.53} - 1 = 21.7$$

$$M.S_{SU} = \frac{S_{US}}{\tau_1} - 1 = \frac{84}{1.77} - 1 = 46.4$$

$$M.S_{SY} = \frac{S_{YS}}{1.5\tau_1} - 1 = \frac{70}{1.5*1.77} - 1 = 26.4$$

$$M.S_{bry} = \frac{S_{bry}}{1.5F_{br}} - 1 = \frac{58}{1.5*1.68} - 1 = 22.0$$

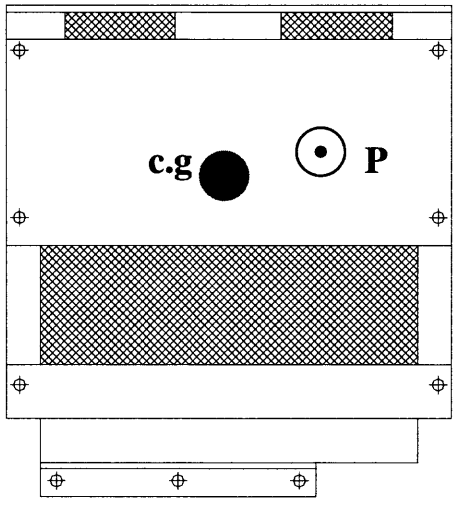

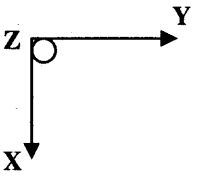

2g load in Z direction:

6 Top AN steel fasteners will be considered

P = 2W =2*50.7 = 101.4lb

Maximum Compressive Reaction Load:

$R_{T\,max}$ = P/6 = 16.9lb

Maximum Shear Reaction Load:

$$R_{smax} = \frac{Pld_{max}}{\sum_i nd_i^2} = \frac{104.2*9.5*4.5}{6((4.5)^2)} = 36.6\text{lb}$$

Total loads per bolts in this case are much less than in 9g loading regimes in X and Y directions. So, the safety margins will be greater.

Load on Multimeter and Function Generator attachment brackets fastened to the Power Supply Plate

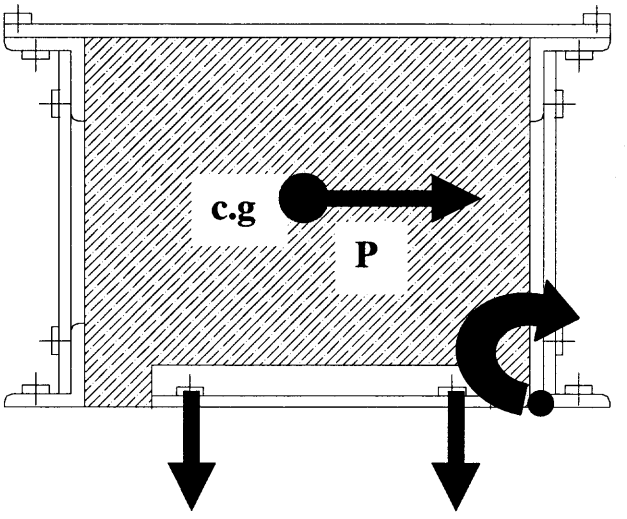

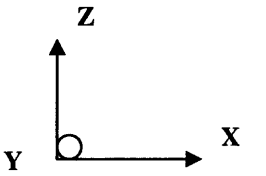

9g load in positive or negative X direction:

Note: Only the bottom 4 Alloy Steel fasteners are considered.

Addition of the top fasteners will only strengthen the assembly, therefore they are ignored.

If safety factors calculated by this method prove unsatisfactory, the top fasteners will be considered in a revision of this analysis.

The Weight of this assembly is 13 lb

P = 9W = 9*13 = 117lb

The brackets are fastened by 4 of the 10-32 Alloy Steel screws.

Maximum Shear Reaction Load:

$R_{s\,max} = P/4 = 29.3lb$

Maximum Tensile Reaction Load:

$$R_T = \frac{Pld_{max}}{\sum_i nd_i^2} = \frac{117*3.5*7}{2((2)^2+7^2)} = 27lb$$

This loads per-bolt are less than previously considered HV amplifier assembly loads, therefore, the safety margins will be greater.

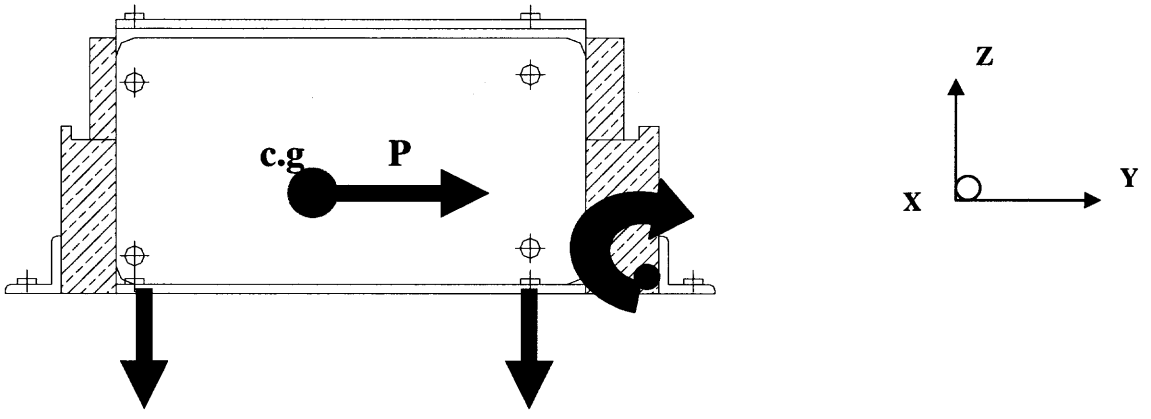

9g load in positive or negative Y direction:

Note: Only the bottom 4 Alloy Steel fasteners are considered.

Addition of the top fasteners will only strengthen the assembly, therefore they are ignored. If safety factors calculated by this method prove unsatisfactory, the top fasteners will be considered in a revision of this analysis.

P = 9W = 9*13 = 117lb

The brackets are fastened by 4 of the 10-32 Alloy Steel screws.

Maximum Shear Reaction Load:

$R_{s\,max}$ = P/4 = 29.3lb

Maximum Tensile Reaction Load:

$$R_T = \frac{Pld_{max}}{\sum_i nd_i^2} = \frac{117*3.5*14}{2((3.5)^2+14^2)} = 13.8\text{lb}$$

This loads per-bolt are less than previously considered HV amplifier assembly loads, therefore, the safety margins will be greater.

2g load in Z direction:

4 Top AN steel fasteners will be considered

P = 2W =2*13 = 26lb

Maximum Compressive Reaction Load:

$R_{T\,max}$ = P/6 = 4.4lb

Maximum Shear Reaction Load:

$$R_{smax} = \frac{Pld_{max}}{\sum_i nd_i^2} = \frac{26*5.5*3.5}{6((3.5)^2)} = 36.6\text{lb}$$

Total loads per bolts in this case are much less than in 9g loading regimes in X and Y directions. So, the safety margins will be greater.

6.3.2 Experimental Box

All of the components mounted in the Experimental Box were pull-tested and qualified to withstand 9g load in positive and negative X and Y directions, 6g in negative Z, and 2g in positive Z direction. See Drawings at the end of this document for details.

Stress Analysis of the Experimental Box:

Load on the "Foot-Print" Strips.

The "Foot-Print" Strips are fastened to the air-plane floor by six 3/8'' aircraft bolts.

Material values for alloy steel 3/8'' bolts will be used.

Because the bolts used are stronger than alloy steel 3/8'' bolts, the safety margins calculated will not be negatively affected.

For Alloy Steel 3/8'' bolts:

Tensile Ultimate Stress

S_{UT} = 140 ksi

Tensile Yield Stress

S_{YT} = 120 ksi

Shear Ultimate Stress

S_{US} = 84 ksi

Shear Yield Stress

S_{YS} = 70 ksi

Shear Area:

A_s= 0.11045 in^2

Tensile Root Area:

$A_{T,R}$= 0.0809 in^2

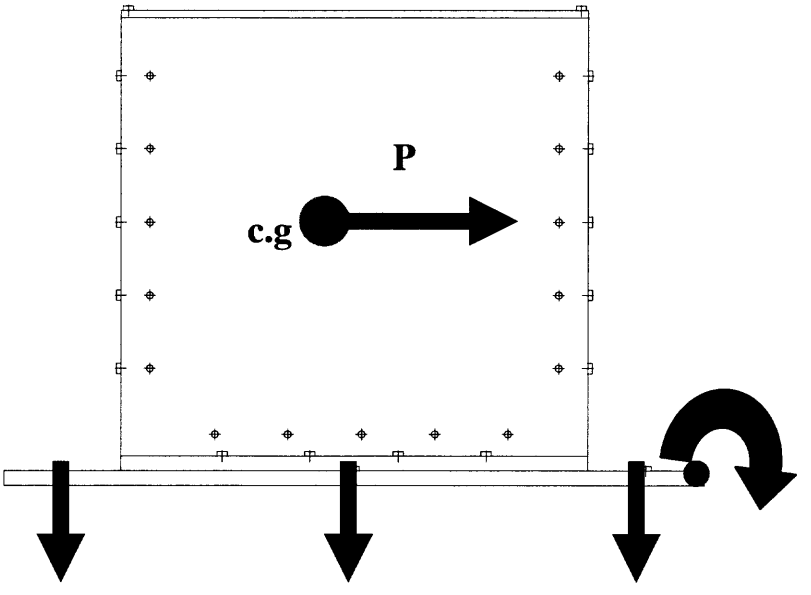

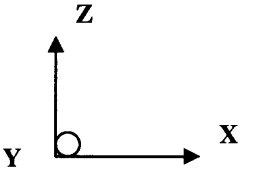

9g load in positive or negative X direction:

The Weight of this assembly is 267 lb.

P = 9W = 9*267 = 2403 lb

Maximum Shear Reaction Load:

$R_{s\,max} = P/6 = 401lb$

Maximum Tensile Reaction Load:

$$R_T = \frac{Pld_{max}}{\sum_i nd_i^2} = \frac{2403*16.25*44}{2(4^2+24^2+44^2)} = 371 \text{ lb}$$

Tensile Stress:

$$\sigma = \frac{371}{0.0809} = 4586 psi$$

$$\sigma_1 = \sqrt{4586^2 + 3631^2} = 5850 psi$$

Shear Stress:

$$\tau = \frac{401}{0.11045} = 3631 psi$$

$$\tau_1 = \frac{\sigma_1}{2} = 2925 psi$$

Margins of Safety:

$$M.S_{TU} = \frac{S_{UT}}{\sigma_1} - 1 = \frac{140}{5.85} - 1 = 22.9$$

$$M.S_{TY} = \frac{S_{YT}}{1.5\sigma_1} - 1 = \frac{120}{1.5*5.85} - 1 = 12.6$$

$$M.S_{SU} = \frac{S_{US}}{\tau_1} - 1 = \frac{84}{2.93} - 1 = 28.6$$

$$M.S_{SY} = \frac{S_{YS}}{1.5\tau_1} - 1 = \frac{70}{1.5*2.93} - 1 = 14.9$$

Bearing Load:

For 1'' Acrylic Sheet:

$S_{bry} = 9.0$ ksi

Breaking Stress:

$$F_{br} = \frac{R_T}{d_{bolt} h_{sheet}} = \frac{371}{0.375 * 1} = 989 psi$$

$$M.S_{bry} = \frac{S_{bry}}{1.5 F_{br}} - 1 = \frac{9.0}{1.5 * 0.99} - 1 = 5.0$$

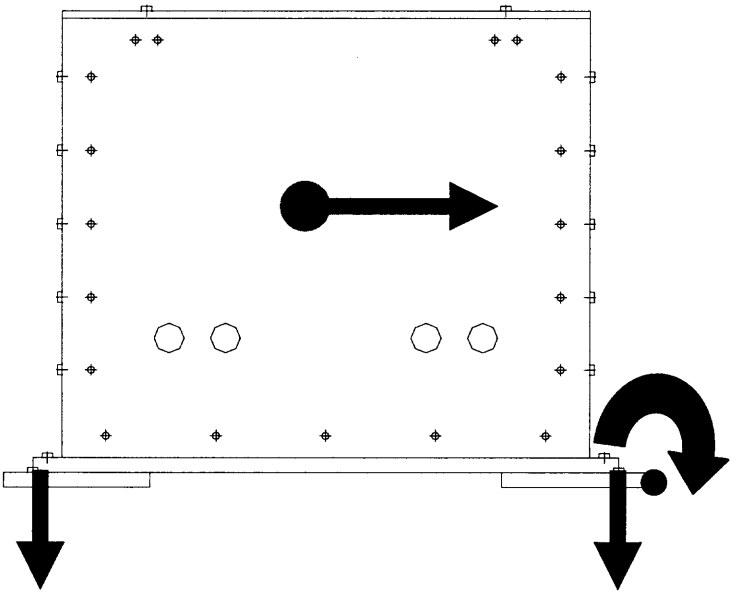

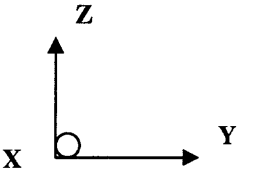

9g load in positive or negative Y direction:

The Weight of this assembly is 267 lb.

P = 9W = 9*267 = 2403 lb

Maximum Shear Reaction Load:

$R_{s\,max}$ = P/6 = 401lb

Maximum Tensile Reaction Load:

$$R_T = \frac{Pld_{max}}{\sum_i nd_i^2} = \frac{2403 * 16.25 * 42}{3(2^2 + 42^2)} = 335 \text{ lb}$$

The load per bolt is less or equal to one considered above, therefore the safety margins for this case will be greater.

2g load in Z direction:

P = 2W =2*267 = 534 lb

Maximum Tensile Reaction Load:

$R_{T\,max}$ = P/6 = 89lb

Maximum Shear Reaction Load:

$$R_{smax} = \frac{Pld_{max}}{\sum_i nd_i^2} = \frac{534*20*16.25}{6((16.25)^2)} = 110 \text{ lb}$$

The load per bolt in this case are much less than in 9g loading regimes in X and Y directions. So, the safety margins will be greater.

Load on the bolts connecting the "Foot-Print" Strips to the experimental box.

The "Foot-Print" Strips are connected to the experimental box by eight ¼'' grade 5 cap screws.

Material values for alloy steel ¼'' bolts will be used.

Because the bolts used are stronger than alloy steel ¼'' bolts, the safety margins calculated will not be negatively affected.

For Alloy Steel ¼'' bolts:

Tensile Ultimate Stress

S_{UT} = 140 ksi

Tensile Yield Stress

S_{YT} = 120 ksi

Shear Ultimate Stress

S_{US} = 84 ksi

Shear Yield Stress

S_{YS} = 70 ksi

Shear Area:

A_s= 0.04909 in^2

Tensile Root Area:

$A_{T,R}$= 0.0269 in^2

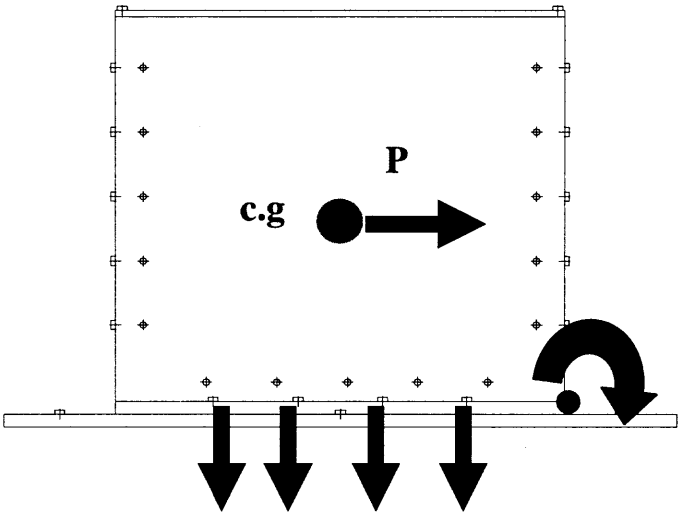

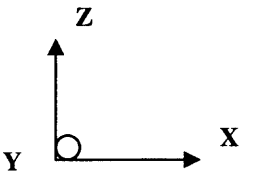

9g load in positive or negative X direction:

The Weight of the experimental box is 250 lb.

P = 9W = 9*250 = 2250 lb

Maximum Shear Reaction Load:

$R_{s\,max}$ = P/8 = 282 lb

Maximum Tensile Reaction Load:

$$R_T = \frac{Pld_{max}}{\sum_i nd_i^2} = \frac{2250*15*25}{2(7^2+13^2+19^2+25^2)} = 344 \text{ lb}$$

Tensile Stress: Shear Stress:

$$\sigma = \frac{344}{0.0269} = 12807\,psi \qquad \tau = \frac{282}{0.04909} = 5745\,psi$$

$$\sigma_1 = \sqrt{12807^2 + 5745^2} = 14037\,psi \qquad \tau_1 = \frac{\sigma_1}{2} = 7019\,psi$$

Margins of Safety:

$$M.S_{TU} = \frac{S_{UT}}{\sigma_1} - 1 = \frac{140}{14.03} - 1 = 8.9$$

$$M.S_{TY} = \frac{S_{YT}}{1.5\sigma_1} - 1 = \frac{120}{1.5*14.03} - 1 = 4.7$$

$$M.S_{SU} = \frac{S_{US}}{\tau_1} - 1 = \frac{84}{7.02} - 1 = 10.9$$

$$M.S_{SY} = \frac{S_{YS}}{1.5\tau_1} - 1 = \frac{70}{1.5*7.02} - 1 = 5.6$$

Bearing Load:

For 1'' Acrylic Sheet:

S_{bry} = 9.0 ksi

Breaking Stress:

$$F_{br} = \frac{R_T}{d_{bolt} h_{sheet}} = \frac{344}{0.25*1} = 1376\,psi$$

$$M.S_{bry} = \frac{S_{bry}}{1.5F_{br}} - 1 = \frac{9.0}{1.5*1.38} - 1 = 3.3$$

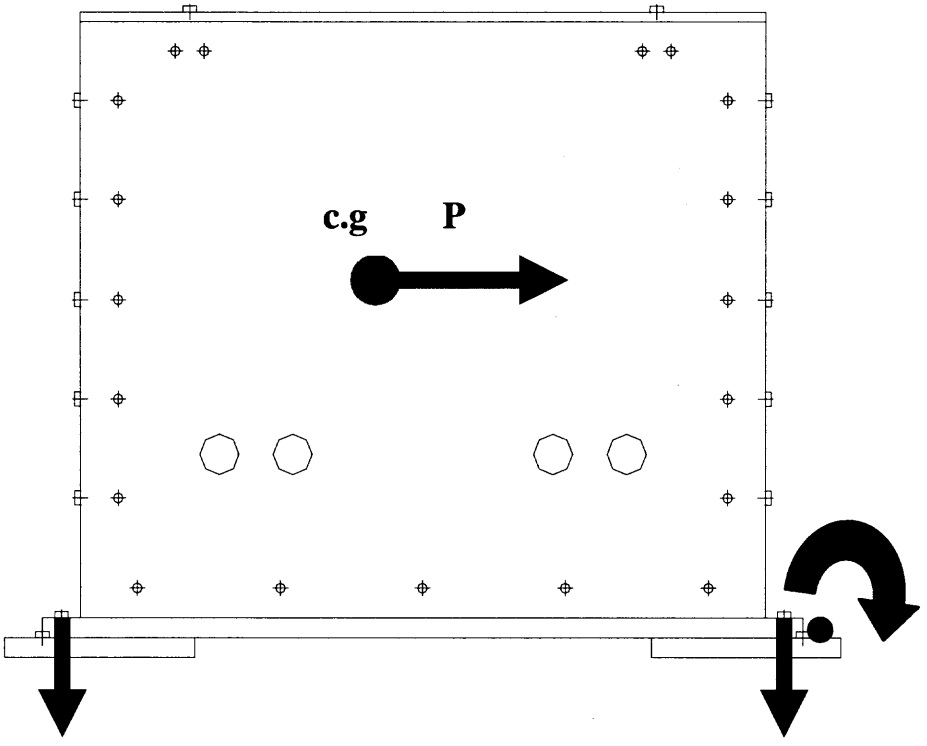

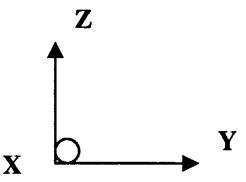

9g load in positive or negative Y direction:

The Weight of the experimental box is 250 lb.

P = 9W = 9*250 = 2250 lb

Maximum Shear Reaction Load:

$R_{s\,max}$ = P/8 = 282 lb

Maximum Tensile Reaction Load:

$$R_T = \frac{Pld_{max}}{\sum_i nd_i^2} = \frac{2250*15*39}{4(1^2+39^2)} = 218 \text{ lb}$$

The load per bolt is less or equal than the load in X direction considered above, therefore the safety margins for this case will be greater.

2g load in positive Z direction:

P = 2W =2*250= 500 lb

Maximum Tensile Reaction Load:

$R_{T\,max} = P/8 = 63lb$

Maximum Shear Reaction Load:

$$R_{smax} = \frac{Pld_{max}}{\sum_i nd_i^2} = \frac{500*20*15}{8((15)^2)} = 84 \text{ lb}$$

The load per bolt in this case are much less than in 9g loading regimes in X and Y directions. So, the safety margins will be greater.

6g load in negative Z direction is qualified by pull-test. (see Pull Test Results)

Load on bolts connecting box walls.

The box walls are 0.5'' acrylic plates weighing 37.5 lb each. They are connected to each other and the bottom with fifteen ¼'' grade 8 bolts on each wall. (total of 60 bolts)

Material values for alloy steel 1/4'' bolts will be used.

Because the bolts used are stronger than alloy steel 3/8'' bolts, the safety margins calculated will not be negatively affected

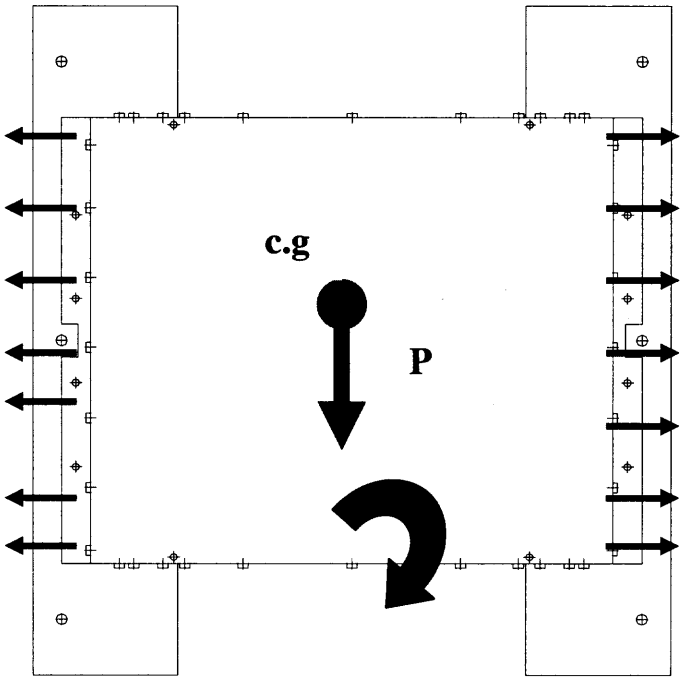

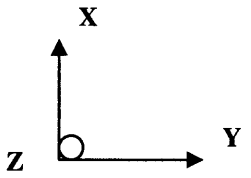

The box is symmetrical with respect to X and Y, therefore only one case of 9g loading in Y direction will be considered

The Weight of the 4 walls is 150 lb.

P = 9W = 9*150 = 1350 lb

Maximum Shear Reaction Load:

$R_{s\,max}$ = P/30 = 45 lb

Maximum Tensile Reaction Load:

$$R_T = \frac{Pld_{max}}{\sum_i nd_i^2} = \frac{1350*18*16}{2(6^2+11^2+16^2+21^2+26^2)+2(3^2+(7.5)^2+15^2+(22.5)^2+30^2)} = 61\text{lb}$$

The per-bolt load is much less than in the case of experimental box to "foot-print" strip connection, and the bolts used in calculation are the same.

Therefore, the safety factors for bolt loads will be greater.

For 0.5'' Acrylic Sheet:

S_{bry} = 9.0 ksi

Breaking Stress:

$$F_{br} = \frac{R_T}{d_{bolt} h_{sheet}} = \frac{29}{0.25 * 0.5} = 232 psi$$

$$M.S_{bry} = \frac{S_{bry}}{1.5 F_{br}} - 1 = \frac{9.0}{1.5 * 0.23} - 1 = 25$$

2g load in Z direction:

P = 2W =2*150= 300 lb

Maximum Tensile Reaction Load:

$R_{T\,max}$ = P/20 = 15lb

Maximum Shear Reaction Load:

$$R_{smax} = \frac{Pld_{max}}{\sum_i nd_i^2} = \frac{300 * 19 * 15}{20((15)^2)} = 19 \text{ lb}$$

The load per bolt in this case are much less than in 9g loading regimes in X and Y directions. So, the safety margins will be greater.

Load on bolts connecting the lid to the box.

The lid is a 0.5'' acrylic plate with a weight of 37.5 lb

It is connected to the box with four ¼'' alloy steel bolts

Considering the worst direction of 9g load:

P = 9W = 9*37.5 = 338 lb

Maximum Shear Reaction Load:

$R_{s\,max}$ = P/4 = 84 lb

Maximum Tensile Reaction Load:

$$R_T = \frac{Pld_{max}}{\sum_i nd_i^2} = \frac{338*0.25*38}{2((5.75)^2+(30.25)^2)} = 2 \text{ lb}$$

The per-bolt load is much less than in the case of experimental box to "foot-print" strip connection.

Therefore, the safety factors will be greater.

Calculation of the Pullout Load for Threaded Hole

The following calculations are carried out according to the Fastener Design Manual, NASA Reference Publication [5].

Component information:

Material:	Acrylic sheet
Mean diameter of the threaded hole (d_m)	¼ "
Length of the threaded engagement (L)	¾ "
Maximum pullout load P_{max} (at 9g)	180 lb

$$P = (\pi d_m F_s L)/3$$

$$P = 902 \text{ lb}$$

$$MS = P_{max} / P$$

M.S. = 5

The threaded holes have an acceptable Margin of Safety according to the Pullout Load Calculation .

Ultimate Shear stress (F_s)	4600 psi
Ultimate Stress for bolt (σ_u)	140,000 psi
Yield Stress for bolt (σ_y)	100,000 psi

Maximum Stress for bolts $\sigma_{max} = P_{max} / (\pi d_m^2/4) = 2$ psi

$$M.S_y = \sigma_y / \sigma_{max} \text{ (based on yield stress) [10]}$$

$$M.S_u = \sigma_u / \sigma_{max} \text{ (based on ultimate stress)}$$

$$M.S = F.S_y = 50$$

The bolts have an acceptable Margin of Safety [10]

6.4 Finite Element Analysis of the Acrylic Box

Introduction

An analysis was necessary to determine whether the equipment housing's acrylic walls would remain intact if all the experimental equipment became unfastened and struck one of the acrylic walls with an acceleration nine times that of gravity at sea level (32.2 ft/s^2). The equipment's mass (45 lbm) and the gravitational acceleration (289.8 ft/s^2) were used to calculate the force that would be applied to one acrylic wall (405 lbf). This force was applied uniformly across the smallest acrylic wall (32"x30"), which under a uniform force would experience the maximum pressure (Table 8.4).

Table 6.4: Location of Maximum Pressure On Equipment Housing

Wall Position	Wall Dimensions (inches)	Wall Max. SA (inches squared)	Max. Applied Force (lbf)	Pressure (psi)	Result
Front	32x30x0.5	960.00	405	0.42	**Max Pres.**
Side	36x30x0.5	1080.00	405	0.38	**Int. Pres.**
Top	$36^{1}/_{8}$x30x0.5	1083.75	405	0.37	**Min. Pres.**

Materials and Methods

The front acrylic wall was modeled using the Pro/Engineer CAD software. The Pro/ENGINEER software was chosen because of its capabilities for creating detailed solid components, creating photo realistic renderings, and its ease in association with various Finite Element Analysis (FEA) Software [6]. The FEA static analysis was conducted with The Pro/MECHANICA software package. Pro/Mechanica was selected because it allows proper simulation of our static load case as well as providing a means to check our results with its multipass convergence algorithms [6]. Acrylic Material properties were applied to our CAD drawing (Table 8.5) [7].

Table 6.5 General Purpose Molded Acrylic Material Properties

PHYSICAL PROPERTIES	VALUES	COMMENTS	US / Other Units
Density, g/cc	1.18	Max=1.19 g/cc, Min=1.15 g/cc, Count=51	1.18 g/cc
Linear Mold Shrinkage, cm/cm	0.0047	Max=0.0065 cm/cm, Min=0.003 cm/cm, Count=30	0.0047 in/in
Melt Flow, g/10 min	6.2	Max=27 g/10 min, Min=0.9 g/10min, Count=45	6.2 g/10 min
Water Absorption, %	0.85	Max=2%, Min=0.3%, Count=27	0.85 %
Moisture Absorption at Equilibrium, %	0.3	Max=0.33%, Min=0.3%, Count=16	0.3 %
Hardness, Rockwell M	90.6	Max=97, Min=63, Count=26	90.6
Refractive Index	1.49	Max=1.498, Min=1.49, Count=25	1.49
Transmission, Visible, %	89.2	Max=93%, Min=80%, Count=42	89.2 %

Haze, %	33.2	Max=96%, Min=1%, Count=10	33.2 %

MECHANICAL PROPERTIES	VALUES	COMMENTS	US / Other Units
Tensile Strength, Yield, Mpa	73.5	Max=85 MPa, Min=55 MPa, Count=11	10,660 psi
Tensile Strength, Ultimate, Mpa	68.7	Max=79 MPa, Min=47 MPa, Count=41	9,964 psi
Shear Strength	60.0		9,000 psi
Elongation %; yield	4.5	Max=5%, Min=4%, Count=11	4.5 %
Modulus of Elasticity, GPa	3.1	Max=3.8 GPa, Min=2.2 GPa, Count=33	450 ksi
Flexural Modulus, GPa	3.3	Max=3.5 GPa, Min=3 GPa, Count=23	479 ksi
Flexural Yield Strength, Mpa	110	Max=138 MPa, Min=81 MPa, Count=31	15,954 psi
Impact Strength, Izod, J/cm	0.16	Max=0.2 J/cm, Min=0.12 J/cm, Count=23	0.30 ft-lb/in
Impact Strength, Unnotched Izod, J/cm	2.7	Max=2.7 J/cm, Min=2.7 J/cm, Count=1	5.1 ft-lb/in
Impact Strength, Charpy, J/cm^2	0.24	Max=0.4 J/cm^2, Min=0.2 J/cm^2, Count=16	1.1 ft-lb/in^2

Impact, Unnotched Charpy, J/cm²	2.6	Max=6 J/cm², Min=1.9 J/cm², Count=16	12 ft-lb/in²
Gardner Impact, J	0.73	Max=1.4 J, Min=0.23 J, Count=7	0.54 ft-lb
Compressive Yield Strength, MPa	110	Max=117 MPa, Min=100 MPa, Count=4	15,954 psi
Shear Modulus, GPa	1.4	Max=1.4 GPa, Min=1.4 GPa, Count=3	203 ksi
Tensile Creep Modulus, 1 hour, Mpa	2500	Max=2700 MPa, Min=1800 MPa, Count=9	362,595 psi
Tensile Creep Modulus, 1000 hours, MPa	1600	Max=1800 MPa, Min=1200 MPa, Count=10	232,061 psi

THERMAL PROPERTIES	VALUES	COMMENTS	US / Other Units
CTE, linear 20°C, μm/m-°C	72.9	Max=130 μm/m-°C, Min=60 μm/m-°C, Count=27	41 μin/in-°F
Deflection Temperature at 0.46 MPa, °C	94.1	Max=103°C, Min=80°C, Count=18	201 °F
Deflection Temperature at 1.8 MPa, °C	86.5	Max=100°C, Min=41°C, Count=47	188 °F
Vicat Softening Point, °C	94.2	Max=117°C, Min=47°C,	202 °F

		Count=42	
Melting Point, °C	130	Max=130°C, Min=130°C, Count=3	266 °F
Maximum Service Temperature, Air, °C	85.8	Max=103°C, Min=41°C, Count=47	186 °F
Glass Temperature, °C	100	Max=105°C, Min=100°C, Count=4	212 °F
Heat Capacity, J/g-°C	1.5	Max=1.47 J/g-K, Min=1.46 J/g-K, Count=10	0.36 BTU/lb-°F
Thermal Conductivity, W/m-K	0.2	Max=0.24 W/m-K, Min=0.19 W/m-K, Count=11	1.4 BTU-in/hr-ft²-°F
Oxygen Index, %	18	Max=18%, Min=18%, Count=7	18 %
Flammability, UL94 (5=V-0; 4=V-1; 3=V-2; 1=HB)	1	Max=HB, Min=HB, Count=36	1
Processing Temperature, °C	240	Max=250°C, Min=243°C, Count=6	464 °F

ELECTRICAL PROPERTIES	VALUES	COMMENTS	US / Other Units
Electrical Resistivity,	9.6E+14	Max=1E+15 ohm-cm,	9.6E+14

Ohm-cm		**Min=1E+14 ohm-cm, Count=20**	**Ohm-cm**
Surface Resistance, Ohm	**1.7E+15**	**Max=1E+16 ohm, Min=1E+14 ohm, Count=19**	**1.7E+15 Ohm**
Dielectric Constant	**3.2**	**Max=4, Min=2.8, Count=23**	**3.2**
Dielectric Constant, Low Frequency	**3.5**	**Max=4, Min=3, Count=23**	**3.5**
Dielectric Strength, kV/mm	**28.8**	**Max=60 kV/mm, Min=17.7 kV/mm, Count=31**	**732 kV/in**
Dissipation Factor	**0.064**	**Max=0.55, Min=0.03, Count=20**	**0.064**
Dissipation Factor, Low Frequency	**0.07**	**Max=0.55, Min=0.04, Count=20**	**0.07**
Comparative Tracking Index, V	**600**	**Max=600 V, Min=600 V, Count=16**	**600 V**

Constraints were applied to the screw holes to simulate the bolts holding the acrylic walls together. A pressure (405 lbf) was then applied uniformly along the front acrylic wall to simulate a worst-case scenario of all the equipment crashing against one wall (Figure 4).

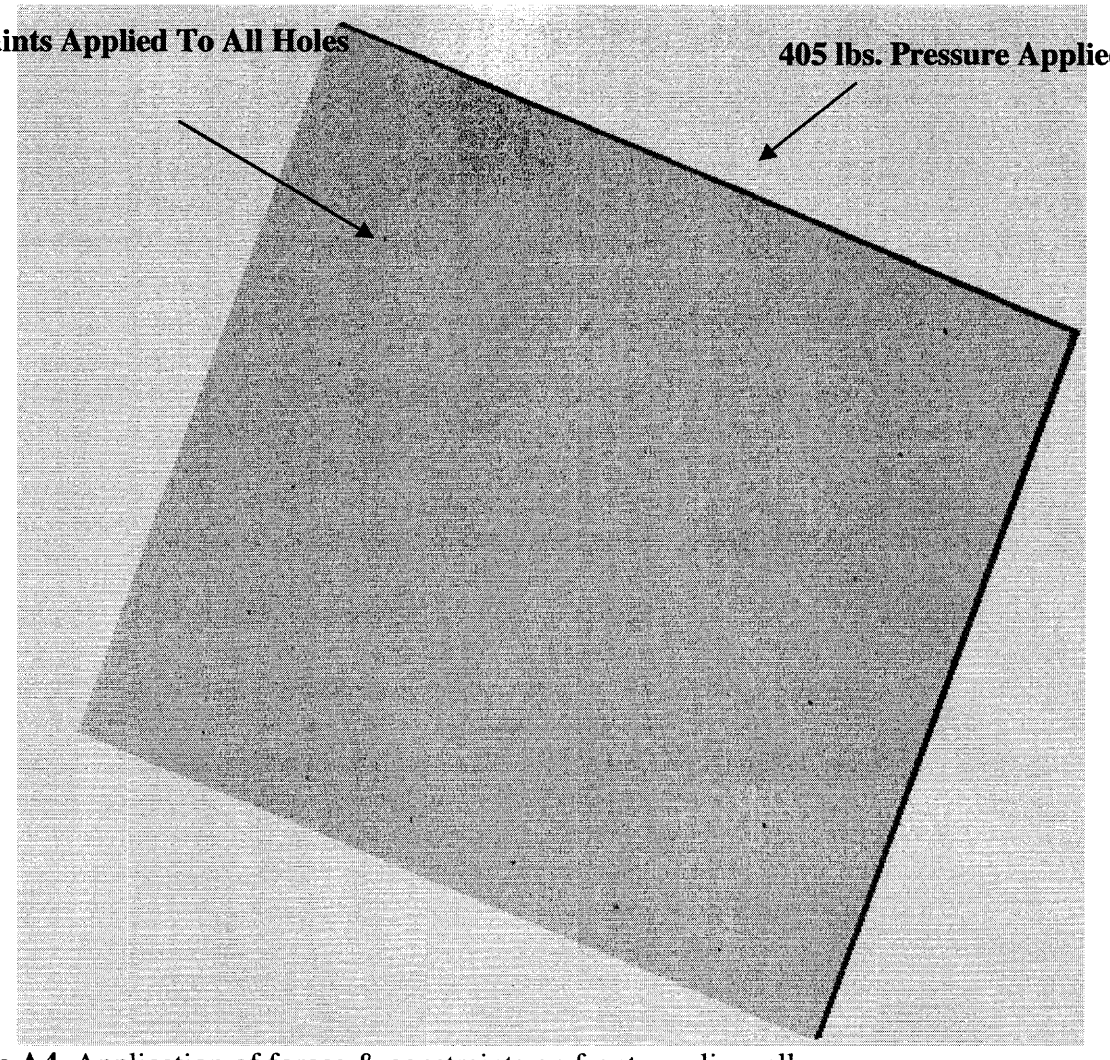

Figure A4 Application of forces & constraints on front acrylic wall

Results and Discussion

The Pro/Mechanica Stress results (Figure 5) show convergence of data points; therefore, the stress values attained could be considered accurate. The maximum stress (1.0291 psi) experienced under loading is much less than the yield strength (10660 psi) of the acrylic material.

Figure A5 Pro/Mechanica Von Mises Stress (psi) results on front acrylic wall

The Pro/Mechanica Displacement results (Figure 6) show convergence of data points; therefore, the displacement values attained could be considered accurate. The maximum displacement ($1.9638*10^{-9}$) experienced under loading is very small and could be considered approximately zero.

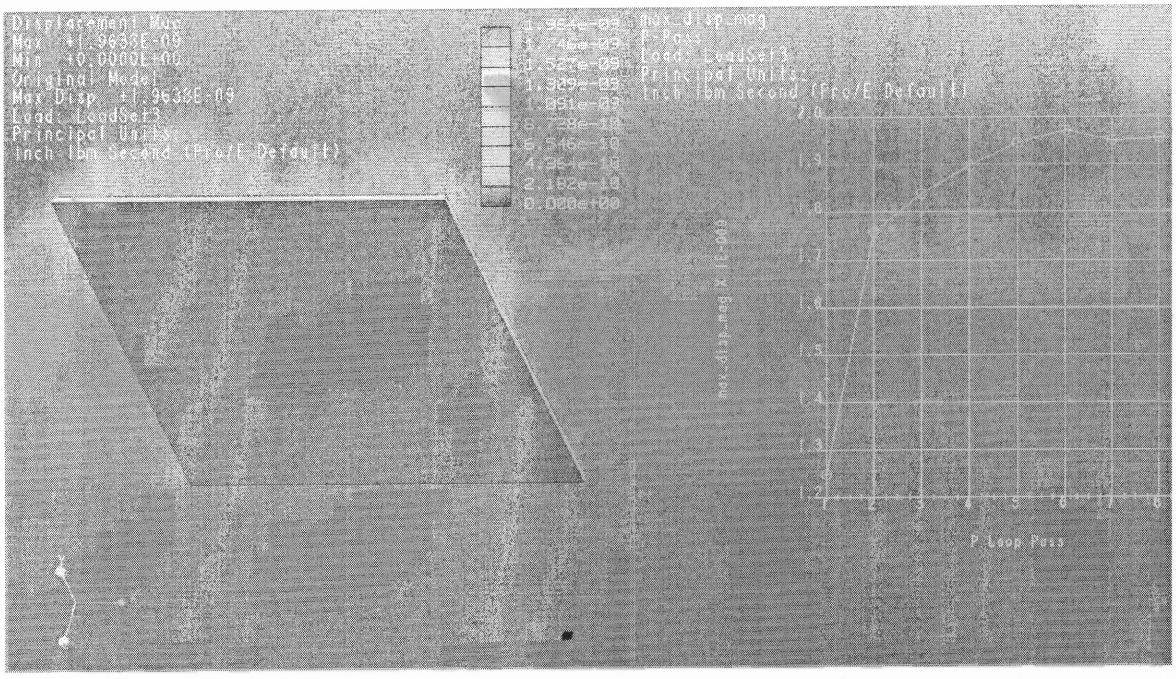

Figure A5 Pro/Mechanica displacement (in) results on front acrylic wall

Conclusion

An analysis was conducted to determine whether the acrylic box's walls would remain intact if the experimental equipment became unfastened and struck one of the acrylic walls with an acceleration nine times that of gravity at sea level (32.2 ft/s^2). The Pro/Engineer CAD software was used to model the front acrylic wall, and the FEA static analysis was conducted with The Pro/MECHANICA software package. The maximum stress (1.0291 psi) experienced under loading is much less than the yield strength (10660 psi) of the acrylic material. The maximum displacement ($1.9638*10^{-9}$) experienced under loading is very small and could be considered approximately zero. Therefore, we conclude that the acrylic walls of the equipment housing will not fail under extreme conditions.

7.0 Electrical Analysis

7.1 Wiring Schematic

An electrical diagram of the experiment is presented in Electrical Diagram (at the end of this document). The blow-off current corresponds to 1.1Imax where Imax is the maximum current through a protected unit. The voltage signal between the HV Amplifier and rotating chamber is 4 kV at 100 Hz, HV Amplifier output current range is 0 +/- 40 mA, it is auto regulated and the limits on the current between the rotating chamber and HV amplifier can be set within this range [8]. Wires, which are carrying electric signal from HV amplifier to Rotating Chamber are secured in the braided shield cable, which protects personal from an electrical hazard and reduces the interference to the aircraft systems. Multi-meter measures the output signal from the HV Amplifier. This measurement is made by hard-wired connection in order to control the high voltage signal, which goes to the rotating chamber.

7.2 Load Tables

Only one power source is used to run the experiment from an aircraft power distribution panel. Power strip 2 is used to distribute the power between Function generator, HV Amplifier, Multi-meter, and Power Strip 1, where Pump, Light Source, Step motor controller, and Camera are plugged in. Power Strip 2 uses a 14 AWG extension cord and has a 20 A circuit breaker. The power source details are given in the table 7.1

Table 7.1 Load Table

Power Source Details	Load Analysis
Name: Power Strip 2 (Main strip)power cord	HV Power Supply: 2.4 A
Voltage: 110 VAC, 60 Hz	Multi-meter: 0.1 A
Wire Gauge: 14	Function Generator: 03A Power Strip1: 4.5
Max Outlet Current: **20 Amps**	Total Current Draw: **7.3 Amps**

The maximum current or power ratings for the primary AC electrical components of the different flight systems are listed in Tables 7.2 and 7.3

Table 7.2: AC electrical load analysis for the Experimental Box-Power Strip 1

Component	current (A) ratings	AWG ratings
Controller & Step motor	0.8 A	18x3
Digital camera	0.3 A	2x18
Light source	2.8 A	3x18
Pump and driver	0.6 A	18x3c
Power Strip 1 (15 Amps. C.B)		14x3c

Table 7.3: AC electrical load analysis for the Power Supply plate –Power Strip 2 (Main Power Strip)

Component	current (A) ratings	AWG ratings
Regulated power supply	2.4 A	14x3
Multi-meter	0.1 A	3x18
Function generator	0.3 A	18x3c
Power Strip 2 (20 Amps. C.B.)		14x3c

A Main Power Off kill switch is located on the Power Strip on the Power Supply Plate (Figure 8), which will shut down all electrical connections to the equipment.

There will be no damage to the equipment in the event of an unexpected power loss.

8.0 Pressure/Vacuum System Documentation Requirements

No pressure/vacuum system used. The liquids used in the test are incompressible under the test conditions. In order to prevent building high-pressure inside the acrylic box, it contains holes of 1" diameter.

9.0 Laser Certification

No laser system used

10.0 Parabola Details and Crew Assistance

This experimental program requires a week of flights with 30 parabolas in each. The time needed for a single parabola experiment is around 20-25 seconds. The gravity levels should be as low as possible. During each parabola, one run of experiments will be

conducted. The field-induced particle motions and segregation will be recorded with a digital camera.

11.0 Institutional Review Board

No IRB approval needed.

12.0 Hazard Analysis Guidelines

Identification of possible hazards:

Systems and units to be analyzed	Failure of the item	Improper usage of the item
Commercial electronic devices: generator, regulated power supply, and driving motors for pumping a suspension and rotating the chamber	Electrical hazard due to shorted power circuit	
Rotating chamber	Electrical hazard due to shorted power circuit	
Electrodes in the chamber	Electrical hazard due to the electric discharge through the suspending fluid	Electric hazard due to shorted high-voltage circuit

Flight Research Hazard Analysis

KC-135 Micro-gravity aircraft program

Experiment Title: The Synergism of Electrorheological Response, Dielectrophoresis, and Shear-Induced Diffusion in Flowing Suspensions

Hazard 1:

Electric hazard can be produced due to a shorted power circuit of a commercial or a custom-built electric device.

Causes:

Possible cause is a failure of an electric device, which can occur because of the mechanical impact, component aging, excessive moisture in the environment, or a higher than normal AC applied voltage.

Controls:

An electric fuse is installed in each key component. The Model 10/40 is protected against over-voltage or/and over-current conditions that may be generated by active loads or by output short circuits to ground. This protection is ensured by either Trip Off or Current Limit upon reaching a panel adjustable current set value, or an automatic internal power monitor and limit function. In addition, an electric fuse is installed in a power strip used to connect all the electric devices with the external AC power line. All the enclosures and handles are grounded. Wires, which are carrying electric signal from HV amplifier to Rotating Chamber are secured in the braided shield cable

Risk Assessment

Severity Category: IV Probability Level: C Risk Assessment: acceptable

Code: 10

Flight Research Hazard Analysis

KC-135 Micro-gravity aircraft program

Experiment Title: The Synergism of Electrorheological Response, Dielectrophoresis, and Shear-Induced Diffusion in Flowing Suspensions

Hazard 2:

Electrical hazard can be produced due to a shorted high-voltage circuit. This can happen if a suspension in the chamber is electrically broken. This will lead to a short-time high current which will immediately activate the protection action of the high-voltage amplifier.

Causes:

There are three possible causes for failure:

(1) The presence of large air bubbles in a suspension.

(2) The applied voltage is too high (>5kV).

Controls:

Remove bubbles from suspensions when loading.

Preset a low current level of the high voltage amplifier (follow the pre- in- flight procedure).

Perform the emergency shut down procedure (Turn off the Main Power of the experiment)

Risk Assessment

Severity Category: III Probability Level: D Risk Assessment: acceptable

Code: 14

Flight Research Hazard Analysis

KC-135 Micro-gravity aircraft program

Experiment Title: The Synergism of Electrorheological Response, Dielectrophoresis, and Shear-Induced Diffusion in Flowing Suspensions

Hazard 3:

Electrical shock from the cable which connects the electrodes to a +/- 4000 volt amplifier. Such a shock could result in severe injury.

Causes:

Contact with the end of the cable where it is connected to the electrodes of the rotating chamber while the amplifier is enabled.

Controls:

The cable used in the experiment is a special High - Voltage Output assembly supplied by manufacturer of the HV amplifier [8]

The end of the cable, which is connected to the electrodes of the rotating chamber, is secured in the Experimental Box. The box will be closed at all time during the flight.The HV amplifier is turned on only after the lid of the Experimental Box is closed. The Power Supply Plate and the Experimental Box should be fixed right next to each other, so that the length of the cable that connects the electrodes of the rotating chamber to the HV amplifier will be minimized. Wires, which are carrying electric signal from HV amplifier to Rotating Chamber are secured in the braided shield cable

Risk Assessment

Severity Category: II Probability Level: D Risk Assessment: acceptableCode: 10

Flight Research Hazard Analysis

KC-135 Micro-gravity aircraft program

Experiment Title: The Synergism of Electrorheological Response, Dielectrophoresis, and Shear-Induced Diffusion in Flowing Suspensions

Hazard 4:

Oil leak from the rotating chamber flow system. In micro gravity conditions, an oil droplet could form, get out of the Experimental box, and interfere with experimental equipment or personnel.

Causes:

a) Failure of silicon tubing or disconnection of barbed nozzle connection due to pinching of the tubing.

b) Leaking rubber gasket

Controls:

The experimental box encloses the rotating chamber so oil droplet most likely splatters on the side or the bottom of the box. The rubber gasket is inspected every flight day. If replacement is needed, spare gaskets are available for each flight day. The experiment shut-down procedure is implemented if a leak occurs.

Risk Assessment:

Severity Category: IV Probability level: E Risk Assessment: acceptable

13.0 Tool Requirements

Tools to bring to the Reduced Gravity facility:

- Standard socket set
- Combination wrenches
- Assorted screwdrivers
- Allen wrenches
- Pliers and wire cutters
- Electrical equipment (portable hydrometer, magnetic stirrer)
- Beakers for loading/changing the suspension in the rotating camber

Tools to use on the airplane:

- Assorted screwdrivers for mounting the peristaltic pump inside the Experimental Box, and closing the lid of the box.

14.0 Photo Requirements

Since we will be using a digital camcorder to record the suspension flow no additional photo equipment is requested.

15.0 Aircraft Loading

The experiment can be loaded on the aircraft with the fork lift and lifting pallet.

There are two assemblies should be loaded on the aircraft:

(1. The acrylic box with an experimental setup (Experimental Box) (~ 267 lb., 15 ft^2)

(2) The aluminum plate with a high voltage power supply and a control system (Power Supply Plate) (~ 180 lb., 8 ft^2)

Dollies are useful for moving them to and from the forklift in Building 101. The forklift can be used to load them on the aircraft and 4 – 6 people can pick them up to carry to the proper aircraft station. The Experimental Box and Power Supply Plate are both bolted down with 3/8-24 UNF bolts (which will be supplied at GRC) in a square pattern (bolt spacing of 20 inches). 6 bolts are required for the Experimental Box, and 6 bolts for Power Supply Plate.

Floor Loading:

Experimental Box:

Base-plate area: 15 ft^2

Weight: 267 lbs

Loading: 17.8 lbs/ft^2

Power Supply Plate:

Base-plate area: 8 ft^2

Weight: 180 lbs

Loading: 22.5 $lbs/9\ ft^2$

16.0 Ground Support Requirements

Power 110V at 60Hz is required for ground testing of the setup.

Access to the machine shop is required, if available.

17.0 Hazardous Materials

No toxic, corrosive, explosive or flammable materials will be used during the flight experiment.

18.0 Experimental Procedure Documentation

Equipment Shipment to Glenn Research Center

The experimentalists will deliver the equipment by cargo van.

Ground Operations

After Removing the equipment from the cargo van very little work is required to set up for the Test Readiness Review and Aircraft loading.

The facilities required at GRC are: access to 110 VAC and bench space for working on the experiment modules.

Loading

The experiment can be loaded on the aircraft with the fork lift and lifting pallet Dollies are useful for moving them to and from the forklift in Building 101. The forklift can be used to load them on the aircraft and 4 – 6 people can pick them up to carry to the proper aircraft station. The Experimental Box and Power Supply Plate are both bolted down with 3/8-24 UNF bolts (which will be supplied by at GRC) in a square pattern (bolt spacing of 20 inches). 6 bolts are required for the Experimental Box, and 6 bolts for Power Supply Plate.

Pre-Flight

Morning setup prior to flight will require 45-60 minutes with 110 VAC power available

Pre-Flight Checklist

1. Mount peristaltic pump and test chamber with flight sample into Experiment Box.
2. Check armature connections on test chamber.
3. Connect electrical connectors to test chamber.

4. Connect motor to test chamber.
5. Check test chamber tube fit.
6. Turn "On" Main Power located on power strip on Power Supply Plate.
7. Turn On High Voltage (HV) amplifier on Power Supply Plate.
8. Turn "On" and check Frequency Generator on Power Supply Plate is functioning..
9. Check output (between 2000 – 4000V) on Digital Multimeter on Power Supply Plate. Actual reading on Digital Multimeter 2-4V. Output divided on device by 1000
10. Check power in test experiment box. (Check power strip indicator light"On").
11. Check Light source, camera, and pump power "On".
12. Check motor controller function.
13. Insert Camera tape (Change tape every flight).
14. Camera FOV check. Lock into position.
15. Turn "Off" High Voltage Amplifier on Power Supply Plate.
16. Turn "Off" Main Power located on power strip on Power Supply Plate.
17. Close and seal experiment box.

The stepper motor, which controls the rotation of the chamber, is operated using a remote control by one of the experimentalists.

Take-off/Landing

The only requirement for take-off and landing are storage space for magnetic stirrer and closed beaker with the suspension.

In-Flight

In One gravity:

1. Turn "On" Main Power located on power strip on Power Supply Plate.
2. Check Light source, camera, and pump power "On".
3. Check/ test motor controller function "On".
4. Turn On High Voltage (HV) amplifier on Power Supply Plate.
5. Check Frequency Generator on Power Supply Plate is functioning..
6. Check output (between 2000 – 4000V) on Digital Multimeter on Power Supply Plate. Actual reading on Digital Multimeter 2-4V. Output divided on device by 1000.
7. Check camera recording; (Stays on through balance of flight all parabolas).

On entering Zero gravity:

8. Bring test chamber into horizontal position using motor controller <F1>.
9. Unlock High Voltage lock out (PULL grey mushroomhead) On High Voltage (HV) amplifier on Power Supply Plate.
10. Power High Voltage (WHITE Button) on High Voltage (HV) amplifier on Power Supply Plate.

When Gravity returns to Aircraft:

11. Shut Off (LOCK) High Voltage lock out (PUSH grey mushroomhead) On High Voltage (HV) amplifier on Power Supply Plate.
12. Restart test chamber rotation using motor controller <RUN - F1- 2-ENTER>.

Repeat Steps 8 through 12, cycling as time and parabolas allow.

Inflight Shutdown Procedures

1. Turn "Off" On High Voltage (HV) amplifier on Power Supply Plate.
2. Turn "Off" Main Power located on power strip on Power Supply Plate.
3. Temp stow camera remote and motor control panel.

Emergency Shut Off Procedures

Turn "Off" Main Power located on power strip on Power Supply Plate.

Flow system:

During the flight the suspension will be run in the close loop. It will be loaded into the Rotating chamber before the take off and will be run for a couple of cycles to remove the bubbles. There will be no beaker in the Experimental Box. The suspension will be circulated through a single silicone tubing (1.5' – 2' long). One end of the tubing will be connected to the inlet swivel and the other one to the outlet swivel. The amount of the suspension in the chamber and tubing will be < 40 ml (Figure 7). If pressure of the system exceeds the maximum value of 25 psi, the oil leakage is likely to occur. (See hazard 4). The value of 25 psi is derived from the maximum pressure ratings of the tubing. (ref. Masterflex BioPharm Silicon Tubing Catalog, product number: EW-96420-14.

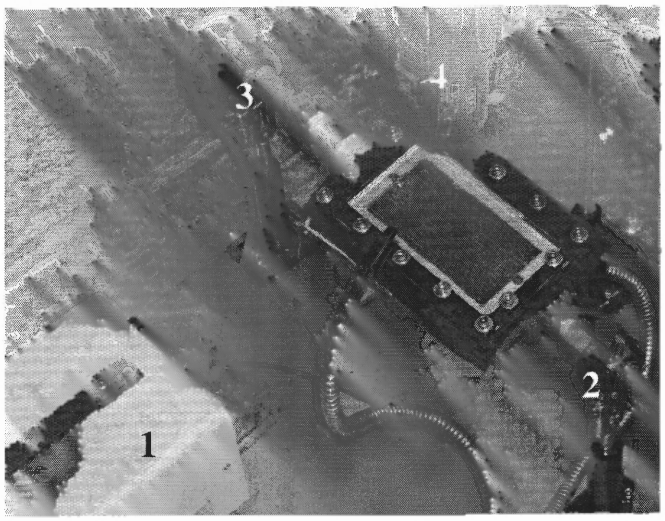

1. **Pump**
2. **Inlet**
3. **Outlet**
4. **Camcorder**

Figure 7. Flow system

The experiment can be rotated onto each of the 6 sides of the Experimental Box without leaking the suspension from the rotating chamber.

Post-Flight

1 Open the Experimental Box

2 Take out the pump, rotating chamber and the camcorder to prepare for the next day

3 Dispose used suspension and prepare a new one for the next flight

Off-Loading

No special procedures required for off-loading. The experimental equipment will be unloaded after the last day of the flight in same way it was loaded.

22.0 Bibliography

[1] Khusid, B. and A. Acrivos, Phase diagrams of electric-field-induced aggregation in conducting colloidal suspensions, Phys. Rev. E 60, 3015 (1999)

[2] Khusid, B. and A. Acrivos, Phase diagrams of electric-field-induced aggregation in conducting colloids, The Fourth Microgravity Fluid Physics & Transport Phenomena Conference, NASA, Cleveland, OH, August 1998

[3] Khusid, B. and A. Acrivos, Effects of the interparticle electric interactions on dielectrophoresis in suspensions. Phys. Rev E 54, 5428 (1996)

[4] Khusid, B. and A. Acrivos, Effects of conductivity in electric-field-induced aggregation in electrorheological fluids. Phys. Rev. E 52, 1669 (1995)

[5] Barret, R., Fastener Design Manual, NASA Reference Publication 1228, 1990

[6] Pro/Engineer: www.ptc.com

[7] Material Properties: www.matwweb.com

[8] Trek Model 10/40 High – Voltage Power Amplifier Operators manual

[9] Ugural, Ansel C. & Fenster, Saul K. Advanced Strength And Applied Elasticity 3rd Edition. Prentice Hall (New Jersey), 1995

[10] Deutschman, Michels, & Wilson. Machine Design Theory & Practice. Macmillan Publishing Co., Inc. (New York, 1975), p. 10.

Drawings of the experiment components

Power Supply Plate

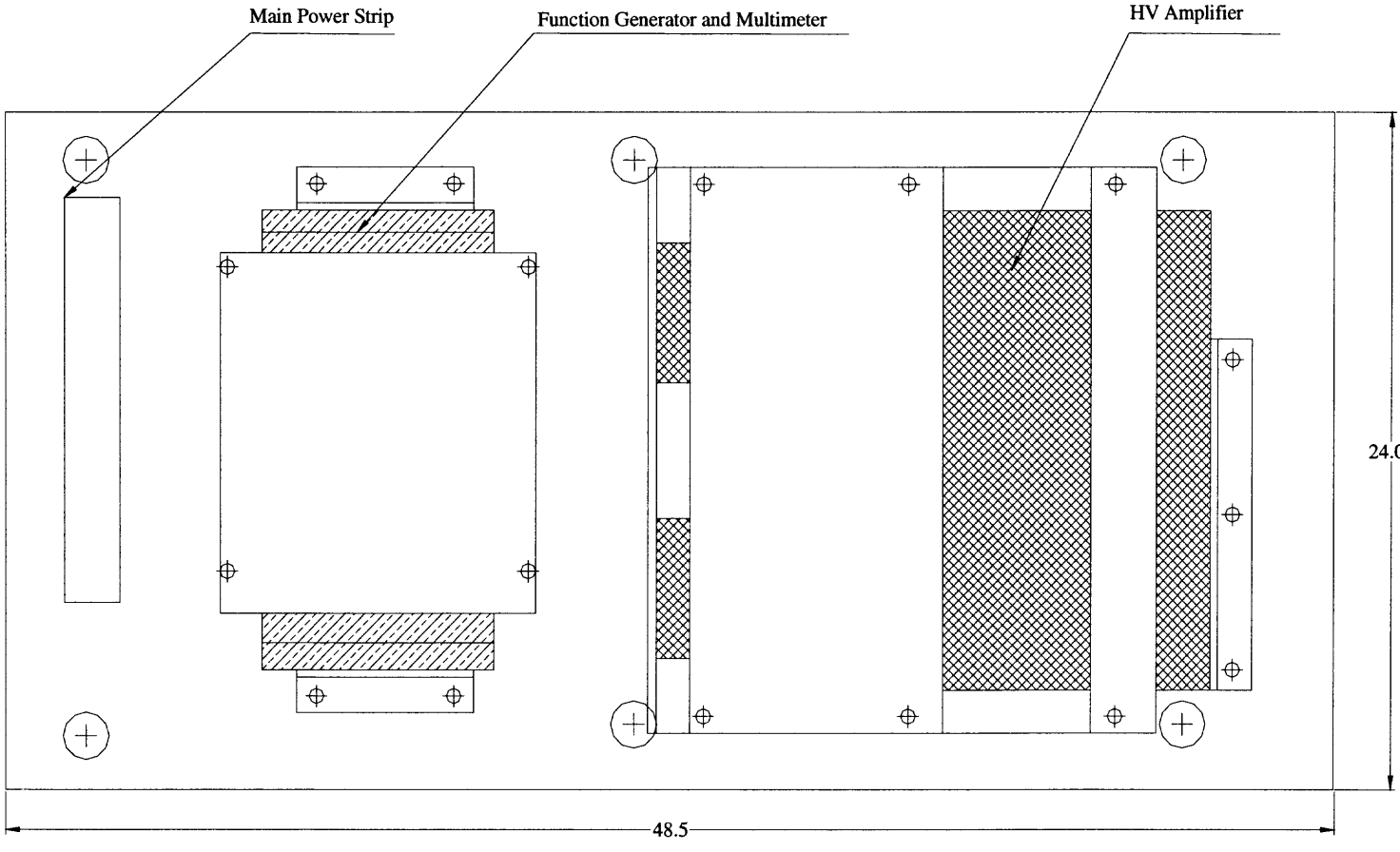

All Components are attched using Aluminum 6061-T6 sheets
with Ø 10/32 Alloy steel and AN steel screws

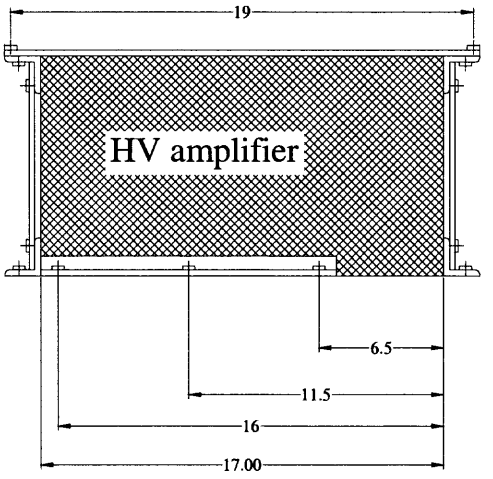
19
HV amplifier
6.5
11.5
16
17.00

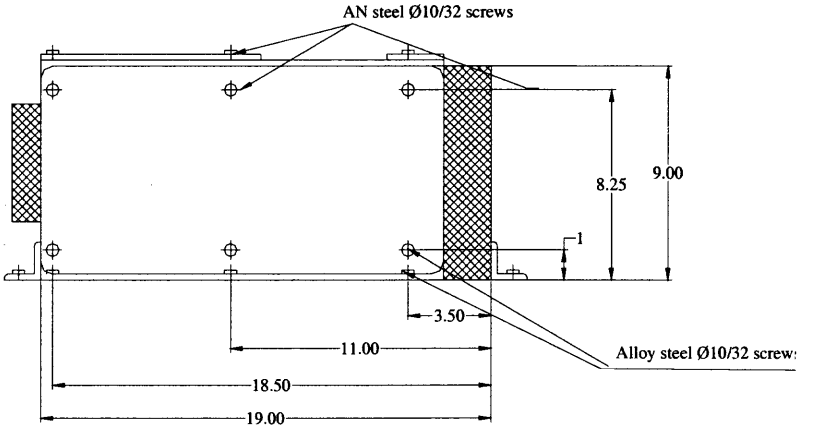
AN steel Ø10/32 screws
8.25
9.00
1
3.50
11.00
18.50
19.00
Alloy steel Ø10/32 screw

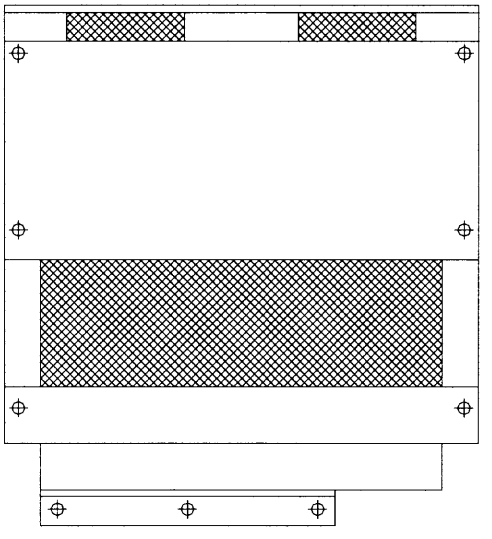

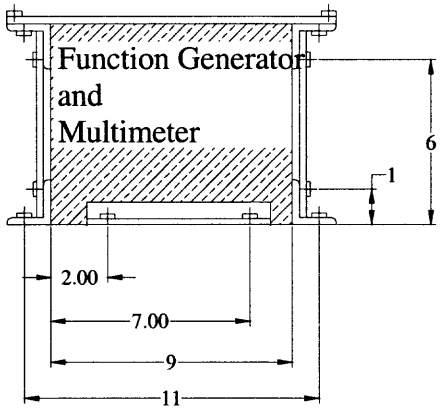

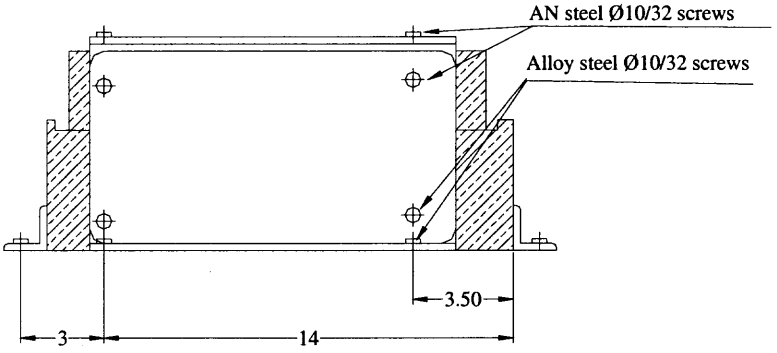

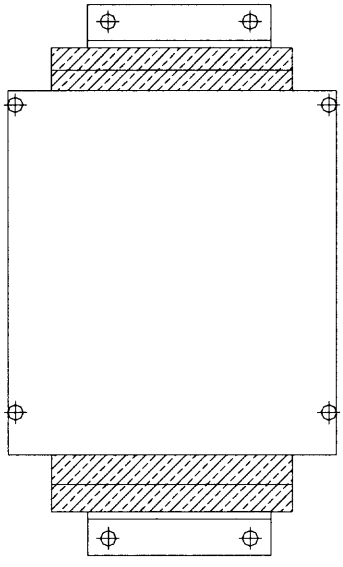

Experimental Box

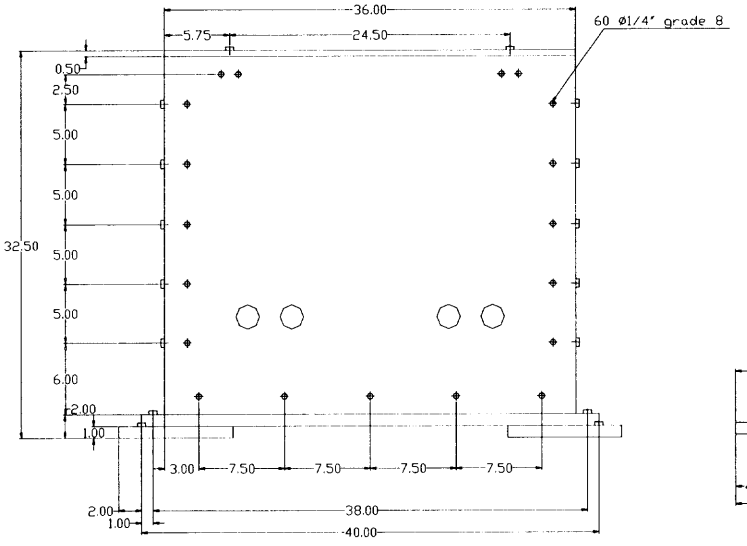
36.00
5.75
24.50
60 Ø1/4" grade 8
0.50
2.50
5.00
5.00
5.00
5.00
5.00
6.00
2.00
1.00
32.50
3.00
7.50
7.50
7.50
7.50
2.00
1.00
38.00
40.00

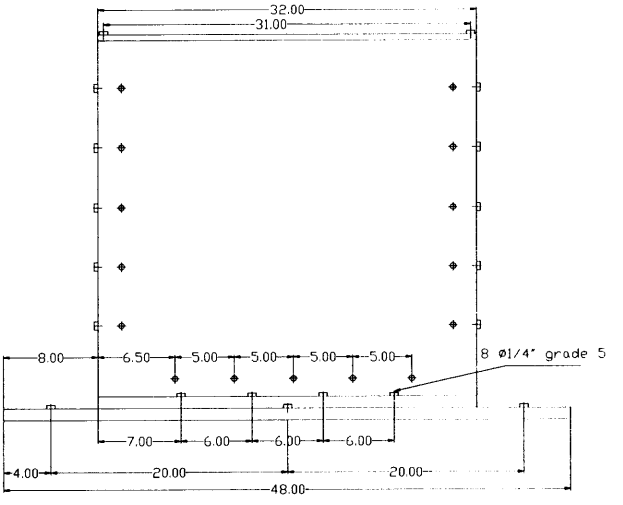
32.00
31.00
8.00
6.50
5.00
5.00
5.00
5.00
8 Ø1/4" grade 5
7.00
6.00
6.00
6.00
4.00
20.00
20.00
48.00

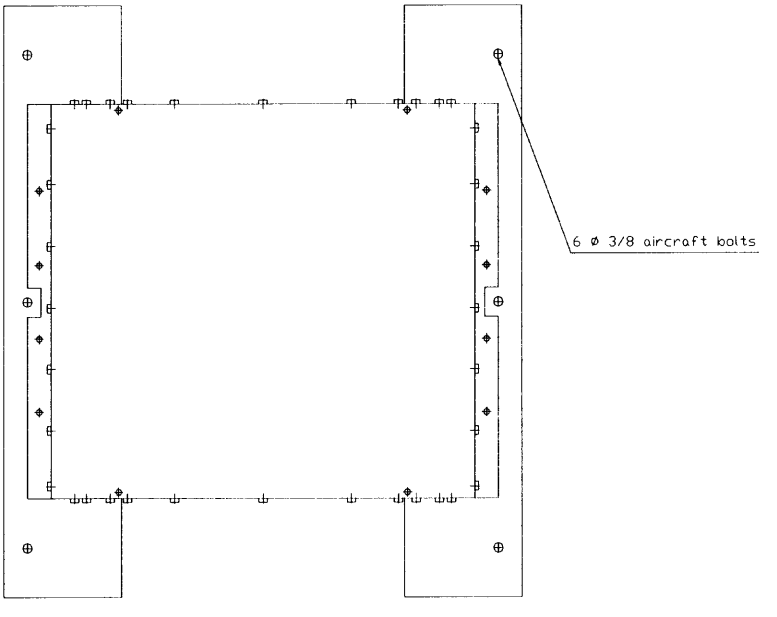
6 Ø 3/8 aircraft bolts

Pull-test Results

Equipment Pull-test Worksheet/Report Project: **Particle Segregation** Date: 9/4/02

Item Description:	Step-motor & bracket		
Manufacturer:	IDC	Model No.:	P32V-EMK
Dimensions (in.)[1]:	4.0 x 4.0 x 7.0	Weight:	9.2 lb
Gauge Description:	Digital force gauge		
Manufacturer:	Chatillon	Model No.:	DFIS-200
Serial No.:	B39279	NASA Tag:	2050334
Cal. Date:	3/6/2002	Cal. Due:	3/6/2003
Notes, comments:	Pull tested to 9g in all horizontal directions to preserve orientation flexibility.		
Case 1:	L.F.[2] 9g Dir. +X	**Case 2:**	L.F.[2] 9g Dir. -X
Target Load (lb):	82.8	Target Load (lb):	82.8
Max. load applied[3]:	89 lb	Max. load applied[3]:	89 lb
Hold Time:	15 sec.	Hold Time:	15 sec.
Inspector (sign.):	M. Dobbs	Inspector (sign.):	M. Dobbs
Case 3:	L.F.[2] 9g Dir. +Y	**Case 4:**	L.F.[2] 9g Dir. -Y
Target Load (lb):	82.8	Target Load (lb):	82.8
Max. load applied[3]:	91 lb	Max. load applied[3]:	90 lb
Hold Time:	15 sec.	Hold Time:	15 sec.
Inspector (sign.):	M. Dobbs	Inspector (sign.):	M. Dobbs
Case 5:	L.F.[2] 2g Dir. Up	**Case 6:**	L.F.[2] 6g Dir. Dn
Target Load (lb):	18.4	Target Load (lb):	55.2
Max. load applied[3]:	24 lb	Max. load applied[3]:	60 lb
Hold Time:	15 sec.	Hold Time:	15 sec.
Inspector (sign.):	M. Dobbs	Inspector (sign.):	M. Dobbs.

[1]Length x Width x Height
[2]Load Factor
[3]Optional

Inspector (print name): Michael Dobbs 7555/ZIN M.S. 101-1

This report is not valid unless accompanied by signature of inspector.

Signature of inspector certifies that the minimum load applied over the specified hold time is equal to or greater than the target load specified.

Loads must be applied at/through equipment Center of Gravity (CG), or corrected computationally to CG.

Include a sketch on a separate sheet to indicate coordinate axes employed and locations of force application.

y
z
x

Equipment Pull-test Worksheet/Report Project: **Particle Segregation** Date: 9/4/02

Item Description:	Video Camera & stand		
Manufacturer:	Panasonic	Model No.:	PV-DV950
Dimensions (in.)[1]:	4.0 x 4.0 x 20	Weight:	4.5 lb
Gauge Description:	Digital force gauge		
Manufacturer:	Chatillon	Model No.:	DFIS-200
Serial No.:	B39279	NASA Tag:	2050334
Cal. Date:	3/6/2002	Cal. Due:	3/6/2003
Notes, comments:	Camera is positioned at approx. Z = 15 in. This position will be taken as the vertical C.G.		
Case 1:	L.F.[2] 9g Dir. +X	**Case 2:**	L.F.[2] 9g Dir. -X
Target Load (lb):	40.5	Target Load (lb):	40.5
Max. load applied[3]:	43	Max. load applied[3]:	44
Hold Time:	15 sec.	Hold Time:	15 sec.
Inspector (sign.):	M. Dobbs	Inspector (sign.):	M. Dobbs
Case 3:	L.F.[2] 9g Dir. +Y	**Case 4:**	L.F.[2] 9g Dir. -Y
Target Load (lb):	40.5	Target Load (lb):	40.5
Max. load applied[3]:	44	Max. load applied[3]:	43
Hold Time:	15 sec.	Hold Time:	15 sec.
Inspector (sign.):	M. Dobbs	Inspector (sign.):	M. Dobbs
Case 5:	L.F.[2] 2g Dir. Up	**Case 6:**	L.F.[2] 6g Dir. Dn
Target Load (lb):	9.0	Target Load (lb):	27
Max. load applied[3]:	12	Max. load applied[3]:	32
Hold Time:	15 sec.	Hold Time:	15 sec.
Inspector (sign.):	M. Dobbs	Inspector (sign.):	M. Dobbs

[1]Length x Width x Height
[2]Load Factor
[3]Optional

Inspector (print name): Michael Dobbs 7555/ZIN M.S. 101-1

This report is not valid unless accompanied by signature of inspector.

Signature of inspector certifies that the minimum load applied over the specified hold time is equal to or greater than the target load specified.

Loads must be applied at/through equipment Center of Gravity (CG), or corrected computationally to CG.

Include a sketch on a separate sheet to indicate coordinate axes employed and locations of force application.

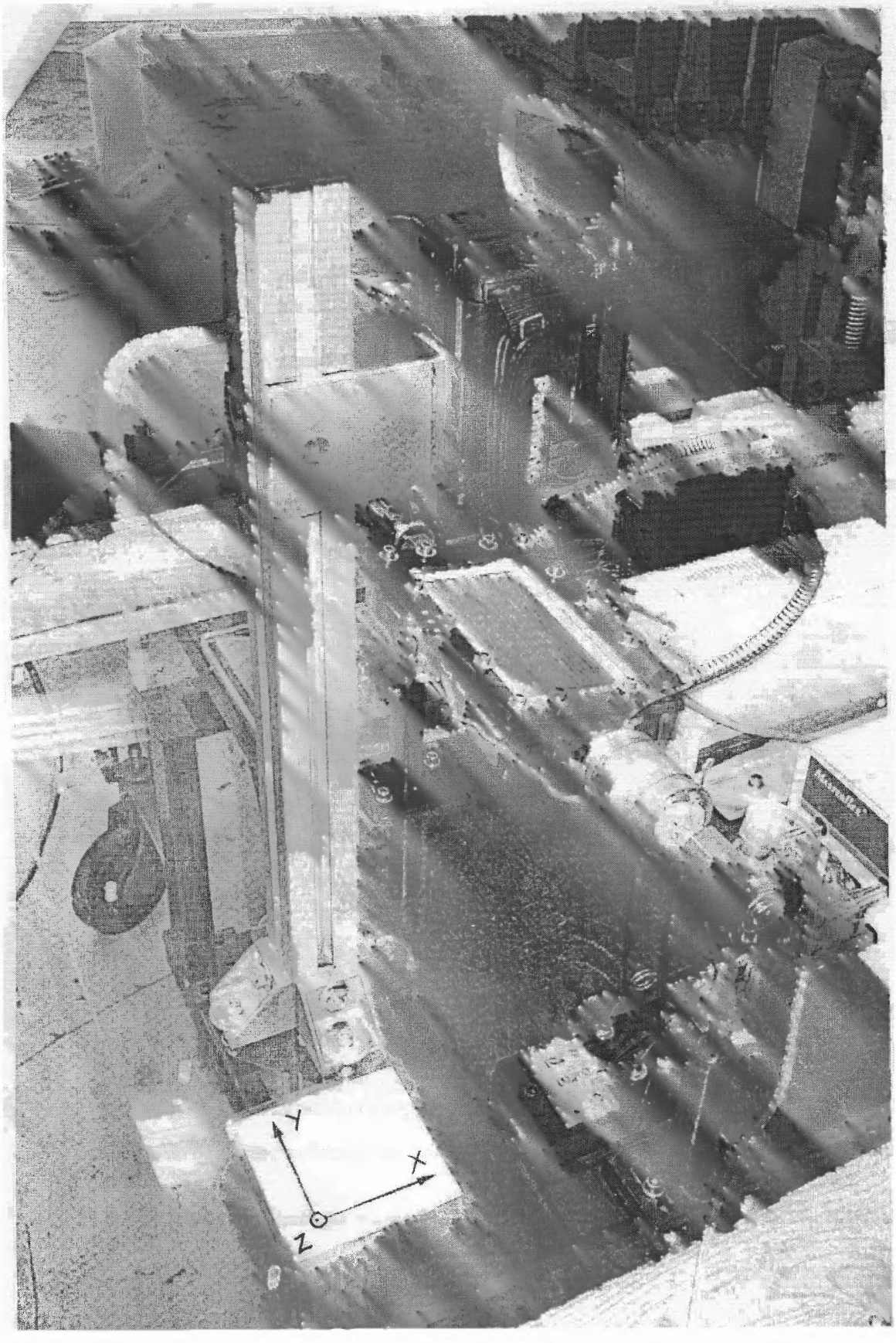
Y
X
Z

Equipment Pull-test Worksheet/Report Project: **Particle Segregation** Date: 9/4/02

Item Description:	Step motor controller		
Manufacturer:	IDC	Model No.:	SmartStep
Dimensions (in.)[1]:	6.0 x 2.5 x 5.5	Weight:	2.7 lb
Gauge Description:	Digital force gauge		
Manufacturer:	Chatillon	Model No.:	DFIS-200
Serial No.:	B39279	NASA Tag:	2050334
Cal. Date:	3/6/2002	Cal. Due:	3/6/2003
Notes, comments:	Pull tested to 9g in all horizontal directions to preserve orientation flexibility.		
Case 1:	L.F.[2] 9g Dir. +X	**Case 2:**	L.F.[2] 9g Dir. -X
Target Load (lb):	24.3	Target Load (lb):	24.3
Max. load applied[3]:	30 lb	Max. load applied[3]:	30 lb
Hold Time:	15 sec.	Hold Time:	15 sec.
Inspector (sign.):	M. Dobbs	Inspector (sign.):	M. Dobbs
Case 3:	L.F.[2] 9g Dir. +Y	**Case 4:**	L.F.[2] 9g Dir. -Y
Target Load (lb):	24.3	Target Load (lb):	24.3
Max. load applied[3]:	30 lb	Max. load applied[3]:	30 lb
Hold Time:	15 sec	Hold Time:	15 sec.
Inspector (sign.):	M. Dobbs	Inspector (sign.):	M. Dobbs
Case 5:	L.F.[2] 2g Dir. Up	**Case 6:**	L.F.[2] 6g Dir. Dn
Target Load (lb):	5.4	Target Load (lb):	16.2
Max. load applied[3]:	9 lb	Max. load applied[3]:	
Hold Time:	15 sec.	Hold Time:	
Inspector (sign.):	M. Dobbs	Inspector (sign.):	

[1]Length x Width x Height
[2]Load Factor
[3]Optional

Inspector (print name): Michael Dobbs 7555/ZIN M.S. 101-1

This report is not valid unless accompanied by signature of inspector.

Signature of inspector certifies that the minimum load applied over the specified hold time is equal to or greater than the target load specified.

Loads must be applied at/through equipment Center of Gravity (CG), or corrected computationally to CG.

Include a sketch on a separate sheet to indicate coordinate axes employed and locations of force application.


Y
X
Z
Motor Controller

Equipment Pull-test Worksheet/Report Project: **Particle Segregation** Date: 9/4/02

Item Description:	Light Source		
Manufacturer:	Moritex	Model No.:	MHF-G150LR
Dimensions (in.)[1]:	4.5 x 4.8 x 10	Weight:	8.4 lb
Gauge Description:	Digital force gauge		
Manufacturer:	Chatillon	Model No.:	DFIS-200
Serial No.:	B39279	NASA Tag:	2050334
Cal. Date:	3/6/2002	Cal. Due:	3/6/2003
Notes, comments:	Pull tested to 9g in all horizontal directions to preserve orientation flexibility.		
Case 1:	L.F.[2] 9g Dir. +X	**Case 2:**	L.F.[2] 9g Dir. -X
Target Load (lb):	75.6	Target Load (lb):	75.6
Max. load applied[3]:	80 lb	Max. load applied[3]:	81 lb
Hold Time:	15 sec.	Hold Time:	15 sec
Inspector (sign.):	M. Dobbs	Inspector (sign.):	M. Dobbs
Case 3:	L.F.[2] 9g Dir. +Y	**Case 4:**	L.F.[2] 9g Dir. -Y
Target Load (lb):	75.6	Target Load (lb):	75.6
Max. load applied[3]:	80 lb	Max. load applied[3]:	80 lb
Hold Time:	15 sec.	Hold Time:	15 sec.
Inspector (sign.):	M. Dobbs	Inspector (sign.):	M. Dobbs
Case 5:	L.F.[2] 2g Dir. Up	**Case 6:**	L.F.[2] 6g Dir. Dn
Target Load (lb):	16.8	Target Load (lb):	50.4
Max. load applied[3]:	20 lb	Max. load applied[3]:	N/A
Hold Time:	15 sec.	Hold Time:	
Inspector (sign.):	M. Dobbs	Inspector (sign.):	

[1]Length x Width x Height
[2]Load Factor
[3]Optional

Inspector (print name): Michael Dobbs 7555/ZIN M.S. 101-1

This report is not valid unless accompanied by signature of inspector.

Signature of inspector certifies that the minimum load applied over the specified hold time is equal to or greater than the target load specified.

Loads must be applied at/through equipment Center of Gravity (CG), or corrected computationally to CG.

Include a sketch on a separate sheet to indicate coordinate axes employed and locations of force application.

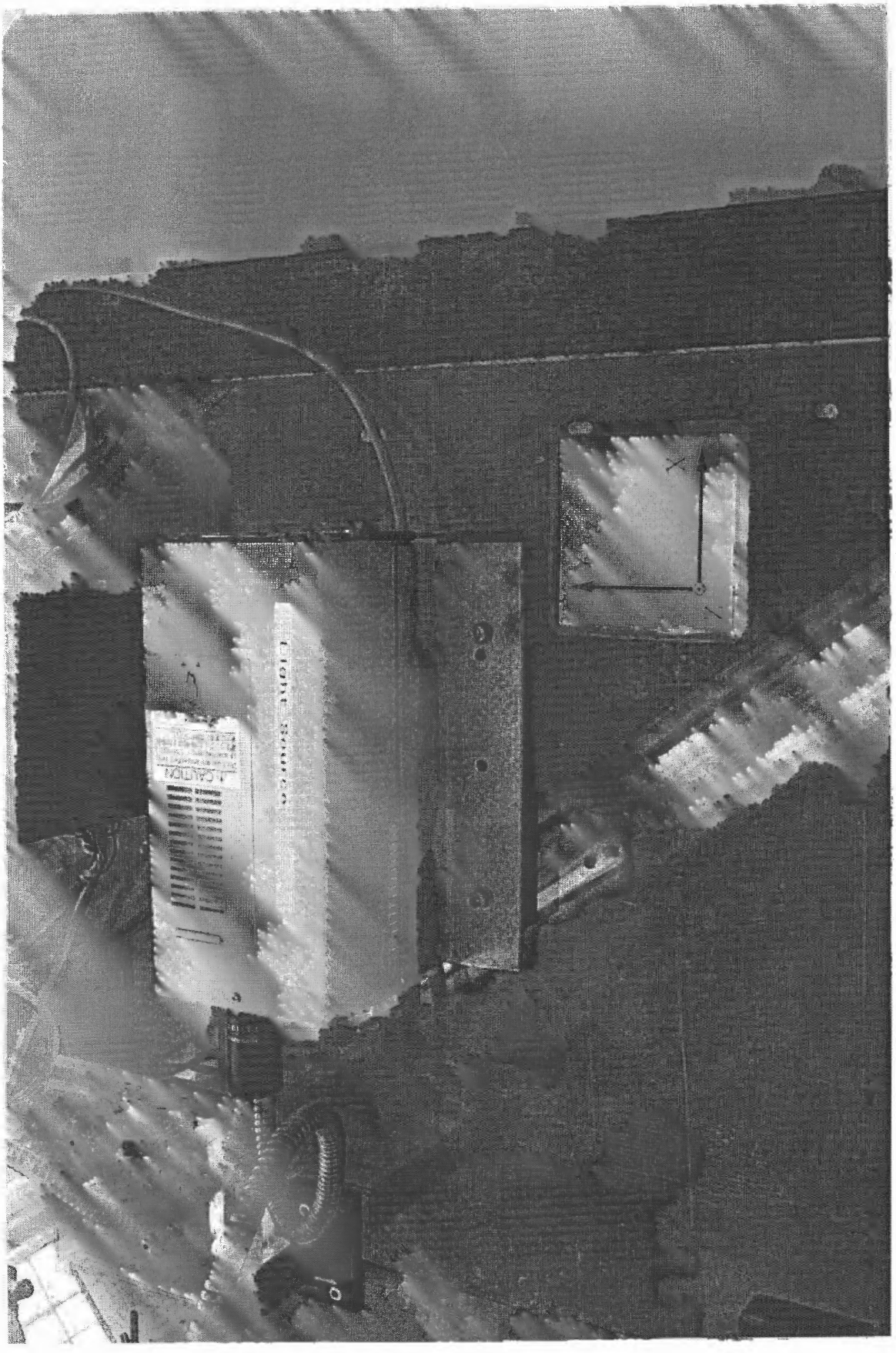

Equipment Pull-test Worksheet/Report Project: **Particle Segregation** Date: 9/4/02

Item Description:	Peristaltic pump		
Manufacturer:	Masterflex	Model No.:	7520-35
Dimensions (in.)[1]:	5.0 x 6.5 x 11.3	Weight:	13.7 lb
Gauge Description:	Digital force gauge		
Manufacturer:	Chatillon	Model No.:	DFIS-200
Serial No.:	B39279	NASA Tag:	2050334
Cal. Date:	3/6/2002	Cal. Due:	3/6/2003
Notes, comments:	Pull tested to 9g in all horizontal directions to preserve orientation flexibility.		
Case 1:	L.F.[2] 9g Dir. +X	**Case 2:**	L.F.[2] 9g Dir. -X
Target Load (lb):	123.3	Target Load (lb):	123.3
Max. load applied[3]:	129 lb	Max. load applied[3]:	128 lb
Hold Time:	15 sec.	Hold Time:	15 sec.
Inspector (sign.):	M. Dobbs	Inspector (sign.):	M. Dobbs
Case 3:	L.F.[2] 9g Dir. +Y	**Case 4:**	L.F.[2] 9g Dir. -Y
Target Load (lb):	123.3	Target Load (lb):	123.3
Max. load applied[3]:	130 lb	Max. load applied[3]:	126 lb
Hold Time:	15 sec.	Hold Time:	15 sec.
Inspector (sign.):	M. Dobbs	Inspector (sign.):	M. Dobbs
Case 5:	L.F.[2] 2g Dir. Up	**Case 6:**	L.F.[2] 6g Dir. Dn
Target Load (lb):	27.4	Target Load (lb):	82.2
Max. load applied[3]:	30 lb	Max. load applied[3]:	N/A
Hold Time:	15 sec.	Hold Time:	
Inspector (sign.):	M. Dobbs	Inspector (sign.):	

[1]Length x Width x Height
[2]Load Factor
[3]Optional

Inspector (print name): Michael Dobbs 7555/ZIN M.S. 101-1

This report is not valid unless accompanied by signature of inspector.

Signature of inspector certifies that the minimum load applied over the specified hold time is equal to or greater than the target load specified.

Loads must be applied at/through equipment Center of Gravity (CG), or corrected computationally to CG.

Include a sketch on a separate sheet to indicate coordinate axes employed and locations of force application.

Equipment Pull-test Worksheet/Report Project: **Particle Segregation** Date: 9/4/02

Item Description:	Rotating Chamber & supports		
Manufacturer:	Project	Model No.:	n/a
Dimensions (in.)[1]:	4.5 x 2.0 x 16.0	Weight:	4.5 lb
Gauge Description:	Digital force gauge		
Manufacturer:	Chatillon	Model No.:	DFIS-200
Serial No.:	B39279	NASA Tag:	2050334
Cal. Date:	3/6/2002	Cal. Due:	3/6/2003
Notes, comments:			
Case 1:	L.F.[2] 9g Dir. +X	**Case 2:**	L.F.[2] 9g Dir. -X
Target Load (lb):	40.5	Target Load (lb):	40.5
Max. load applied[3]:	42 lb	Max. load applied[3]:	42 lb
Hold Time:	15 sec.	Hold Time:	15 sec.
Inspector (sign.):	Mr Dobbs	Inspector (sign.):	Mr Dobbs
Case 3:	L.F.[2] 9g Dir. +Y	**Case 4:**	L.F.[2] 9g Dir. -Y
Target Load (lb):	40.5	Target Load (lb):	40.5
Max. load applied[3]:	42 lb	Max. load applied[3]:	42 lb
Hold Time:	15 sec.	Hold Time:	15 sec.
Inspector (sign.):	Mr Dobbs	Inspector (sign.):	Mr Dobbs
Case 5:	L.F.[2] 2g Dir. Up	**Case 6:**	L.F.[2] 6g Dir. Dn
Target Load (lb):	9.0	Target Load (lb):	27
Max. load applied[3]:	13 lb	Max. load applied[3]:	30 lb
Hold Time:	15 sec	Hold Time:	15 sec.
Inspector (sign.):	Mr Dobbs	Inspector (sign.):	Mr Dobbs

[1]Length x Width x Height
[2]Load Factor
[3]Optional

Inspector (print name): Michael Dobbs 7555/ZIN M.S. 101-1

This report is not valid unless accompanied by signature of inspector.

Signature of inspector certifies that the minimum load applied over the specified hold time is equal to or greater than the target load specified.

Loads must be applied at/through equipment Center of Gravity (CG), or corrected computationally to CG.

Include a sketch on a separate sheet to indicate coordinate axes employed and locations of force application.

y
z
x

Equipment Pull-test Worksheet/Report Project: **Particle Segregation** Date: 9/5/02

Item Description:	Experiment base plate		
Manufacturer:	project	Model No.:	
Dimensions (in.)[1]:	32 x 40 x 1	Weight:	29.3 lb (components)
Gauge Description:	Digital force gauge		
Manufacturer:	Chatillon	Model No.:	DFIS-200
Serial No.:	B39279	NASA Tag:	2050334
Cal. Date:	3/6/2002	Cal. Due:	3/6/2003
Notes, comments:	This test is intended to address bending in the plate resulting from loads applied by the individual components subject to the 6g downward load factor. 2g upward load is implicitly addressed, by similarity.		
Case 1:	L.F.[2] 9g Dir. +X	**Case 2:**	L.F.[2] 3g Dir. -X
Target Load (lb):		Target Load (lb):	
Max. load applied[3]:	N/A	Max. load applied[3]:	N/A
Hold Time:		Hold Time:	
Inspector (sign.):		Inspector (sign.):	
Case 3:	L.F.[2] 2g Dir. +Y	**Case 4:**	L.F.[2] 2g Dir. -Y
Target Load (lb):		Target Load (lb):	
Max. load applied[3]:	N/A	Max. load applied[3]:	N/A
Hold Time:		Hold Time:	
Inspector (sign.):		Inspector (sign.):	
Case 5:	L.F.[2] 2g Dir. Up	**Case 6:**	L.F.[2] 6g Dir. Dn
Target Load (lb):		Target Load (lb):	175.8
Max. load applied[3]:	N/A	Max. load applied[3]:	195
Hold Time:		Hold Time:	15 sec.
Inspector (sign.):		Inspector (sign.):	M. Dobbs

[1]Length x Width x Height
[2]Load Factor
[3]Optional

Inspector (print name): Michael Dobbs 7555/ZIN M.S. 101-1

This report is not valid unless accompanied by signature of inspector.

Signature of inspector certifies that the minimum load applied over the specified hold time is equal to or greater than the target load specified.

Loads must be applied at/through equipment Center of Gravity (CG), or corrected computationally to CG.

Include a sketch on a separate sheet to indicate coordinate axes employed and locations of force application.

Electrical Diagram

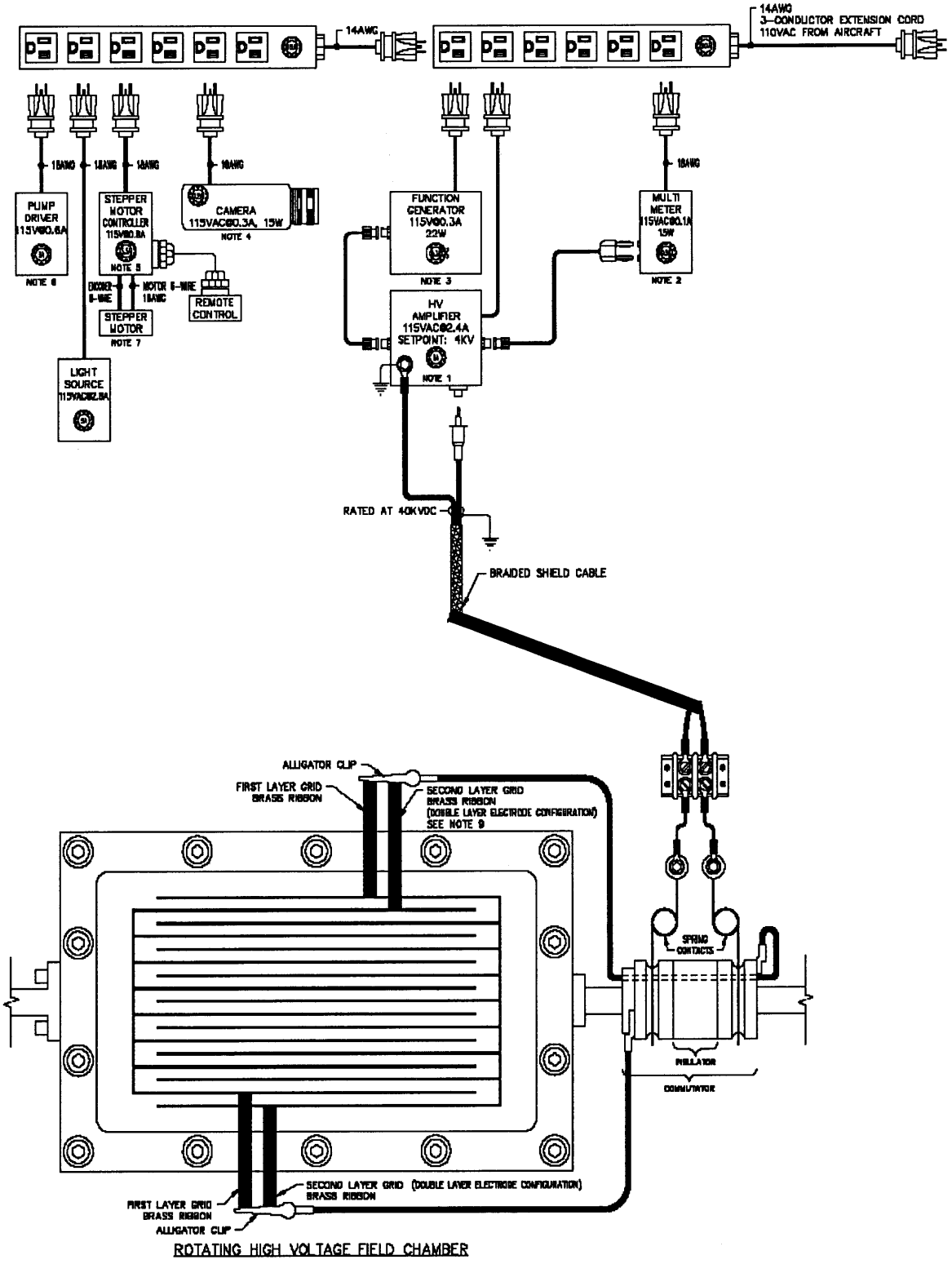

Questions and Answers

Questions from Chris Hegedus

Flight Test Engineer

QSS Group , Inc. @ NASA Glenn Research Center

Mail Stop 4-8

21000 Brookpark Rd.

Cleveland, Ohio 44135

Phone: 216-433-8496

FAX: 216-433-8144

QUESTION 1 I would like your team to consider when installing the experiment the routing of the high voltage cable to minimize the potential exposure to high voltage at ANY time the experiment is installed on the aircraft. I am reacting to a statement in you Hazards Analysis on pg 26 discussing taping the high Voltage cable to the floor. The cabling should not be routed on the floor or outside the boundaries of the experiment rack in a manner that will permit the damage of the insulation by someone walking or falling on it. I do not know where your rig will be placed in the cabin. If it is placed close to the cabin wall, placing the cables between the wall and the experiment's rack should help. I would suggest discussing the rig's placement with Jim Withrow and Mike Dobbs .

RESPONSE: The HV amplifier and Experimental Box will be placed at the minimum possible distance from each other to minimize the length of the wires running outside the Experimental Box. Also, according to suggestions from Jim Withrow and Mike Dobbs, wires, which are carrying electric signal from HV amplifier to Rotating Chamber are secured in the braided shield cable, which protects personnel from an electrical shock and reduces the interference to the aircraft systems.

QUESTION 2 I would like to know what wave shape the 100Hz 4Kv signal is. This info request is done with regards to the possibility that signal leakage may have an impact on aircraft avionic and power systems or experiments co-residing in the aircraft cabin. I suspect the signal is a sine wave which should cause the least problems. If the signal wave shape is a square, impulse or sawtooth, I would like know if you have an effective shielding plan for possible harmonics that might remotely affect systems. At the least, I will ask that an avionics EMI / RFI check be performed if there is a potential for aircraft operations interference.

RESPONSE: The shape of the signal in the experiments is a sine wave.

QUESTION 3 In the TEDP, the wire gauge is stated as 14. Is that for all wires associated with your experiment? What is the high voltage cable, twisted wire pair or coax?

RESPONSE: The wire gauges are indicated in the table 9.3 on page 21 of TEDP.

The high voltage cable consists of two separate wires, high voltage signal wire and grounded wire. They are not twisted. The rating of the high voltage signal and grounded signal wires are the following: AWM 3239 1005C 40KVDC

QUESTION 4 In the TEDP, the hazard analysis concerning the shock from the 4Kv amplifier states that the amplifier is turned on only after the experimental box is closed (pg 26). Given that I have not seen the rig, I would like to know if the potential exists for someone to open the box with high voltage present due to perhaps a procedural fault, distraction or some other event? Would a limit switch that prevents the amplifier to be powered be an appropriate prevention measure?

RESPONSE: In case of the procedural fault, the power in the whole experiment (including the HV amplifier) will be cut off manually using a kill (Main power off) switch located on the plated with HV amplifier. Experimental Box will remain closed during the flight.

Questions from Gary T Huber

QUESTION 1: Is the Mazola loaded into the test rig prior to loading the rig onto the plane or is the Mazola poured into the test rig while in the test rig is still in the hangar? If it is loaded with Mazola on the plane, do you have a means of cleaning up any spills?

RESPONSE: The Mazola corn oil will be loaded into the chamber in the hanger therefore there will be no spills on the plane.

QUESTION 2 On page 13 section 8.4 it states that "This force was applied uniformly across the smallest acrylic wall." A worse case would be to have the package smash into the wall with a corner rather than smash into the wall uniformly. Would it be possible to do the analysis in this mode across the smallest wall and the largest wall?

RESPONSE: Consider the whole package having the total weight of 45 lb to be smashing into the wall with a corner represented by an area of about 0.1 square inch at the acceleration of nine times that of the gravity at the sea level ($9*32.2\ ft/s^2=289.8\ ft/s^2$). Then the force of 405 lbf to be acting on the area of 0.1 square inch will result in a pressure of 4050 psi which is much less than the yield strength (10660 psi) of the acrylic material.

QUESTION 3 Is the rotating chamber leak proof? If it is, this means that it is a pressure vessel. Do you have the analysis to show it will withstand an explosive decompression of the cabin? If it is not leak proof, what keep the Mazola inside the chamber?

RESPONSE: The rotating chamber leaks out air but it is leak proof for highly viscous fluids like the Mazola corn oil.

QUESTION 4 Would it be possible to put the Hazards Analysis in the standard Glenn form C-923a?

RESPONSE: The form C-923a is attached. As can be seen from this form, the only hazard relevant to our experiment is the electrical one.

QUESTION 5 On page 42 under the Emergency Shutdown section it states that the kill switch is "easily accessible to the operator." Is it easily accessible to the test conductor?

RESPONSE: Yes, the kill (Main Power Off) switch is easily accessible to both the operator and the test conductor.

SAFETY PERMIT HAZARD ANALYSIS WORKSHEET

HAZARD CATEGORY	DESCRIPTION OF SPECIFIC HAZARDS	DESCRIPTION OF PLANNED HAZARD CONTROLS OR SAFETY PROCEDURES	RISK INDEX
COLLISION	N/A	☐ Overspeed Control ☐ Crane Proofloading ☐ Guards ☐ Lockout/Tagout Procedures ☐ Barricade Plan ☐ Blast Shield ☐ Critical Speed Analysis ☐ Triburst Calculations ☐ Other	
CHEMICAL	N/A	☐ Ventilation ☐ Detectors ☐ Proper Storage ☐ Personal Protective Equipment ☐ HazCom Training ☐ Proper Labeling ☐ Spill Resource Procedures ☐ Respiratory Protection Program ☐ Other	
ELECTRICAL SHOCK	Electric hazard can be produced due to: 1. a shorted power circuit of a commercial or a custom-built electric device 2. a shorted high-voltage circuit.This will immediately activate the protection action of the high-voltage amplifier 3. Electrical shock from the cable which connects the electrodes to a +/- 4000 volt amplifier.	☐ Grounding ☑ Guards ☐ Designed per NEC ☐ Current limiting devices ☑ Lockout/Tagout Procedures ☐ Other	1. IV C 10 2. III D 14 3. II D 10
TEMPERATURE EXTREMES	N/A	☐ Temperature Controls ☐ Temperature Alarms ☐ Personal Protective Equipment ☐ Other	

HAZARD CATEGORY	DESCRIPTION OF SPECIFIC HAZARDS	DESCRIPTION OF PLANNED HAZARD CONTROLS OR SAFETY PROCEDURES	RISK INDEX
LASER RADIATION	N/A	☐ Laser Radiation Form ☐ Compliance with ANSI Z136.1 ☐ Interlocks ☐ Annual Eye Exams ☐ Shielding ☐ Barricade Plan ☐ Signs ☐ Other	
NUCLEAR RADIATION	N/A	☐ NRC License Review ☐ Radiation Detection Equipment ☐ Shielding ☐ Barricade Plan ☐ Signs ☐ Other	
OTHER RADIATION	N/A	☐ Shielding ☐ Barricade Plan ☐ Signs ☐ Other	
LOSS OF HABITABLE ATMOSPHERE	N/A	☐ Ventilation ☐ Detectors ☐ Confined Space Entry Procedures ☐ Temperature Control ☐ Other	
BIOLOGICAL	N/A	☐ Personal Protective Equipment ☐ Bloodborne Pathogen Program ☐ Disposal Methods ☐ Other	
OTHER	4. Oil Leak due to pinching of the tubing or leaky gasket.	Enclosure of the Rotating Chamber in the Experimenal Box, and daily inspection of the chamber components	4.IV E

REFERENCES

Batchelor, G. K., *An Introduction to Fluid Dynamics* (Cambridge University Press, Cambridge, 1993), pp. 182-183.

Burt, P. H., T. A. K. Al-Ameen, and R. Pethig, An optical dielectrophoresis spectrometer for low- frequency measurments on colloidal suspensions, *J. Phys. E: Instrum.*, vol 22, 1989, 952-957.

Cui, L. and H. Morgan, Design and fabrication of traveling wave dielectrophoresis structure, *J. Micromech. Microeng.*, **10** ,(2000) 72–79

Daniel, V. V., *Dielectric Relaxation* (Academic Press, London and New York, 1967)

Dukhin, S. S., and V.N. Shilov, *Dielectric Phenomena and the Double Layer in Disperse Systems and Polyelectrolytes* (Wiley, New York, 1974).

Dussaud, A. , B. Khusid and A. Acrivos, Particle segregation in suspensions subject to high-gradient ac electric fields, J. *Appl. Phys.*, Vol. 88, No. 10, (2000) *Electrohydrodynamics*. Edited by A. Castellanos (Springer, Wien, 1998).

Gascoyne, P. R. C., Y. Huang, R. Pethig, J. Vykoukal, and F. F. Becker, Dielectrophoretic separation of mammalian cells studied by computerized image analysis, *Meas. Sci. Technol.*, vol. 3, 1992, 439-445.

Gascoyne, P. R. C., and J. Vykoukal, Electrophoresis, 23, 1973 (2002) *Handbook of Electrostatic Processes*, edited by J.-S. Chang, A.J. Kelly, and J.M.Crowley (Marcel Dekker, New York, 1995).

Halsey, T. C., Science, **258**, 761 (1992).

Hass, K. C., Phys. Rev. E **47**, 3362 (1993).

Hill, N. E., W.E. Vaughan, A.H. Price, and M. Davies, *Dielectric Properties and Molecular Behavior* (Van Nostrand, London, 1969).

Jones, T. B., *Electromechanics of Particles* (Cambridge University Press, Cambridge, 1995).

Jun Yang, Ying Huang, Xiao-Bo Wang, Frederick F. Becker, and Peter R. C. Gascoyne, Cell separation on microfabricated electrodes using dielectrophoresis/gravitational field-flow fractionation *Anal. Chem.*1999, 71, 911-918

Kaler, K. V. I. S., and T. B. Jones, Dielectrophoretic spectra of single cells determined by feedback controlled levitation, *Biophys. J.*, vol. 57, 1990, 173-182.

Khusid, B., and A. Acrivos, Phys. Rev. E **54**, 5428 (1996).

Khusid, B., and A. Acrivos, Phys. Rev. E **52**, 1669 (1995).

Khusid, B., and A. Acrivos, Phys. Rev. E **60**, 3015 (1999).

Koch, K., A. Evans, and A. Brunnschweiler, *Microfluidic Technology and Applications* (Research Studies Press, Baldock, 2000).

Langtangen, H. P., *Computational Partial Differential Equations: Numerical Methods and Diffpack Programming* (Springer, Berlin, 1999).

Landau, L. D., L.P. Lifshitz, and L.P. Pitaevski, *Electrodynamics of Continuous Media* (Pergamon, Oxford, 1984).

Lin, I. J., and L. Benguigui, in *Progress in Filtration and Separation*, edited by R.J. Wakerman (Elsevier, Amsterdam, 1983), Vol. 3, pp. 149-205.

Marszalek, P., J. J. Zielinski, and M. Fikus, Experimental verification of a theoretical treatment of the mechanism of dielectrophoresis, *Bioelectrochem. Bioenergetics*, vol. 22, 1989, 289-298.

Masuda, S., M. Washizu, and T. Nanba, Novel method of cell fusion in the field construction area in fluid integrated circuit, *IEEE Trans. IAS*, vol.25, 1989 732-737.

Pethig, R., 1996 ,Dielectrophoresis: Using inhomogeneous A.C. electric fields to separate and manipulate cells *Crit.Rev. Biotechnol.*, **16**, 331–48

Pethig, R., Y. Huang, X. B. Wang, and J. P. H. Burt, Positive and negative dielectrophoretic collection of colloidal particles using interdigitated castellated microelectrodes, *J. Phys. D: Appl. Phys.*, vol. 25, 881 (1992).

Pohl, H. A., The motion and precipitaion of suspensoids in divergent electric fields, *J. Appl. Phys.*, vol. 22, 1951, 869-871.

Pohl, H. A., 1978 *Dielectrophoresis* (Cambridge: CambridgeUniversity Press)

Pohl, H. A. and K. Pollock, in *Perry's Chemical Engineers' Handbook*, 6th ed., edited by R.H. Perry, D.W. Green, and J.O. Maloney (McGraw-Hill, New York, 1984), 17-45.

Price, J. A. R., J. P. H. Burt, and R. Pethig, "Applications of a new optical technique for measuring the dielectrophoretic behavior of micro-organisms," *Biochim. Biophys. Acta*, vol. 964, 1988, 221-230. *Progress in Electrorheology. Science and Technology of Electrorheological Materials*, edited by K.O. Havelka and F.E. Filisko (Plenum Press, New York, 1995).

Z. Qiu, N. Markarian, B. Khusid, and A. Acrivos, J. Appl. Phys., **92**, 2829 (2002)

Ramos, A., H. Morgan , N. G. Green and A. Castellanos, Ac electrokinetics: a review of forces in microelectrode structures, *J. Phys. D: Appl. Phys.*vol. **31** (1998) 2338–2353.

Russel, W. B., D. A. Saville, W. R. Schowalter, *Colloidal Dispertions* (Cambridge University Press, Cambridge, 1989).

Shapiro, M., A.L. Shalom, and I.J. Lin, J. Appl. Phys. **58**, 1028 (1985).

Washizu, M., and O. Kurosawa, Electrostatic manipulation of DNA in microfabricated structures, *IEEE Trans. IAS*, vol.26, 1990, 1165-1172.

Washizu, M., O.Kurosawa, I. Arai, S. Suzuki, and S. Shimamoto, Applications of electrostatic stretch and positioning of DNA, Proc. Of IEEE/IAS Annual Meeting, Toronto, Canada, 1993b, 1629-1637.

Washizu, M., T. Nanba, and S. Masuda, Handling biological cells using a fluid integrated circuit, *IEEE Trans. IAS,* vol. 26, 1990, 352-358.

Zimmermann, U., J. Vienken, Electric field induced cell to cell fusion, *J. Membrane Biol.,* vol. 67, 1982, 165-182

Zimmermann, U. in *Electromanipulation of Cells*, edited by U. Zimmermann and G. A. Neil (CRC Press, London, 1996), p. 173; Biochim. Biophys. Acta 694, 227 (1982).

Zukoski, C. F., Annu. Rev. Mater. Sci. **23**, 45 (1993).